Prediction and analysis of JET fusion performance based on reduced first principle transport models

PhD Thesis

Scuola di Dottorato in Scienze e Tecnologie per l'Innovazione Industriale
Facoltà di Ingegneria Civile e Industriale
Dipartimento di Ingegneria Astronautica, Elettrica ed Energetica
Dottorato di Ricerca in Energia e Ambiente (XXXV cycle)

Vito Konrad Zotta
ID number 1725522

Advisor
Chiarissimo Prof. Renato Gatto

Co-Advisor
Dr. Luca Garzotti

Academic Year 2021/2022

Thesis defended on January the 25^{th}, 2023
in front of a Board of Examiners composed by:

Prof. Lucia Fontana, Roma Tre University
Prof. Fulvio Palmieri, Roma Tre University
Prof. Marco Sabatini, Sapienza University of Rome (chairman)

:

Prof. Lidia Piron, University of Padova
Dr. Fernanda Rimini, JET Senior Manager

Prediction and analysis of JET fusion performance based on reduced first principle transport models
PhD thesis. Sapienza University of Rome

This thesis has been typeset by LaTeX and the Sapthesis class.

Version: January the 8^{th}, 2023

Author's email: vitokonrad.zotta@uniroma1.it

"Science, after all, must be demarcated from a curiosity shop where funny local - or cosmic - oddieties are collected and displayed."

Imre Lakatos,

Falsification and the Methodology of Scientific Research Programmes

Acknowledgments

At the end of this research work I would like to thank Sapienza and the Department of Astronautical, Electrical and Energy Engineering for their support to my research activities and for the opportunity of participating to the European fusion research program led by EUROfusion; in particular Professor Renato Gatto who has supervised my activities allowing me to lead my research interests freely, Professor Massimo Corcione and Professor Gianfranco Caruso who have coordinated the activities of the PhD Program in Energy and Environment. A special thank must be devoted to Dr. Luca Garzotti for his supervision on the research activities performed at JET. He has been an excellent mentor during these years, even during the pandemic, and he has inspired me both in professional and in private life. I need to thank also the external reviewers Dr. Fernanda Rimini and Dr. Lidia Piron for their useful comments that have improved the quality and the clarity of this manuscript.

In these years I've been introduced in the wide community of European Fusion Researchers and I had the opportunity of meeting and discussing with many physicists who have contributed directly and indirectly in my research and in my growth, some of them are: Dr. Gianluca Pucella, Dr. Daniele Brunetti, Dr. Francis J. Casson, Dr. Jonathan Citrin, Dr. Michele Marin, Dr. Hyun-Tae Kim, Dr. Fulvio Auriemma, Dr. Giovanni Artaserse for his hints on life in Oxford. I'm glad to Dr. Matteo Baruzzo for guesting me in Abingdon in his beautiful house during my visitings at JET and to Luana Gentili for having taken care of all the administrative issues related to the interactions with a complex partner as EUROfusion. Finally, I would like to thank JET Task Force Leaders, Dr. Joelle Mailloux, Dr. Costanza F. Maggi, Dr. Elena de la Luna and Dr. Jeronimo Garcia for having supported and shown interest in my activities in JET experimental teams.

This work has been carried out within the framework of the EUROfusion Consortium, funded by the European Union via the Euratom Research and Training Programme (Grant Agreement No 101052200 — EUROfusion). Views and opinions expressed are however those of the author only and do not necessarily reflect those of the European Union or the European Commission. Neither the European Union nor the European Commission can be held responsible for them.

Vorrei ringraziare la mia famiglia: mio padre e mia madre per l'entusiasmo e la cura con cui mi hanno seguito in questi anni; Irene con la quale continuiamo a crescere ed a prendere le redini delle nostre vite legati da un affetto profondo che ci rende partecipi delle gioie e delle preoccupazioni dell'altro come se riguardassero noi stessi; vorrei ringraziare Alberto per la sua amicizia che si è trasformata in un affetto fraterno; Diletta che riempie ogni giorno la mia vita di felicità e di tutta la serenità di cui ho bisogno per riuscire a ragionare lucidamente tanto sugli obiettivi personali che su quelli professionali. Ringrazio mia zia Gilda e mia zia Gabriela che hanno continuato a seguire i miei progressi nonostante la lontananza esasperata dalla pandemia. Zia Franca, Zio Roberto, Ornella, Manuela, Diego ed Alessandro che fanno parte da sempre della mia "famiglia (allargata) romana".

Non posso che dirmi felice e sentirmi fortunato se penso ai miei amici. Ringrazio Fabio e le nostre conversazioni della domenica pomeriggio, Federico per le nostre "vite parallele" dai primi giorni di Università; Giampiero, un amico solido ed attento con cui confrontarsi quotidianamente; Antonio, col quale discutere di qualsiasi argomento di fisica e non solo; Cecilia ed Alessio, e Donatello che mi hanno accompagnato affettuosamente in ogni avvenimento di questi ultimi tre anni; Fabrizio e Matteo che pur non essendo più assidui compagni di studio continuano ad essere amici preziosi; Elio che anche da lontano riesce a farsi sentire sempre vicino. Vorrei ringraziare anche i nuovi amici: Patrizia, Chiara, Lorenzo, Chiara e Gianluca, Patrizio, e Stefano, quest'ultimo appassionato lettore di questa tesi ed ottimo compagno di lavoro durante l'anno appena trascorso.

Abstract

The design of a Tokamak device is carried out initially with a 0D approach aiming at defining the plasma engineering parameters estimated with the help of empirical scaling laws, and the technological limits of the device components. The assessment of local parameters (1D) is then required to define the optimal plasma performance during the entire time evolution of the discharge. In this contest, the transport of energy and particles in fusion plasmas is one of the main actor in determining the evolution of a plasma scenario both in present experiments and in future reactors.

The Joint European Torus (JET) experiment has operated in deuterium (D) and tritium (T) main ion plasma composition in 1997 (DTE1) and in 2021 (DTE2). The most important differences between the two experimental campaigns are related to the plasma facing components, carbon (C) in DTE1 and Be/W in DTE2, the increased additional heating power, and the presence of improved diagnostics, especially at the plasma edge which is determinant in the global plasma performance. After DTE1 the high levels of T retention in the C-wall have been considered unacceptable for a reactor, leading to the substitution of the C-wall with a metallic wall in the design of the International Tokamak Experimental Reactor (ITER). DTE2 campaign at JET aimed at studying D-T plasmas in the closest conditions to ITER operations. Differently from DTE1, the recent campaign focused on the stationarity of the performance and on addressing ITER-relevant aspects such as α-particles physics, plasma wall interactions and plasma heating schemes. In preparation to D-T operations, a wide experimental and modelling activity has been performed at JET in order to optimise the plasma scenarios.

The focus of this thesis is the extrapolation in D-T main ion plasma composition of the JET baseline scenario. The latter is a high confinement mode (H-mode) plasma, characterized by the presence of Edge Localized Modes (ELMs), where the confinement relies on high plasma current. In ITER D-T operations, the baseline scenario is envisaged to achieve a gain factor, defined as the ratio between the fusion power and the input power, $Q = P_{fus}/P_{in} \approx 10$. The objective of the thesis has been achieved through extensive integrated modelling, based on the reduced first principles transport models QuaLiKiz and TGLF employing different assumptions, and in a wide range of plasma operating conditions. QuaLiKiz and TGLF transport models have been validated in reference D plasmas, and their extrapolation capability with different plasma parameters has been tested by performing blind predictions. The results of the predictive modelling have been compared with the experimental data and analysed in order to address the sensitivity of the plasma scenario to the experimental boundary conditions. The QuaLiKiz transport model has also been validated against the experimental results produced at JET in DTE1.

Before the start of the DTE2 campaign, an estimate of the particle sources required to sustain a 50-50 D-T baseline plasma has been obtained. This result has provided inputs to the JET control team in the preparation phase of the baseline fuelling scheme. This contribution boosted JET D-T operations without spending experimental time, neutron and T budget.

The results of the predictive modelling performed in preparation to DTE2 are presented and discussed. The sensitivity of the predictions to plasma parameters

such as current, toroidal magnetic field, pedestal confinement and impurity content are analysed together with the sensitivity to the available amount of auxiliary heating power.

The experimental results obtained in DTE2 by the baseline scenario are also presented and discussed. In the last part of this thesis, the implications of the modelling assumptions performed on D pulses will be compared with the assumptions done on D-T discharges with the experimental boundary conditions. The key parameters needed for reliable predictions of future experiments are discussed both in D and D-T main ion plasma composition. The estimate of particle sources obtained before the DTE2 campaign are adjusted to reproduce the experimental conditions, leading to an estimate of the different fuelling channels and an evaluation of the wall sources.

The thesis is organised as follows:

- In Chapter 1 we introduce fusion as a potential energy source.
- In Chapter 2 we describe the Tokamak configuration and the JET experimental device, and we present a first comparison between the different D-T experimental campaign, and between the different scenarios prepared for DTE2.
- In Chapter 3 we introduce the issue of energy and particle transport in Tokamaks, we present the theoretical background and the state of the art of transport analysis. The models used in this work are presented together with the different assumptions implemented in JINTRAC.
- In Chapter 4 we present and discuss the validation of the reduced first principle transport models performed on D pulses. The extrapolations in D-T plasma mixture are presented with their sensitivity to the operating conditions.
- In Chapter 5 we present and discuss the baseline results obtained in DTE2. The predictive simulations are improved by adopting the actual boundary conditions of the D-T experiments, and we discuss the impact of the different assumptions on the modelling of D plasmas extrapolated to D-T plasma mixture. We show the limits of predictive simulations in integrated modelling, and we use the predictive simulations to obtain an estimate of the different fuelling sources in the D-T experiments.

Contents

Chapter 1

Introduction

The first experimental studies on plasma physics have been performed during the 1920s by I. Langmuir [5]. He has defined the “plasma” as a completely ionized gas. At the same time the English astronomer A. Eddington has speculated that the solar energy is caused by fusion processes. During the 1930s the fission nuclear reaction has been discovered and applied for the construction of an experimental nuclear reactor (1942) and for the atomic bomb (1945) [6].

At the beginning of the 1950s E. Teller in the USA coordinates the researches for a thermonuclear bomb, while other scientists start the investigations to achieve controlled thermonuclear fusion reactions in a plasma. The constrain of military secrecy on the fusion researches has been removed during the “United Nations International Conference on the Peaceful Uses of Atomic Energy” (Geneva, 1958). This event underlines two occurrences:

- The research on fusion reactors has been more difficult than expected in comparison to the fission as applied to civil energy production;
- The research on fusion power generation becomes a global challenge despite the Cold War and the political, economic and technological competition between the Eastern Block and the Western Block.

It is important to underline that the research on plasma physics is not oriented only in thermonuclear applications for power generation, but it is also interested in the understanding of the astrophysical plasmas.

The energy production from nuclear reactions is associated to the missing rest mass between the reagents and the products of the reaction. The energy distribution between the products is associated to the reduced mass of the system assuming a fusion reaction as a collision. The basic idea of fusion is to use light elements and to carry them sufficiently close one to the other in order to obtain a fusion reaction with the production of another nucleus species. The fusion reactions relevant for the power production on Earth involves the fusion of the Hydrogen in its isotopic components:

$$D + D \rightarrow He^3(0.82MeV) + n(2.45MeV) \tag{1.1}$$

$$D + D \rightarrow T(1.01MeV) + H(3.02MeV) \tag{1.2}$$

$$D + T \rightarrow \alpha(3.52MeV) + n(14.06MeV) \tag{1.3}$$

$$D + He^3 \rightarrow \alpha(3.67MeV) + n(14.67MeV) \tag{1.4}$$

The D-D reaction has two branches with the same reaction rate, and is the most desirable in the sense of a virtually unlimited supply of inexpensive fuel, easily extracted from oceans.

The D-He^3 reaction requires the production of He^3 because of its absence on earth. This reaction is interesting thanks to the large amount of energy released, the absence of neutrons that can activate the reactor and the species of the product of reaction. Having charged particles as products allows to confine also the products of the reaction and it also offers the possibility to perform a direct energy conversion to electricity.

The D-T reaction is the most convenient fusion reaction, it produces a large amount of nuclear energy. This reaction is the central focus of worldwide fusion research: the core of ITER proposing is the study of the D-T operation regimes. Some critical issues should be taken into account: the reaction produces high energy neutrons that can not be confined and can induce a material degradation, the use of tritium involves the activation of the reactor (also if its half-life is 12.26 years) and due to its half-life tritium must be produced to fuel the reactors. The solution to breed tritium can be a lithium blanket external to the first wall. The lithium isotopes react with a neutron, depending on the energy level of the neutron, with two different reactions producing tritium.

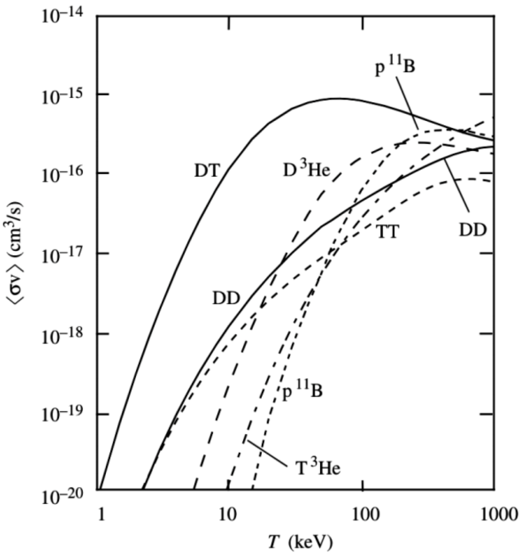

Figure 1.1. Velocity averaged cross section in dependence on temperature.

The fusion nuclear reactions have been introduced as collisions and it has also been presented a scale of increasing activation energy levels required to initiate the different reactions. The cross section σ is a measure of the characteristic area available for interaction between two particles involved in a nuclear reaction. The reaction rate is related to the relative distance between the charged particles and the kinetic energy available to overcome the Coulomb force.

Assuming a Maxwellian distribution for the particle velocity, the velocity averaged cross section is plotted in Fig. 1.1 in function of temperature that identifies the Maxwellian distribution function. The reaction rate between two species can be computed:

$$R_{12} = \int f_1(\mathbf{v_1}) f_2(\mathbf{v_2}) \sigma(|\mathbf{v_1} - \mathbf{v_2}|) |\mathbf{v_1} - \mathbf{v_2}| d\mathbf{v_1} d\mathbf{v_2} = n_1 n_2 \langle \sigma v \rangle \tag{1.5}$$

where f_j, v_j and n_j are respectively the Maxwellian distribution function, the velocity and the density of the species j.

The fusion power can be computed from the fusion reaction rate as:

$$P_{fus} = R_{12}E_{fus} = n_1n_2\langle\sigma v\rangle E_{fus} = n_1n_2\langle\sigma v\rangle\left(E_{fus,C} + E_{fus,N}\right) \tag{1.6}$$

where it may be convenient to separate the specific energy produced by a fusion reaction in the term $E_{fus,C}$ fusion energy component carried by charged particles and $E_{fus,N}$ fusion energy component carried by neutral particles. This is convenient because charged particles can be confined and, therefore, can contribute to plasma heating while neutral particles have limited interactions with the plasma.

The virtually unlimited fuel supply and the efficiency of energy conversion associated to the missing rest mass of fusion reactions make nuclear fusion an attractive energy source.

Despite several decades of studies we must notice that nuclear fusion technology readiness level isn't close to a commercial fusion power plant. Many progresses have been done in solving technological issues and in improving the physics understanding of plasmas, but, according to the European road-map of fusion research, time and experiments are needed to approach the construction of a first demonstrating fusion power plant expected around 2040s. In a recent publication [1], Reinders reviews the status of the research activities on nuclear fusion and exhorts the fusion community to avoid premature announcements on fusion readiness. We do agree with his exhortation.

In this context, it is clear that, in absence of "miraculous progresses", fusion energy can not give its contribution to the energy transition. However, in a long-term strategy we are convinced that fusion energy could be a reliable energy source. It can be envisaged for substituting fission power plants and it can give its contribution to the diversification of the primary energy sources. In a decarbonized power grid, fusion power plants could increase the power supply security compensating the variable energy production from renewable plants. On the other hand, the research on fusion technologies is fundamental for those Countries which have limited energy sources or limited territorial extension for satisfying their energy need.

During the work on this PhD thesis we have assisted to the onset of two global crises: the pandemic due to COVID-19 and the Russian invasion of Ukraine. Both the phenomena could be considered at the beginning as regional stresses but, in the time of few weeks, both have achieved a global dimension. The propagation of these events around the world is still in progress and we may not have a complete understanding of their consequences [2]. We can observe the propagation of the consequences strictly related to the strong interconnections between the economies in the global market. The two crises have impacted on global economy from two different directions: the pandemic has triggered issues in the global supply chain due to the lockdowns in the sites of production (e.g. the shortage of semi-conductors); the invasion of Ukraine has started an energy crisis with the increase of energy prices without a real shortage of energy products [3].

Referring to the European energy market, the European Countries seem to be completely unprepared to the latter occurrence [4]. Moreover, it can be argued that the low prices of the natural gas imported from Russia in the last ten years have enhanced the European energy dependence discouraging investments in renewable energies [3].

These trends need to be changed implementing investments not only in present-days energy facilities but also in the research of alternative energy sources. Fusion may give its contribution to increase the European energy security and resilience to global stresses. This increase in the resilience can come also from the European private companies already involved in the manufacturing and in the research on fusion energy.

With this work we tried to give our contribution to the European framework of fusion research on magnetic confinement.

Chapter 2

The Joint European Torus experiment (JET)

2.1 A brief history of JET

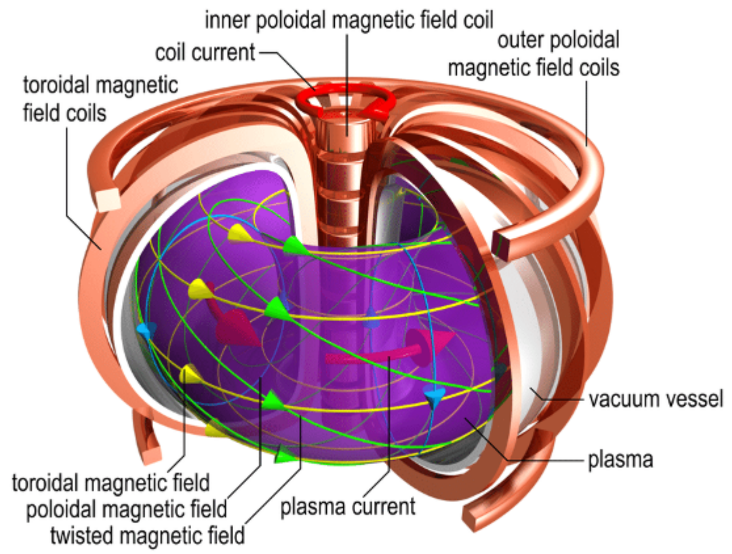

Figure 2.1. Sketch of the Tokamak configuration with the coils and the correspondent induced magnetic fields, plasma current and the total (twisted) magnetic field.

The Tokamak configuration is illustrated in Fig. 2.1. It is a torus-shaped axisymmetric device that uses magnetic field to confine the charged particles of the plasma. The toroidal coils are equally spaced and surround the toroidal chamber generating the toroidal magnetic field. In this configuration the magnets density results higher in the centre of the machine. The resulting gradient in the magnetic filed would be responsible for the onset of particle drifts leading to a charge separation. Therefore, the plasma would not be confined. The charge separation can be can be short circuited with a toroidal plasma current, induced by the central solenoid, which generates a poloidal magnetic field [5]. The composition of the toroidal and poloidal magnetic fields results in a twisted magnetic field (c.f. Fig. 2.1).

In the world, the *Joint European Torus* (JET) [7, 8, 9] is the largest Tokamak in operations and the only one licensed for D-T operations. The design of JET started in September 1973 in a context where the largest existing Tokamak was the *Tokamak de Fountenay-aux-Roses* (TFR) [10], with a plasma volume around $V_{p,TFR} \approx 0.01 V_{p,JET}$ and in absence of a solid background in Tokamak physics. Despite these premises, JET design team concluded the activities in September 1975, presenting a robust design which has allowed JET to operate with minor modifications in regimes not yet observed at the time. A more detailed description of their activities can be found in [8]. For example, the D-shaped cross section has been proposed to reduce the tensile stresses in the toroidal field coils. It was argued in [11] that a vertically elongated plasma cross section may increase plasma performance by reaching a higher β. Since there was not a theoretical agreement, JET design team contemplated operations both with elongated plasmas and with plasma circular cross section. The essential objective of JET individuated in the design phase were: investigate the scaling of plasma behavior as parameters approach the reactor range; the plasma-wall interactions in these conditions; the study of plasma heating; the study of α-particle production, confinement and consequent plasma heating [8].

JET started its operation in 1983 with a limited additional heating power that have been increased in steps until 1986 when Ion Cyclotron Resonance Heating (ICRH) and Neutral Beam Injection (NBI) achieved a nominal additional heating power $P_{aux} = P_{NBI} + P_{ICRH} \approx 24 + 15$ MW [8]. After the discovery of the high confinement mode (H-mode) at *Axially Symmetric Divertor EXperiment* (ASDEX) [12, 13, 14], also JET achieved the access in H-mode adjusting the currents in the external coils to reach the required magnetic geometry. What has been observed in ASDEX, and confirmed by JET, is when increasing the auxiliary heating above a certain threshold the plasma show a spontaneous transition from the low confinement mode (L-mode) to the H-mode. The typical plasma pressure profiles in L-mode and in H-mode are shown in Fig. 2.2. The physics of the L-H transition is still not completely understood. The H-mode is characterized by the presence of an Edge Transport Barrier (ETB) which is commonly referred to as pedestal [15]. The L-H transition strongly suppresses the turbulence close to the last closed magnetic flux surface, called separatrix. The suppression of turbulence results in a region with a stiff pressure gradient and in the occurrence of Edge Localized Modes (ELMs), triggered by Magneto Hydro Dynamic (MHD) instabilities.

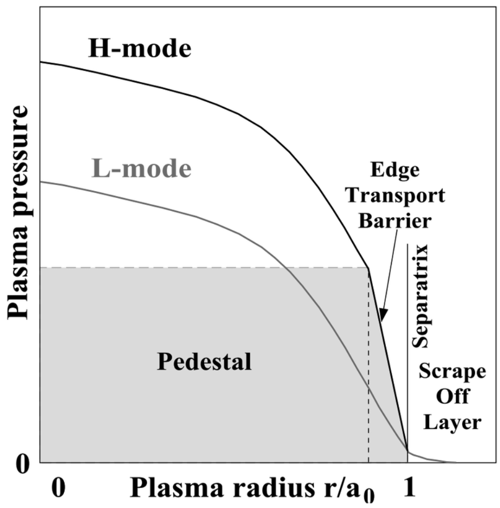

Figure 2.2. Typical plasma pressure profiles in L-mode and in H-mode. The edge transport barrier (ETB) near the last closed flux surface (LCFS), referred to as separatrix, establishes a strong pressure gradient [16].

JET has been equipped with a divertor in 1993. D-shaped plasmas are characterized by the presence of an X-point in the last closed magnetic flux surface. Particles that are loosing confinement can be oriented in specific components designed for exhaust heat management to protect the main chamber wall. The divertor is the Tokamak component devoted to exhaust heat management. An exhaustive discussion on the benefits of the divertor configuration in a Tokamak and about the designing criteria can be found in [17]. The divertor configuration will be crucial in future reactors where the power loads are expected to be severe. The geometry of the divertor configuration needs to be studied in detail not only for the thermo-mechanical limits of the components but also because it plays an important role in the conditions required to access the H-mode, in the reduction of the ionization sources and in the impurity contamination of the plasma.

JET performed a first D-T experimental campaign (DTE1) in 1997 in presence of C-wall and C divertor. After the experimental campaign, the level of T retention in C plasma facing components (PFCs) determined the change of the ITER design with the introduction of a Be wall and a W divertor. In 2011, JET has been equipped with the ITER-like wall (Be/W) and the NBI has been upgraded to a nominal heating power $P_{NBI} = 34$ MW. There are several challenges presented by operations with the ITER-like wall [18]: a general deterioration of the pedestal confinement; the risk of heavy impurity accumulation in the core, which, if not controlled, can cause the radiative collapse of the discharge; the requirement to protect the divertor from excessive heat loads, which may damage it permanently. The campaigns performed until 2020 have been devoted to optimise the plasma scenarios and to recover the C-wall plasma performance in presence of the W sputtered from the divertor. In 2021, JET has operated in D-T main ion plasma composition, in the closest possible conditions to ITER D-T operations. In the next section the D-T campaigns will be presented and compared.

2.2 Deuterium-tritium experiments

JET performed the world's first D-T fusion experiment in 1991. It was limited to two pulses with a T concentration in the main ion plasma composition around 10% and 20% introduced in the torus by the NBI. It produced a peak fusion power $P_{fus} = 1.7$ MW and released 2 MJ of fusion energy.

From 1993 to 1996 the *Tokamak Fusion Test Reactor* (TFTR) [19], located in Princeton, operated in D-T main ion plamsa mixture. In 1994, TFTR achieved the peak fusion power $P_{fus} = 10.7$ MW with an auxiliary heating $P_{aux} = 39.5$ MW (leading to a gain factor $Q = 0.27$) [20]. TFTR demonstated for the first time the tritium handling technology and a reliable plasma heating technology with the ICRH heating scheme for D-T plasmas.

D-T experiments were again performed at JET in 1997. DTE1 aimed at [21]: characterizing the baseline ITER mode of operation in D-T, producing high fusion power and Q, observing α-particle heating and studying the stability of Alfén eigenmodes.

In Fig. 2.3 the fusion power produced in the first experiments at TFTR and at

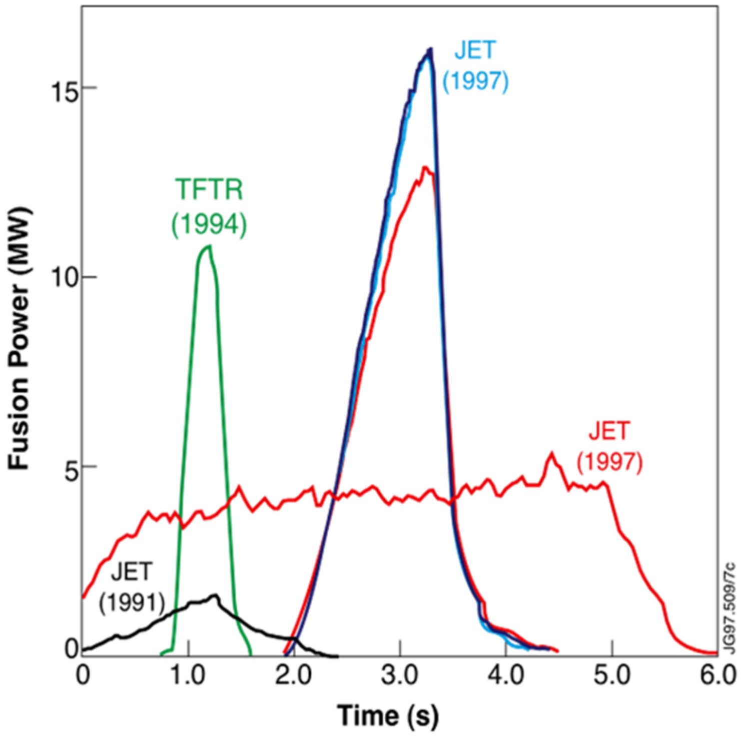

Figure 2.3. Comparison between the fusion power achieved by the first experiments in D-T main ion plasma composition.

JET are compared. During DTE1, JET achieved a record fusion power $P_{fus} = 16.1$ MW with a gain factor $Q = 0.62$ in transient hot-ion H-mode, while the performance achieved in steady state produced a fusion power $P_{fus} = 4$ MW with an ELMy H-mode for a duration of 4 s. An overview of DTE1 experiments can be found in [21] and the analysis of the most performing discharges can be found in [22]. It has been mentioned that at this time JET was equipped with CFC-based plasma facing components and one of the main results was the large retention of T in the wall, which is unacceptable for a reactor, both for nuclear safety and for plasma fuelling control.

The ITER-like wall has been installed at JET between 2009 and 2011 with an increased NBI power and an improved set of diagnostics with respect to DTE1. The activities of JET have been oriented towards optimising the plasma scenarios and dealing with the presence of high radiated power due to the presence of W as impurity species. The DTE2 campaign has been focused on the stationarity of the performance in the closest conditions to the ITER operations in D-T. The DTE2 campaign has been preceded by a wide experimental and modelling activity and this thesis belongs to this framework. For the DTE2 campaign the following scientific goals have been proposed in [23] and in [24]: demonstrating high fusion power up to 15 MW sustained for 5 s, demonstrating clear alpha particle effects, clarifying the isotope effect on energy and particle transport, exploring the consequences of mixed plasma species, addressing key plasma-wall interaction issues, demonstrating ITER-relevant ICRF schemes and demonstrating ITER-like integrated plasmas.

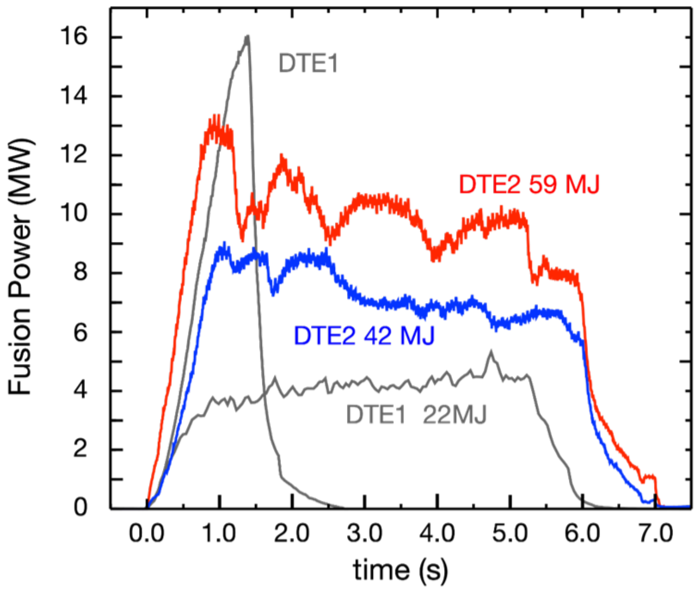

Figure 2.4. Achieved fusion power at JET during DTE1 (grey) and in DTE2 with hybrid scenario (blue) and optimised fuel mix scenario (red).

In Fig. 2.4 the record pulses performed at JET in DTE1 and DTE2 are compared. It can be seen that in terms of achieved fusion power and, consequently, fusion energy produced in 5 s long pulses, in DTE2 there is a significant improvement with respect to the results obtained in DTE1. The different aspects cited in the aims of DTE2 are strictly interconnected and the high performance scenarios integrate the information and the results form different research areas. In the next section the different plasma scenarios will be introduced in order to understand the peculiarities of each scenario.

2.3 Plasma scenarios in preparation to D-T operations at JET

In preparation to DTE2, a vast activity of scenario development has been undertaken at JET since 2016 [18]. To maximise the thermal reactivity of a D-T plasma, the concentration has to be close to 50-50. The scenarios studied in preparation of DTE2 are the *baseline* scenario and the *hybrid* scenario both prepared in presence of balanced D-T neutral beam injection. At JET the beam-thermal component of D-T reactions can be used to maximise the fusion power, and with this approach an *optimised fuel mix* scenario has been prepared too.

The *baseline* scenario ($\beta_N \approx 1.8$, $q_{95} \approx 3$) is a ELMy H-mode where good confinement relies on high plasma current ($I_p \geq 3.5$ MA) and high magnetic field with a relaxed plasma current profile.

The *hybrid* scenario ($\beta_N \approx 2-3$, $q_{95} \approx 4$) is a ELMy H-mode where good confinement is achieved at higher β_N and lower current ($I_p \leq 2.5$ MA) through a shaped current density profile, allowing to achieve an on-axis safety factor $q_0 > 1$.

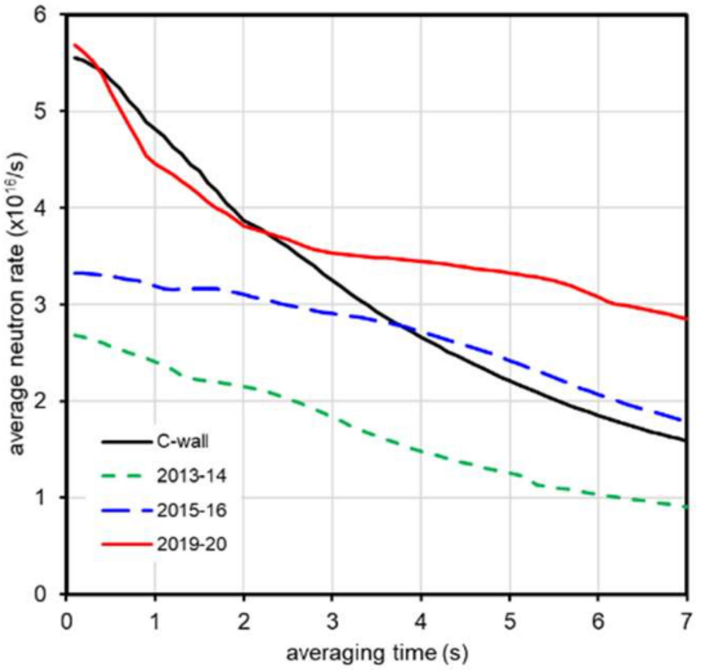

Figure 2.5. Average neutron rate for different campaigns in the JET-ILW and comparison to maximum values obtained during JET C-wall operations [25]

During the optimization in preparation to DTE2, both *hybrid* and *baseline* scenarios achieved a similar performance in D plasmas. Some differences can be found comparing the stored energy (higher in *baseline*), which can be considered an evidence of achieving better confinement. It can also be argued that the two scenarios show a similar neutron yield with a different stored energy, suggesting a better conversion of stored energy into fusion power in the *hybrid* scenario. However, the two scenarios are complementary, and were expected to reach both a stationary high fusion performance with a confinement enhancement factor $H_{98} > 0.9$ and a stored energy $W_{th} \approx 10 - 12$ MJ.

The results of the intense activity of scenario optimization in preparation to D-T operations are presented in Fig. 2.5. It can be seen how the average neutron rate has been increased recovering the peak values of the experiments carried out in presence of C-wall, and exceeding the performance in pulses longer than 3 s [25].

Starting from the *hybrid* scenario, the *optimized fuel mix* scenario has been prepared to increase the beam-thermal target component of fusion reactions. The dependence of fusion power on main ion plasma composition in presence of pure D beams can be seen in Fig. 2.6. This scenario consists of a T plasma heated by pure D NBI, the main ion plasma composition depends on the fuelling determined by T gas puff and D beams. A *caveat* before the beginning of the experiments in D-T plasma mixture is related to the difficulties in sustaining a T rich plasma for a sufficient time. Nevertheless, the *optimized fuel mix* scenario produced in DTE2 the world's fusion record with 59 MJ of fusion energy, with a beam target component of the fusion reactions around 75%. Therefore, this operating regime is not relevant for future reactors where the thermal component of fusion reactions must be dominant and additional heating systems are envisaged to help the ramp-up phase, to help the control of plasma instabilities and to contribute to the fuelling control of the machine. In today experiment it can help on investigating the effects related to the presence of α-particles in the plasma.

The work of this thesis focus on the *baseline* scenario as a reference for the plasma operating conditions. With the integrated modelling, different scenarios in different plasma operating conditions can be developed and compared before the plasma operations. The aim of this approach is the development of a virtual Tokamak machine, where the evolution of the plasma can be studied consistently with the expected experimental boundary conditions. The transport models are crucial for describing the plasma profiles evolution, while other modules are using the plasma profiles as an input to compute the external particle and energy sources related to different phenomena. We will start presenting a systematic analysis and validation of the first principle transport models in D *baseline* plasmas. This is needed to test the reliability of the models in the desired operating conditions, and then we will present the results expected in slightly different operating conditions together with the sensitivity of the scenario to the expected experimental conditions. It has to be mentioned that energy and particle turbulent transport is still not completely understood. As a consequence, transport models must be used carefully when exploring new operative conditions, keeping into account theirs limits of validity.

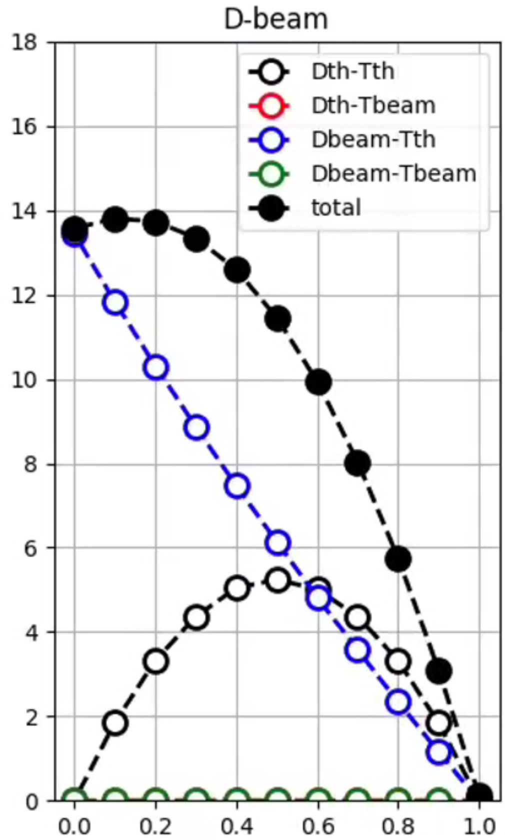

Figure 2.6. Fusion power in dependence on D concentration in presence of pure D beams: (black with solid markers) total fusion power, (black with open markers) D-T thermal component, (blue with open markers) beam-thermal target component.

Chapter 3

Transport simulations: theoretical background and codes

3.1 Introduction to transport

The aim of fusion research is to achieve the conditions for a self sustained burning plasma. Form the power balance and the ignition condition the Lawson criterion can be obtained [5]:

$$\frac{P_C}{P_L} \geq 1 \implies n\tau_E \geq \frac{12}{E_{fus,C}} \frac{T}{\langle \sigma v \rangle} \equiv F(T) \tag{3.1}$$

where P_C is the specific fusion power carried by charged particles, P_L is the specific power related to the loss processes, n is the electron density, τ_E is the energy confinement time, $E_{fus,C}$ is the fusion energy component carried by charged particles and $\langle \sigma v \rangle$ is the reaction cross section distribution which is a function of the temperature. The energy confinement time can be defined as follow:

$$\tau_E = \frac{W_{th}}{P_h - (dW_{th}/dt)} \tag{3.2}$$

where W_{th} is the plasma stored energy and P_h the heating power.

Transport plays a crucial role in determining the energy confinement time. The most relevant transport mechanisms are thermal diffusion and particle diffusion. The transport is driven by temperature gradients, density gradients, the onset of MHD instability modes and micro-instabilities related to plasma turbulence. The transport can be evaluated by the random walk model, with transport coefficients having the dimensions of a squared characteristic length over a characteristic time $[L^2]/[T]$. The transport problem can be solved in a local expression between the fluxes which are the effects of the presence of gradients through a transport coefficient, hence the particle flux Γ and the heat flux q can be written as:

$$\Gamma = -D\nabla n + Vn \tag{3.3}$$

$$q = n\chi\nabla T \tag{3.4}$$

where D is the particle diffusivity, V is the particle convection and χ is the thermal diffusivity. Similar local expression can be defined for the other relevant quantities such as momentum and plasma current.

Conventionally, the transport mechanisms (and coefficients) have been divided in three categories:

Classical transport: related to the collision effects in a cylindrical geometry;

Neoclassical transport: related to collision effects in toroidal geometry, including the interaction between trapped particles (in banana orbits) and passing particles; this component, which is including classical transport effects, represents the minimum level of transport in a Tokamak.

Anomalous transport: related to turbulence, i.e. the non-linear interaction of instability fluctuations generated in the plasma.

In Tokamak devices the heat and particle transport parallel to the magnetic field lines is sufficiently fast so that the pressure can be considered constant on the magnetic flux surfaces. Taking into account the axisymmetry in the toroidal direction, the macroscopic quantities, such as density and temperature, represent flux surface averages which depend only on the radial variable. The plasma geometry is determined by the 2D distribution of the poloidal magnetic flux $\Psi(R, Z)$, which is a solution of the Grad-Shafranof equilibrium equation [26]:

$$\Delta^* \Psi = -4\pi \left(\mu R^2 \frac{\partial p}{\partial \Psi} + I \frac{\partial I}{\partial \Psi} \right) \tag{3.5}$$

where the Grad-Shafranof operator is defined as $\Delta^* = R^2 \nabla \cdot (1/R^2 \nabla)$, R is the radial distance from Tokamak axis, Z the vertical distance from the horizontal plane, p is the plasma pressure and I the diamagnetic current. In applications, are often used the normalised poloidal or toroidal fluxes, for example the normalised toroidal flux is defined $\rho_{tor} = (\psi_{tor}/\psi_{tor,LCFS})^{1/2}$, where the Last Closed Flux Surface (LCFS) is the most external magnetic surface that does not intersect with the wall.

The presence of Coulomb collisions leads to radial transport. The transport equations describe the temporal and spatial evolution of densities and temperatures in presence of external and internal sources and sinks of particles and energy [27]. In interpretative simulations, assuming the external sources (or sinks), the transport codes can solve the transport equations (energy and particle balance) and determine the transport coefficients. In predictive simulations, assuming the external particle sources (or sinks) and the plasma kinetic profiles, the evolution of the plasma kinetic profiles can be predicted using a transport model to compute the transport coefficients. In the experiments, it has been seen that the "measured" transport (computed by means of interpretative simulations) is significantly higher (an order of magnitude at least) of the neoclassical transport. Therefore, anomalous or turbulent transport is dominant in Tokamaks and is responsible for the degradation of the energy confinement time τ_E. It goes without saying that in predictive simulations the choice of turbulent transport model is determinant for achieving reliable results. Different transport models are available for this purpose, the choice of the model depending on the desired degree of accuracy and on the available computing time for the analysis. The transport models can be empirical or first principle. Empirical transport models are obtained with experimental scalings and use simplified relations in terms of plasma parameters to determine the transport coefficients. First principle transport models compute the transport coefficients from theory based relations.

3.2 The kinetic equations

A first approach to the problem may be microscopic: for each particle one should write the equation of motion in externally imposed electromagnetic fields and in the fields generated by particles themselves, and then solve the equations. Since the number of confined particles in a Tokamak plasma is of the order of 10^{22}, mutually interacting, it is computationally impossible [5]. A suitable approach is the one of kinetic theory, which still describes the plasma in terms of the particles motion but, because of the large number of particles involved, the description has to be statistical, solving the particles motion equations in terms of kinetic distribution functions. The basic equation of kinetic theory is the Boltzmann equation [5]:

$$\frac{\partial f_{e,i}}{\partial t} + \frac{\partial f_{e,i}}{\partial \mathbf{r}} \cdot \mathbf{v} + \frac{\partial f_{e,i}}{\partial \mathbf{v}} \cdot \mathbf{a} = \left(\frac{\partial f}{\partial t}\right)_{coll} \tag{3.6}$$

To determine the final form of the equation, one needs to specify the fields $\mathbf{E}$, $\mathbf{B}$ and an expression for the collisional term $\left(\frac{\partial f}{\partial t}\right)_{coll}$. Therefore, kinetic equations and Maxwell equations must be solved simultaneously. This equation describes the evolution of the distribution function $f_{e,i}(\mathbf{r}, \mathbf{v}, t)$ for electrons and ions under the effect of long-range electric and magnetic fields $\mathbf{E}$ and $\mathbf{B}$. The choice of the distribution function f, that defines the probability density of a particle in a 6D space $(\mathbf{r}, \mathbf{v})$ and the time dependencies, is arbitrary, but it must satisfy the possibility of obtaining macroscopic quantities by integrating microscopic quantities. As a first approximation we can assume that the distribution function in a plasma is the Maxwell-Boltzmann distribution.

Neglecting the collisionality term in Boltzmann equation 3.6, the Vlasov equation can be derived:

$$\frac{\partial f_{e,i}}{\partial t} + \frac{\partial f_{e,i}}{\partial \mathbf{r}} \cdot \mathbf{v} + \frac{q_{e,i}}{m_{e,i}}(\mathbf{E} + \mathbf{v} \times \mathbf{B})\frac{\partial f_{e,i}}{\partial \mathbf{v}} = 0 \tag{3.7}$$

where m indicates the particle mass and q indicates the particle charge. The approximation of low collisionality is generally justified in magnetically confined plasmas, since the collision frequency is low at high temperatures and low densities, being $\nu \approx n/T^{1.5}$.

From the Boltzmann equation 3.6 the collisional term in a plasma can be derived under the simplified hypothesis that the majority of collisions are small-angle deflections [5]. In a plasma we have many long-range small-angle Coulomb collisions which are more efficient in changing particles momentum than hard-sphere collisions. We can then define the following parameters, function of the averages of velocity fields [5]:

$$A_i = \frac{\langle \Delta v_i \rangle}{\Delta t} - \frac{1}{2}\frac{\partial}{\partial v_j}\frac{\langle \Delta v_i \Delta v_j \rangle}{\Delta t} \tag{3.8}$$

$$D_{ij} = \frac{\langle \Delta v_i \Delta v_j \rangle}{\Delta t} \tag{3.9}$$

The Fokker-Plank collisionality term can be defined as [5]:

$$\left(\frac{\partial f}{\partial t} \right)_{coll} = -\frac{\partial}{\partial v_i}(A_i f) + \frac{1}{2} \frac{\partial}{\partial v_i} \left(D_{ij} \frac{\partial f}{\partial v_j} \right) \tag{3.10}$$

The first term on the RHS is a dynamic friction coefficient and represents the loss of momentum of a particle species via collisions with other particles of the same species or different one. The second term on RHS describes a flux in the velocity field.

3.3 The gyrokinetic approach

The gyrokinetic formulation represents a way of simplifying the kinetic equations in plasma physics and reducing the phase space of dimensionality in which the distribution function exists. In this approach, the particle motion is described averaging it over the fast Larmor motion. Inside the plasma there are phenomena which are slow compared to the fast gyro-motion of charged particles around magnetic field lines and which vary slowly in space compared to the Larmor radius of ions and electrons. This equations are called “gyro-averaged kinetic equations”. The advantage lies in the reduced dimensionality of the phase space, that goes from the six dimensions of the Vlasov equation to the five of gyro-averaged equations: three for space, one for the velocity parallel to toroidal magnetic field B_T and one for the magnetic moment ($\mathbf{r}$, $v_\parallel$, μ).

Gyrokinetic transport models are the golden standard of the state of the art. They take into account a variety of drift-wave instabilities such as Ion Temperature Gradient (ITG) driven mode, Electron Temperature Gradient (ETG) driven mode, and Trapped Electron Mode (TEM), which are the most significant instabilities in Tokamak core plasmas [28]. Kinetic Ballooning Modes (KBM) [29] and MicroTearing Modes (MTM) [30] are predicted in the pedestal region in H-mode, a narrow band towards the plasma edge where turbulence is stabilized due to strong rotation shear flows [31, 32, 33]. KBM is also predicted in the core of high poloidal-β scenarios with relatively low plasma current [34]. Resistive Ballooning Modes (RBM) [35] are predicted in the high-collisionality L-mode edge.

A high-fidelity first-principles approach to gyrokinetics involves calculating the full distribution function for the entire radial extent of the plasma selfconsistently [28]. Unfortunately the time computational expense is highly challenging, and further approximations might be considered. Instead of considering the entire tokamak, it is useful to limit the analysis to a narrow annular section. This is referred to as the flux tube approximation. The background temperature, density and rotation are described by their value at the central flux surface of the annulus and are fixed in time. Since the gradients provide the drive for the instabilities, simulations of this kind are said to be gradient driven. The constant gradients allow for a spectral (Fourier) decomposition of the spatial domain in the directions perpendicular to the magnetic field, employing cyclic boundary conditions. This significantly accelerates the computations [28]. Usually the magnetic equilibrium is not solved, but prescribed in gyrokinetic simulations. Assuming that the radial transport can provide enough time to the collisions to keep the plasma close to a Maxwell equilibrium, the distribution function can be expressed locally as $f = f_0 + \delta f$, where f_0 is the Maxwell distribution and δf is the perturbation. Similar expansions are adopted for the fields $\mathbf{E}$ and $\mathbf{B}$. With this approach, for each perturbation the growth rate can be computed in non-linear simulations. If the sources (or sinks) have been used as an input for the simulations, the determination of the grow rates corresponds to the determination of the fluxes. The transport equations can be solved obtaining the evolution of the computed quantities. The relaxation of the solutions requires a time scale of few confinement times, but the computing time is still prohibitive (e.g. 10^8 CPUh would be necessary to predict temperature and density profile over a range of an energy confinement time [28]). This leads to the need of reduced first principle transport models that will be introduced in the next sections.

3.4 The fluid equations

In order to perform global plasma simulations there is the need of the fluid approximation. The base of the fluid model is to take the plasma and divide it in a large number of small fluid elements, each one containing enough particles so that statistical averages can be defined. However, the size of the fluid element must not be too large or the spatial resolution could be lost and the accuracy of the model reduced. For example, if we imagine a plasma with a number density of 10^{20} m^{-3}, a fluid element that satisfies both conflicting requirements is one with a characteristic dimension $\Delta x = 10^{-5}$ m and a number of particles of about $N = nV = 10^{20}10^{-15} = 10^5$, which is high enough for statistical purposes and has a good spatial resolution (typical tokamak dimensions ≈ 1 m).

The goal of the model is to write a set of coupled non-linear partial differential equations which describe the evolution of macroscopic quantities in the plasma: $n_e(\mathbf{r}, t)$, $n_i(\mathbf{r}, t)$, $\mathbf{u_e}(\mathbf{r}, t)$, $\mathbf{u_i}(\mathbf{r}, t)$, $p_e(\mathbf{r}, t)$, $p_i(\mathbf{r}, t)$, $T_e(\mathbf{r}, t)$, $T_i(\mathbf{r}, t)$. The full set of the two fluid model (for electrons and ions) consist of:

$$\frac{\partial(mn)}{\partial t} + \nabla \cdot \mathbf{\Gamma} = S_p \tag{3.11}$$

$$\frac{\partial \mathbf{v}}{\partial t} + (\mathbf{v} \cdot \nabla)\mathbf{v} + \frac{1}{mn}\nabla p - \mathbf{F} = \mathbf{S_m} \tag{3.12}$$

$$mn\left(\frac{\partial \epsilon}{\partial t} + \mathbf{v} \cdot \nabla \epsilon\right) - \nabla \cdot \mathbf{q} + p\nabla \cdot \mathbf{v} = S_E \tag{3.13}$$

where in the conservation of mass 3.11 $\mathbf{\Gamma}$ is the particle flux and S_P are the particle sources; in the conservation of momentum 3.12 p is the pressure and $\mathbf{S_m}$ are the external sources of momentum; in the conservation of energy 3.13 ϵ is the internal energy per unit mass, $\mathbf{q}$ is the heat flux and S_E the external energy sources. The set of two fluid equations is closed with the Maxwell equations:

$$\nabla \times \mathbf{E} = -\frac{1}{c}\frac{\partial \mathbf{B}}{\partial t} \tag{3.14}$$

$$\nabla \times \mathbf{B} = -\frac{4\pi}{c}\sum_s \mathbf{j_s} + \frac{1}{c}\frac{\partial \mathbf{E}}{\partial t} \tag{3.15}$$

$$\nabla \cdot \mathbf{E} = 4\pi \sum_s e_s n_s \tag{3.16}$$

$$\nabla \cdot \mathbf{B} = 0 \tag{3.17}$$

The set of equations is complete and the solutions can be obtained independently of the transport model in use. In interpretative simulations, assuming the external sources and the experimental kinetic profiles of plasma, we can obtain the experimental fluxes and experimental transport coefficients. In predictive simulations, the external sources are assumed, the transport model computes the transport coefficients or the fluxes and the time evolution of the quantities of interest can be determined. In the next sections we will present two examples of anomalous transport models: the empirical model Bohm gyroBohm and the reduced first principle model QuaLiKiz

3.5 The Bohm gyroBohm model

The turbulent transport can be evaluated in first approximation with the Bohm gyroBohm model. The Bohm transport is driven by severe macroscopic instabilities while the gyroBohm transport component is related to small-scale fluctuations in the order of magnitude of the ion Larmor radius. This is an empirical model validated on the results of a vast number of JET pulses, suitable for fast simulations, utilised in this thesis to check the consistency of experimental initial and boundary conditions.

Bohm diffusivities are typically characterized by a term proportional to the temperature and inversely proportional to the magnetic field: $\chi_{Bohm} \propto T/B$. The Bohm transport coefficients can be expressed as follow [36, 37]:

$$\chi_{e,Bohm} = C_1 \cdot \frac{T_e}{B_0}\frac{a_0|\nabla p_e|}{p_e} \cdot q^2 \tag{3.18}$$

$$\chi_{i,Bohm} = 2 \cdot \chi_{e,Bohm} \tag{3.19}$$

where C_1 is the empirical constant chosen for reproducing the experimental results, p_e is the electron pressure, a_0 is the Tokamak minor radius and q is the safety factor.

The structure of the gyroBohm transport coefficients can be derived from the assumption, that the typical time scale of microinstabilities is in the order of the diamagnetic drift frequency $\omega_{*i} = k_y u_{*i}$, where the mode number $k_y \sim 1/\rho_i$ [26]:

$$\chi_{gyroBohm} \sim \frac{\Delta x^2}{\Delta t} \sim \rho_i^2 \omega_{*i} \sim \rho_i \frac{\nabla p}{q_i n_e B_0} \tag{3.20}$$

Under the conditions of flat density profiles and $T_e \sim T_i$ the gyroBohm component can be expressed as [26]:

$$\chi_{e,gyroBohm} = \chi_{i,gyroBohm} = C_2 \cdot \frac{a_0|\nabla T|}{B_0} \cdot \rho_* \tag{3.21}$$

where $\rho_* = (m_i T_e)^{0.5}/q_i B_0$.

To emulate the reduction of Bohm transport in H-mode, a non-local multiplier can be introduced close to the plasma edge, which is an average of the inverse of the electron temperature gradient length.

The particle diffusivity is defined as the harmonic mean of the electron and ion heat diffusivities [26].

3.6 The QuaLiKiz transport model

It has been mentioned that even when introducing the gyrokinetic approximation the computing time is still significantly expensive and does not allow for global plasma simulations. A significant decrease in the computation time can be obtained introducing the quasi-linear approximation. The $\mathbf{E} \times \mathbf{B}$ nonlinearity is ignored and are taken into account only the linearly unstable modes. The non-linear fluxes are computed applying a series of *saturation rules* extracted by studying the saturation mechanism in non-linear simulations. The quasilinear approximation is satisfied if the plasma fluctuations in the long-wavelength transport-driving region maintain their linear characteristics [28].

In this thesis we used extensively the transport model QuaLiKiz [41, 42], while TGLF [38] has been used only for benchmarking purposes. QuaLiKiz is an electrostatic quasi-linear gyrokinetic code, where magnetic perturbations are ignored. On the contrary magnetic perturbations are taken into acoount in TGLF, which is a gyrofluid electromagnetic code. TGLF solves the Gyro Landau Fluid equations for the linear eigenmodes (growth rates and frequencies) of the gyrokinetic instabilities such as ETG, ITG, TEM and KBM. For a more detailed description of the TGLF implementation are available the references [38, 39, 40]. Here we will present only the QuaLiKiz transport model.

In QuaLiKiz the significant decrease in the computation time, with respect to non-linear gyrokinetic simulations, is achieved using the following assumptions:

1. QualiKiz uses the lowest orer balloning transformation to simplify the axisimmetric gyrokinetic problem;

2. The eigenvalues are solutions of a linear gyro-kinetic equation, whereas the eigenfunctions are solutions of the fluid limit of the same equation, i.e. QuaLiKiz accounts for all the unstable modes [43];

   - the eigenvalues are decoupled from the computation of the eigenfunctions;
   - the non-linear effects in the eigenvalues computation are neglected;

3. The distribution function can be decomposed with the gyrokinetic approximation $f_s = f_{0,s} + \delta f_s$ with:

$$f_{s,0} = n_s \frac{1}{(2\pi m_s T_s)^{3/2}} e^{-E/T_s} \tag{3.22}$$

   where n_s, m_s, T_s are the density, the mass and the temperature of the s-species, and E is the kinetic energy of a particle in thermodynamic equilibrium

4. In QuaLiKiz the electrostatic limit is assumed, which is valid for low β plasmas [41]:

   the electrostatic potential can be casted as: $\phi = \phi_0 + \delta\phi$

5. Assuming the Maxwellian distribution function to the lowest order, the collisional term in the kinetic equation 3.6 is zero $\left(\frac{\partial f}{\partial t}\right)_{coll} = 0$:

   $\implies$ QuaLiKiz solves the Vlasov equation.

6. the Vlasov equation is linearized assuming harmonic perturbations for both the distribution function and the electrostatic potential [41]:

$$\delta f = \sum_{\mathbf{n}\omega} f_{\mathbf{n}\omega} \mathbf{J} e^{i(\mathbf{n}\cdot\theta - \omega t)} \tag{3.23}$$

$$\delta\phi = \sum_{\mathbf{n}\omega} \phi_{\mathbf{n}\omega} \mathbf{J} e^{i(\mathbf{n}\cdot\theta - \omega t)} \tag{3.24}$$

   where $\mathbf{J}$ and θ are respectively the action and angle variables, $\mathbf{n}$ is the associated wave vector and ω is the frequency of the perturbation. The linearized Vlasov equation can be expressed as:

$$f_{\mathbf{n}\omega}(\mathbf{J}) = -\frac{f_0(\mathbf{J})}{T_s}\left(1 - \frac{\omega - \mathbf{n}\cdot\omega_{\mathbf{s}}^* - \mathbf{n}\cdot\omega_{\mathbf{E}}}{\omega - \mathbf{n}\cdot\mathbf{\Omega_J} + i0^+}\right) e_s \phi_{\mathbf{n}\omega}(\mathbf{J}) \tag{3.25}$$

   where e_s the charge of the species s and $\mathbf{n}\cdot\mathbf{\Omega_J}$ includes the effect of Doppler frequency shift due to the curvature $\nabla_\perp B$ drifts; ω_s^* is the diamagnetic frequency and the term $\mathbf{n}\cdot\omega_{\mathbf{E}}$ accounts for the $\mathbf{E}\times\mathbf{B}$ drift.

7. The quasineutrality is in its weak formulations:

$$\sum_s \mathcal{L}_s(\omega, \mathbf{n}) = 0 \tag{3.26}$$

   being $\mathcal{L}_s$ the Lagrangian defined for each species. The quasineutrality weak formulation is valid only in the electrostatic case because the relevant wavelength are larger than the Debye length [41].

Combining the equations 3.25 and 3.26 the following dispersion relation can be obtained [41]:

$$\sum_s \frac{e_s^2 f_0^s}{T_s}\left[\langle\phi_{\mathbf{n}\omega}\phi_{\mathbf{n}\omega}^*\rangle - \langle\frac{\omega - \mathbf{n}\cdot\omega_{\mathbf{s}}^* - \mathbf{n}\cdot\omega_{\mathbf{E}}}{\omega - \mathbf{n}\cdot\mathbf{\Omega} + i0^+}\phi_{\mathbf{n}\omega}\phi_{\mathbf{n}\omega}^*\rangle\right] = 0 \tag{3.27}$$

where the averages are performed over the action and the angle variables, therefore this lead to 6D integrals. It can be reduced to 5D with the assumption of toroidal axisymmetry and then to 4D thanks to the gyrokinetic assumption of fast cyclotron gyration $\frac{\omega}{\omega_c} \ll 1$. With the ballooning approximation, the dispersion relation is reduced to 2D, because the dynamics along the field lines is faster than the perpendicular ($k_{||} \ll k_\perp$). The only unknown is the complex mode frequency ω, under the assumption of small perturbation the problem can be solved in the frequency spectrum and it appears as an eigenvalue. For each solution ω_k the linear response can be calculated for the desired poloidal wavenumber k. The quasilinear fluxes are calculated summing the linear responses. As an example the particle flux is evaluated as:

$$\Gamma_s = -\sum_j \frac{k_\theta}{Z_s B} |\phi_k|^2 L_{s,k,0} \tag{3.28}$$

where k are the wavenumbers associated to ω and $L_{s,k,0}$ is the linear saturated response. The saturated potentials ϕ_k can not be calculated in quasilinear approximation so they are assumed in the form:

$$|\phi_k|^2 \propto C_{NL} \left[\frac{\gamma_k}{k_\perp^2}\right]_{max} \frac{B}{k_{\theta,max} R_0} \frac{T_e}{q_e} \tag{3.29}$$

where C_{NL} is the only parameter in the model fitted to reproduce the turbulent spectrum computed by nonlinear simulation [28].

QuaLiKiz transport model has been validated extensively against nonlinear gyrokinetic simulations in [43, 41, 44, 45] showing a good agreement with high fidelity gyrokinetic codes. The significant speed up in the computation time, a factor ≈ 100 with respect to nonlinear simulations, allows QuaLiKiz to be used as reduced first principle transport model in fluid transport codes.

3.7 Integrated modelling in JINTRAC

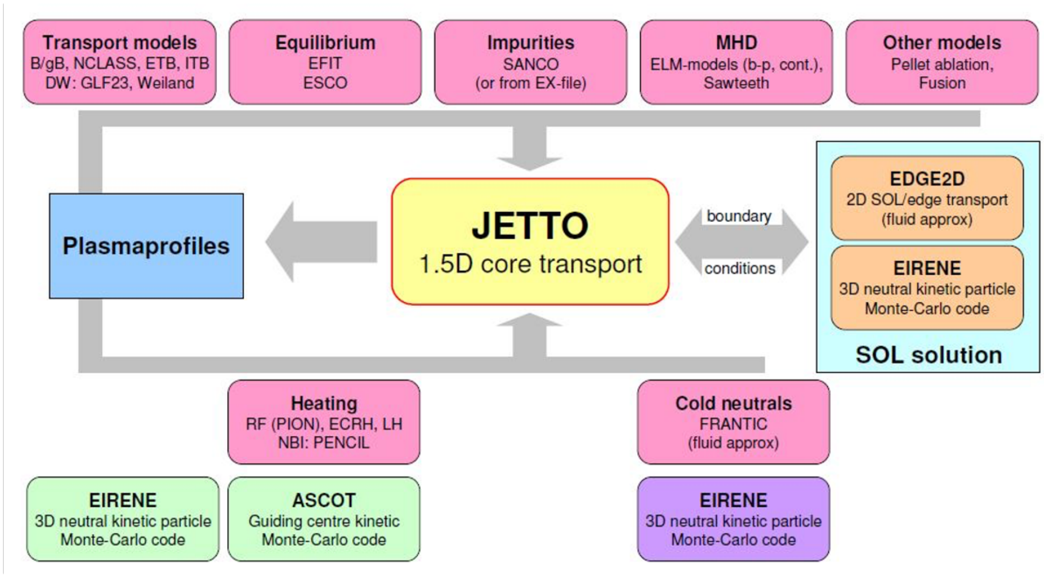

Figure 3.1. Schematic of JINTRAC suite of codes with the available modules [46].

When we are referring to the integrated modelling we are considering the possibility of simulating the plasma evolution consistently with the evolution of multiple mutually interacting phenomena. JINTRAC (Jet INtegrated TRAnsport Code) [46] is the suite of codes in use at JET, a schematic of JINTRAC can be seen in Fig. 3.1. The 1.5D transport code JETTO [47] is the core of the suite of codes. It can be defined 1.5D code because transport equations are averaged over the magnetic flux surfaces, while the informations on plasma geometry are incapsulated in the equilibrium modules by means of solving the Grad-Shafranof equation as mentioned in Sec. 3.1. The main equations solved by JETTO are [47]:

$$\frac{3}{2}\left(\frac{dV}{d\rho}\right)^{-\frac{5}{3}}\frac{\partial}{\partial t}\left[\left(\frac{dV}{d\rho}\right)^{\frac{5}{3}}n_eT_e\right]+\left(\frac{dV}{d\rho}\right)\frac{\partial}{\partial t}\left[\frac{dV}{d\rho}\langle\nabla p\rangle^2\left(q_e+\frac{5}{2}T_e\Gamma_e\right)\right]=\langle P_e\rangle \tag{3.30}$$

$$\frac{3}{2}\left(\frac{dV}{d\rho}\right)^{-\frac{5}{3}}\frac{\partial}{\partial t}\left[\left(\frac{dV}{d\rho}\right)^{\frac{5}{3}}\sum_j^{n_H}n_jT_j\right]+\left(\frac{dV}{d\rho}\right)\frac{\partial}{\partial t}\left[\frac{dV}{d\rho}\langle\nabla p\rangle^2\left(\sum_j^{n_H}q_i+\frac{5}{2}T_i\Gamma_i\right)\right]=\langle P_i\rangle \tag{3.31}$$

$$\left(\frac{dV}{d\rho}\right)^{-1}\frac{\partial}{\partial t}\left[\left(\frac{dV}{d\rho}\right)^{-1}n_s\right]+\left(\frac{dV}{d\rho}\right)\frac{\partial}{\partial\rho}\left(\frac{dV}{d\rho}\langle\nabla p\rangle^2\Gamma_s\right)=\langle S_s\rangle \tag{3.32}$$

$$\frac{\partial\psi}{\partial t}=\frac{A\eta_{||}}{\rho\mu_0}\frac{\partial}{\partial\rho}\left(K\frac{\partial\psi}{\partial\rho}\right)+\frac{V'\eta_{||}}{2\pi\rho}(j_{bs}+j_{cd}) \tag{3.33}$$

where V is the plasma volume, $\rho=(\phi/\pi B_0)^{0.5}$ is the native JETTO coordinate (the normalized toroidal flux), the Γ are the heat or particle fluxes and P, S_s are the heat and particle sources (or sinks). In Eq. 3.30 and in Eq. 3.31 JETTO solves the thermal energy equation, respectively for electrons and ions. The Eq. 3.32 is the mass conservation, solved for each hydrogen isotope (up to two different isotopes). The particle balance of electrons is obtained from the particle balance of all the ions, i.e. main plasma ion species and impurities (if modelled), using the quasi-neutrality. The Eq. 3.33 is the current diffusion equation solved under the hypothesis of the Neoclassical model, where $\eta_{||}$ is the plasma resistivity along the magnetic field, and A and K factors are incapsulating the informations on plasma geometry.

In order to evolve the plasma kinetic profiles, the transport models available in JINTRAC use the kinetic profiles to compute the fluxes. The fluxes are an input for JETTO equations to evolve the kinetic profiles in the following time step. The sources in JETTO equations are computed by the different modules. Here we are presenting the relevant modules used during the work presented in this thesis:

- **PENCIL** [48]: computes the heating, particle, torque and current deposition profiles from the NBI injection. Each beam is represented by a grid and the attenuation coefficients are computed through ADAS [49]. The Fokker-Plank equation is solved for each flux surface to compute the fast ions distribution. Toroidal electric field and bulk plasma rotation effects on the fast ions are neglected; the current drive is obtained as in [50].

- **PION** [51]: reproduces the analytical results with a parametrization of LION [52] to compute the heating deposition and the current drive from the Ion Cyclotron Resonance Heating (ICRH). The Fokker-Plank equation is solved on each flux surface to compute the competition between ion cyclotron absorption and electron Landau damping. When used in JINTRAC with PENCIL it improves the calculation of the fast ion slowing down and takes into account the synergies between the NBI and the ICRH [53]. The full distribution function is taken into account and the cross sections for D-D and D-T reactions are taken from [54].

- **FRANTIC** [55]: computes the neutral particle sources from the separatrix. Modelling an isotropic neutral source electron and ion ionization sources are computed by charge exchange. The neutral transport is approximated by a set of algebraical equations assuming the plasma cross section to be circular. FRANTIC has been validated against more complex codes for the computation of the neutral fluxes from the separatrix, showing a good agreement with the results produced by EIRENE [56].

- **SANCO** [57]: evolves the impurity transport, it calculates the ionization states and the radiated power. The impurities ionization, recombination and charge exchange are computed using multiple ADAS [49] database depending on the impurity species. The conservation of mass equation is solved for each impurity species and for all the ionization stages. Irregular grids are available to increase the spatial resolution towards the plasma edge, initial conditions can be imposed both in terms of impurity density profiles and in terms of relative impurity concentration and Z_{eff}.

- **ESCO** [58]: it solves the Grad-Shafranov equation reading from JETTO the plasma pressure profile and the plasma current. ESCO requires the boundaries of the equilibrium as an input, the boundary can be imposed from experiments by EFIT [59] or other equilibrium solvers such as CREATE-NL [60].

A more detailed description of the code integration in JINTRAC and the references for all the available models can be found in Ref. [46]. For our purposes, this brief description of the codes and the introduction to the transport is sufficient. From this presentation of JINTRAC, it can be seen that it is suitable for plasma simulations, both interpretative and predictive, with a high level of plasma description. With JINTRAC available capabilities it is possible to simulate both present and future experiments in order to compare and understand the peculiarities and the sensitivity of each plasma scenario to the operating conditions (i.e. plasma engineering parameters). This approach will be presented in the next chapters showing the analysis performed in preparation to DTE2 and the analysis of actual D-T data collected during the experimental campaign.

Chapter 4

Simulations of D plasmas

The work that will be discussed in this chapter has been firstly presented in a reduced version in [61] and afterwards published in [62]. Here it is adjusted and extended for the purpose of this dissertation.

After a first deuterium-tritium (D-T) experimental campaign in 1997 (DTE1) the JET tokamak has operated in D-T main ion plasma mixture again in 2021 (DTE2). DTE2 is substantially different from DTE1 because, since DTE1, in subsequent upgrades, JET has had the original C first wall replaced with an ITER-like wall (ILW) made of Be and W, increased its additional heating power and expanded the set of available diagnostics. The focus of DTE2 has been different from DTE1 as the emphasis has been placed on the stationary nature of the performance instead of the record peak fusion power. The DTE2 target performance is 15 MW of fusion power averaged for 5 s [63].

In preparation to DTE2, experiments have been performed on JET to prepare the plasma scenarios in D, which have been used in DTE2 [18, 7, 25]. Two scenarios are being developed: the baseline scenario where the confinement is achieved at high plasma current ($I_p \geq 3.5$ MA) and medium normalized beta ($\beta_N \approx 1.8$), and the hybrid scenario, which relies on a lower plasma current ($I_p \leq 2.5$ MA) and a higher normalized beta ($\beta_N \approx 2-3$) to achieve good confinement.

Normalized beta is an operational parameter indicating how close the plasma is to the onset of macroscopic MHD instabilities [64] and is defined as [65]:

$$\beta_N = \beta \frac{aB_T}{I_p}$$

where where B_T is the toroidal magnetic field in T, a is the minor radius in m, I_p is the plasma current in MA and:

$$\beta = \frac{\langle p \rangle}{B^2/2\mu_0}$$

is the ratio of the plasma pressure to the magnetic pressure.

These plasmas have been the object of an intense activity of modelling in order to extrapolate the performance from D to D-T and quantify the uncertainty affecting the predicted results [66, 67]. This chapter focuses on the baseline scenario, using

Table 4.1. Main plasma parameters for the JET plasmas used as references for the extrapolations presented in the chapter.

Shot number	92376	96482	42464	42982
Main ion species	D	D	D	D-T
Simulated time window [s]	9.6 - 10.7	10 - 10.5	14.4 - 16.4	15 - 17
B_T [T]	2.8	3.35	3.8	3.8
I_p [MA]	3.0	3.5	3.8	3.8
q_{95}	3.2	3.2	3.5	3.5
β_N [%/MA]	1.8	1.9	1.2	1.45
P_{NBI} [MW]	22	29	18	21.6
P_{ICRH} [MW]	4.4	4.3	0.5	2.0
n_{e0} [10^{19} m^{-3}]	7.8	9.4	8.5	7.8
$< n_e >$ [10^{19} m^{-3}]	5.8	6.1	5.6	5.8
T_{e0} [keV]	5.4	6.0	7.5	5.8
$< T_e >$ [keV]	2.8	2.5	4.5	3.3
T_{i0} [keV]	6.9	8.0	7.6	10.3
$< T_i >$ [keV]	3.0	3.8	3.7	4.9
W_{th} [MJ]	7.5	10.0	8.3	7.9
Neutron rate [10^{16} [n/s]	1.65	3.0	1.33	168.8
Z_{eff}	1.9	1.8	2.3	2.8

the transport model QuaLiKiz to predict the D-T performance of typical baseline plasmas under a variety of assumptions.

Some of the best performing baseline plasmas considered for extrapolation are characterized by a normalized beta $\beta_N \approx 2.2$. These plasmas, however, might be not extrapolable at plasma currents higher than 3.8 MA due to the limited additional heating power available on JET. Therefore, the medium β_N (≈ 1.8) baseline plasma is the basis for the D-T extrapolations.

Table 4.1 reports the main plasma parameters averaged over the time interval of interest of the JET pulses that will be shown in this chapter of the dissertation.

4.1 Validation on the reference discharge

The baseline plasma used as reference for the modelling and the extrapolations presented in this work is JET pulse JPN 92376 ($\beta_N \approx 1.8$). This is a pure D, H-mode plasma with B_T=2.8 T, I_p=3 MA and 26 MW of additional heating power, 22 MW from neutral beam injection (NBI), and 4.4 MW from ion cyclotron resonance heating (ICRH) in H minority scheme. In the flat-top phase of the discharge, D pacing pellets are injected for promoting ELMs, for high and medium-Z impurity influx control and for density control. The experimental time traces of the relevant plasma parameters and the details of the diagnostics considered are shown in Fig. 4.1, while the main plasma parameters averaged over the time window of interest (between 9.6 s and 10.7 s) are reported in Table 4.1.

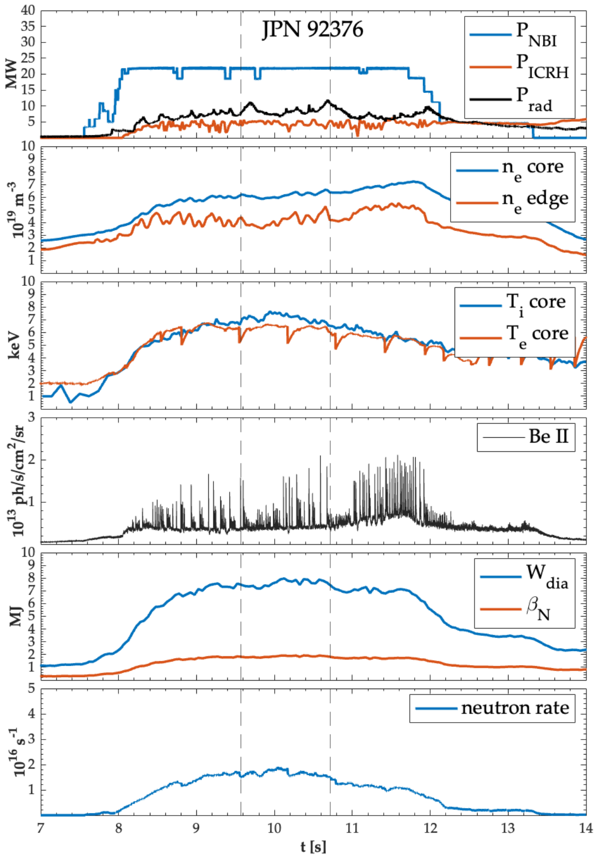

Figure 4.1. Experimental evolution of main plasma parameters for JET shot 92376, a medium β_N ($\beta_N \approx 1.8$) plasma chosen as reference for the extrapolations presented in this chapter. From top to bottom are shown: NBI and ICRH auxiliary heating power and radiated power (from bolometer); core and edge line average electron density (from JET multi-channel infrared interferometer, on-axis electron temperature (from electron cyclotron emission radiometer) and core ion temperature (from high resolution X-ray crystal spectrometer looking at Ni^{+26} emission at $\psi_N \approx 0.18$); Be II emission (from visible spectroscopy, showing the ELM behaviour); plasma thermal energy and β_N and neutron rate.

The modelling of this plasma has been performed with the JINTRAC suite of codes [46] using the QuaLiKiz first-principle transport model [41, 42]. Note that QuaLiKiz takes into account some possible linear isotope effects on the main ion transport, but does not capture other non-linear effects at high β [68, 69]. However, given the moderate β of the plasmas used in this paper as a basis for the extrapolation, these non-linear effects are not crucial and therefore QuaLiKiz can be considered suitable for the extrapolation to D-T main ion plasma mixture.

The simulations are performed in a fully predictive way. In particular, the evolution of plasma current density, ion density, electron and ion temperature and plasma rotation is predicted. In addition, the evolution of the density of a number of impurities was modelled by the impurity transport code SANCO [57]. The impurity transport model includes neo-classical transport from NCLASS [70] and anomalous transport provided by QuaLiKiz.

The initial conditions for the electron density and temperature profiles were taken from the measurements of the JET high resolution Thomson scattering system (HRTS) [71] and for the ion temperature and plasma toroidal rotation profiles from beam charge exchange spectroscopy (CX) [72].

In this simulation an impurity mix of Be ($\langle n_{Be}\rangle/\langle n_e\rangle \approx 1.8\%$), Ni ($\langle n_{Ni}\rangle/\langle n_e\rangle \approx 0.075\%$) and W ($\langle n_W\rangle/\langle n_e\rangle \approx 0.0067\%$) was considered and the relative concentration of the impurity species were prescribed according to an estimate taking into account several diagnostics and described in [73]. In this way, it is ensured that the impurity mixture used in the simulation is the same as in the experiment.

The boundary conditions are imposed at the separatrix identified by $T_e = T_i =$ 100 eV. The heat transport in the edge transport barrier (ETB) is adjusted in order to match the experimental height of the temperature pedestal. The width of the pedestal is imposed to match the experimental value. Once the heat transport in the ETB has been fixed, a χ/D ratio in the pedestal of 4 is assumed and the gas puff and the wall recycling particle source are tuned to match the density at the top of the ETB. Here χ is the heat conductivity (assumed to be the same for ion and electrons in the ETB) and D is the ion particle diffusivity (assumed the same for D and T ions in the ETB), both expressed in m^2/s.

The heat sources are modelled by means of the PENCIL [48] and PION [51] codes for the NBI and ICRH heating source respectively. The synergy between NBI and ICRH is taken into account self-consistently in JINTRAC (see, for example, [53]).

The equilibrium is computed self-consistently with the evolution of the plasma current and of the plasma kinetic profiles by means of the ESCO equilibrium solver [58].

The simulation results for the reference pulse are shown in Fig. 4.2(a), where the electron density and electron and ion temperature profiles are compared to the experimental measurements, and in Fig. 4.2(b), where the modelled D-D neutron rate, Z_{eff} and radiated power are compared to the experimental values.

It can be seen that the general agreement between simulation and experiment is good. In particular there is very good agreement between the experimental and modelled kinetic profiles (electron density, electron and ion temperature) and the measured and modelled radiated power. The experimental neutron rate is initially underestimated by about 30-40% but the predicted value approaches the experimental one from half way through the simulation to the end of the modelled time window.

Moreover, the pedestal pressure calculated in our simulation is 11.2 kPa, close to the experimental one of 10.2 kPa. The differences between measured and modelled pedestal pressure are in agreement within the uncertainties in the experimental pressure computation. This is illustrated in Fig. 4.3 showing the resulting pedestal pressure from a scan of electron and ion thermal diffusivities in the pedestal (including $\chi_e = \chi_i = 0.75$ m^2/s, the value chosen for this simulation), indicating that not only the first-principle transport model captures the details of the reference plasma core, but also that the empirical modelling of the pedestal can be considered realistic.

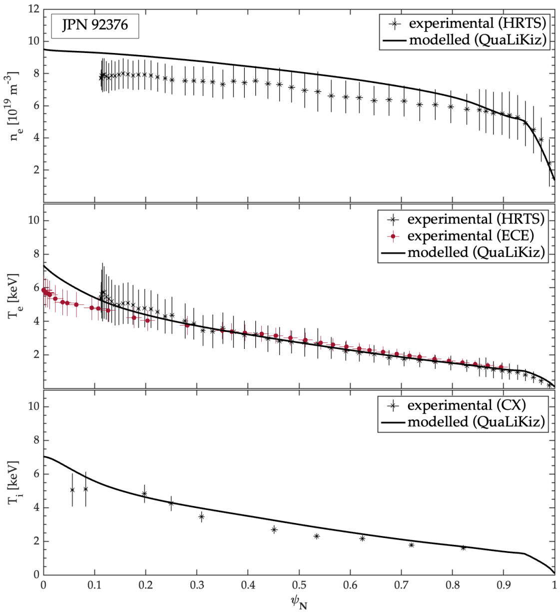

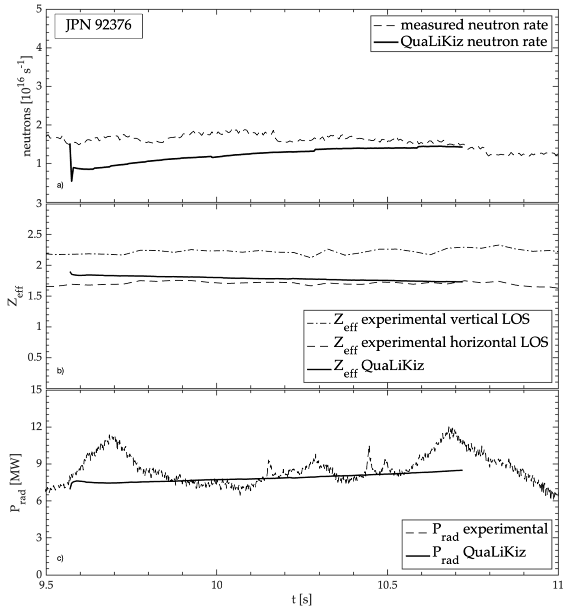

(a) JPN 92376 plasma kinetic profiles

(b) JPN 92376 plasma time traces

Figure 4.2. JPN 92376: (a) Comparison between experimental and modelled n_e, T_e and T_i; The electron density experimental points are HRTS measurements, the electron temperature experimental points are high resolution Thomson scattering measurements (HRTS, black crosses) and electron cyclotron emission measurements (ECE, burgundy circles) and the ion temperature experimental points are beam CX spectroscopy measurements. Measurements and predictions are averaged over the time interval of interest. The vertical error bars combine the RMS over the time interval and the measurements uncertainties, the horizontal error bars are the RMS of the ψ_N coordinate mapped from an EFTP equilibrium. (b) Comparison between experimental and modelled neutron rate, Z_{eff} obtained from Bremsstrahlung measurements along a vertical and horizontal line of sight, and radiated power from bolometry.

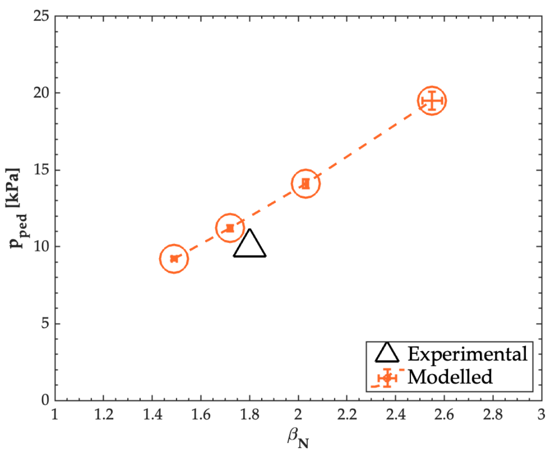

Figure 4.3. JPN 92376: modelled and experimental pedestal pressure for different assumptions of $\chi_{e,i}$ in the pedestal region.

4.2 Extrapolation capability in D plasma at higher plasma current

To further validate the modelling of an ILW baseline plasma, based on the simulations parameter used for reproducing JPN 92376, it has been produced a 'blind' prediction of the JPN 96482, a pure D, 3.5 MA, 3.35 T plasma. The evolution of the main plasma parameters for shot 96482 is shown in figure 4.4 and the values of the most relevant plasma quantities averaged of the the time window targeted by the blind simulation are shown in table 4.1.

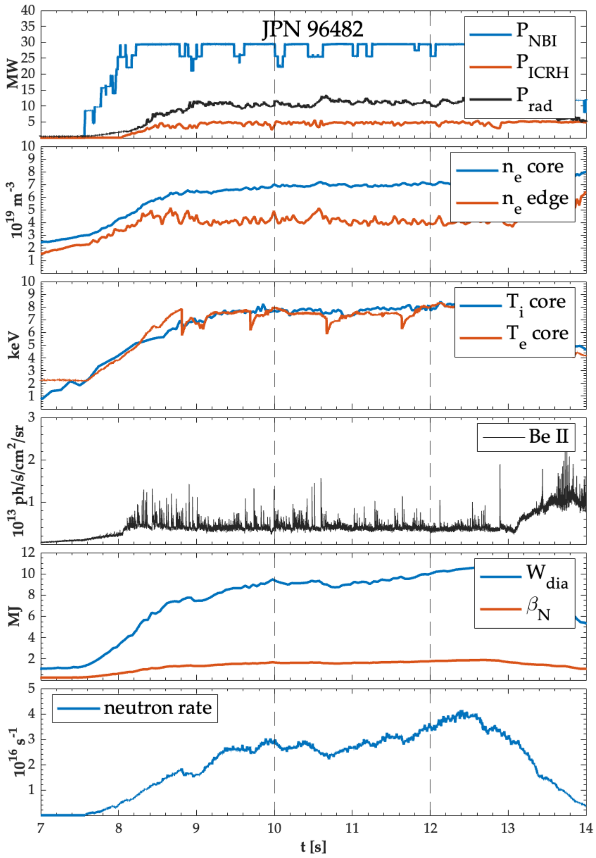

Figure 4.4. Experimental evolution of main plasma parameters for JET shot 96482, a medium β_N ($\beta_N \approx 1.8$) plasma chosen as target to validate the model tuned on JET shot 92376 and used for the extrapolations presented in this paper. From top to bottom are shown: NBI and ICRH auxiliary heating power and radiated power (from bolometer); core and edge line average electron density (from JET multi-channel infrared interferometer, on-axis electron temperature (from electron cyclotron emission radiometer) and core ion temperature (from high resolution X-ray crystal spectrometer looking at Ni^{+26} emission at $\psi_N \approx 0.18$); Be II emission (from visible spectroscopy, showing the ELM behaviour); plasma thermal energy and β_N and neutron rate.

The 'blind' simulation was obtained by repeating the fully predictive simulation of shot 92376 with the plasma current increased to 3.5 MA, the toroidal magnetic field increased to 3.35 T, the initial density scaled at constant Greenwald fraction and imposing the nominal additional heating power of shot 96482. All the remaining simulation parameters (including the transport coefficients in the pedestal and the prescribed impurity mix) were left unchanged. The results are shown in Fig. 4.5(a) and in Fig. 4.5(b), where the pulse is modelled with the same simulation parameters as for JPN 92376 compared with the experimental ones.

As it can be seen this simulation does an excellent job at predicting the higher current discharge, and an even better match with the experiment can be obtained by tuning the ionization source and using the actual experimental impurity mix for the higher current shot determined as described in [73] ($\langle n_{Be}\rangle/\langle n_e\rangle \approx 2.2\%$, $\langle n_{Ni}\rangle/\langle n_e\rangle \approx 0.092\%$ and $\langle n_W\rangle/\langle n_e\rangle \approx 0.0081\%$) .

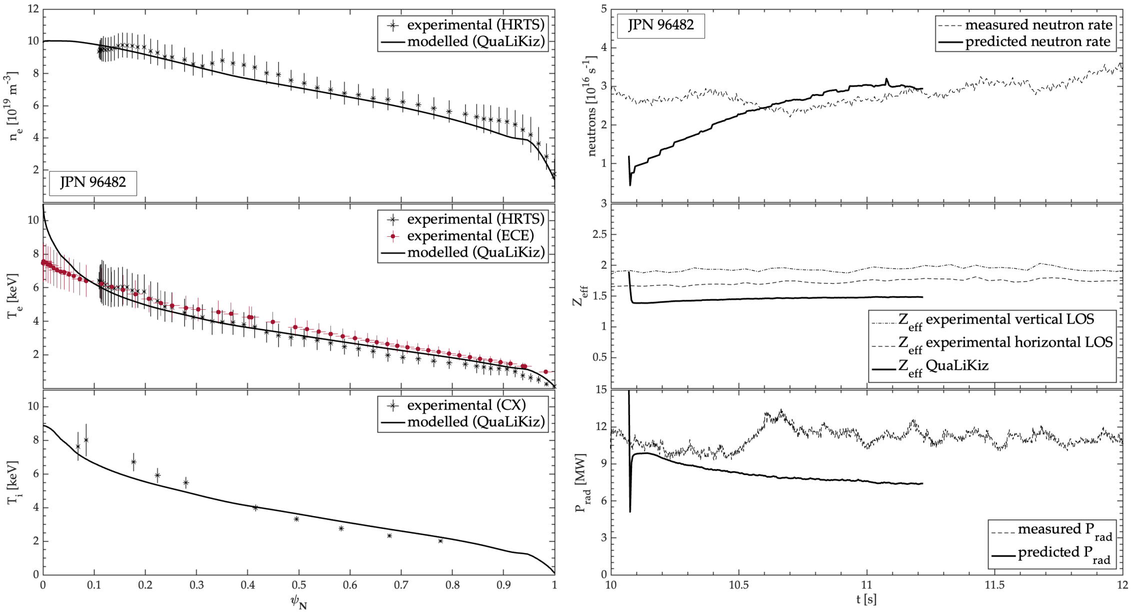

(a) JPN 96482 plasma kinetic profiles **(b)** JPN 96482 plasma time traces

Figure 4.5. JPN 96482: (a) Comparison between experimental and modelled n_e, T_e and T_i; The electron density experimental points are HRTS measurements, the electron temperature experimental points are high resolution Thomson scattering measurements (HRTS, black crosses) and electron cyclotron emission measurements (ECE, burgundy circles) and the ion temperature experimental points are beam CX spectroscopy measurements. Measurements and predictions are averaged over the time interval of interest. The vertical error bars combine the RMS over the time interval and the measurements uncertainties, the horizontal error bars are the RMS of the ψ_N coordinate mapped from an EFTP equilibrium. (b) Comparison between experimental and modelled neutron rate, Z_{eff} obtained from Bremsstrahlung measurements along a vertical and horizontal line of sight, and radiated power from bolometry.

In Fig. 4.4 it can be observed that the performance of the D pulse JPN 96482 consist of two phases, in the first phase ($10 \leq t \leq 12$ s) the performance is lower with respect to the second phase ($12 \leq t \leq 13$ s). It should be mentioned that by scanning the ELM averaged transport coefficients imposed in the pedestal region, in the simulations it is possible to move from the lower performance operative condition of the pedestal to the higher performance operative condition matching with modelling the experiment. This is suggesting that during the experiment, starting from $t = 12$ s, the pedestal changed with a beneficial effect for the core and the overall confinement.

The reproducibility of the JPN 96482 at 3.5 MA starting from the simulation settings optimised to reproduce the JPN 92376 at 3.0 MA confirms the extrapolation capability of JINTRAC-QuaLiKiz-SANCO predictive simulations in D plasmas under a wide range of assumptions on the density scaling and on the impurity mixture. A set of detailed simulations with the experimental boundary conditions of the JPN 96482 will be shown in Sec. 5.2.1, in Sec. 5.2.2 and in Sec. 5.2.3.

4.3 Backward validation on JET DTE1 pulses

To extend the validation of the model to be deployed for the prediction of the performance in DTE2 to a DT plasma, two ELMy H-mode discharges from DTE1 have been simulated. The pulses considered are JET pulses JPN 42464 (D) and JPN 42982 (D-T). Both plasmas have $I_p = 3.8$ MA, $B_T = 3.8$ T, a C plasma facing wall (and, consequently a different impurity mix with respect to the references modelled in the previous section) and use a ^{3}He minority ICRH heating scheme (as opposed to the H minority scheme used in the shots described in the previous section). Shot 42464 is a pure D plasma, whereas shot 42982 is a 50-50 D-T main ion plasma mixture.

Note that, for the D-T plasmas, the collisional heating of the electrons by the alpha particles produced by fusion reactions is calculated in JINTRAC self-consistently with the evolution of the kinetic profile according to the model described in [74]. However, the alpha particle concentration is ignored in the PION calculation of the ICRH absorption. Separate estimates of the role played by the alpha particle as an ICRH absorber indicate that this should be negligible in the scenarios considered in this work.

The evolution of the experimental plasma parameters for these two plasmas is shown in figures 4.6 and 4.7, whereas the average values over the time window of interest are reported in table 4.1. Further details on these shots can be found in [22] and interpretative transport analysis, in the context of a wider study of ELMy H-mode D-T plasmas on JET, can be found in [75].

The same modelling procedure described in the previous section has been applied for the JPN 42464 (D) and for the JPN 42982 (D-T). Note that in these simulations the nominal ^{3}He concentration of $\approx 5\%$ is assumed, C is considered as the only other impurity contributing to Z_{eff} in the plasma and adjusted its concentration to match the experimental Z_{eff} value (inferred from Bremsstrahlung measurements). This resulted in $\langle n_C\rangle/\langle n_e\rangle \approx 3.9\%$ for the JPN 42464 and $\langle n_C\rangle/\langle n_e\rangle \approx 5.6\%$ for the JPN 42982.

These values are broadly in line with the C concentration and Z_{eff} reported in [22] where an impurity mix of 4% C, 1% Be and 6% ^{3}He is given. In the same paper the uncertainty on Z_{eff} is estimated at ± 0.5. Assuming values for Z_{eff} 0.5 lower than the ones used in our simulations it can be found that the C concentration is reduced to 2.6% for the JPN 42464 and to 4.2% for the JPN 42982. However, these lower values of Z_{eff} (and consequently lower C concentrations) would lead to our simulations simultaneously overestimating the experimental neutron rate and underestimating the experimental radiated power.

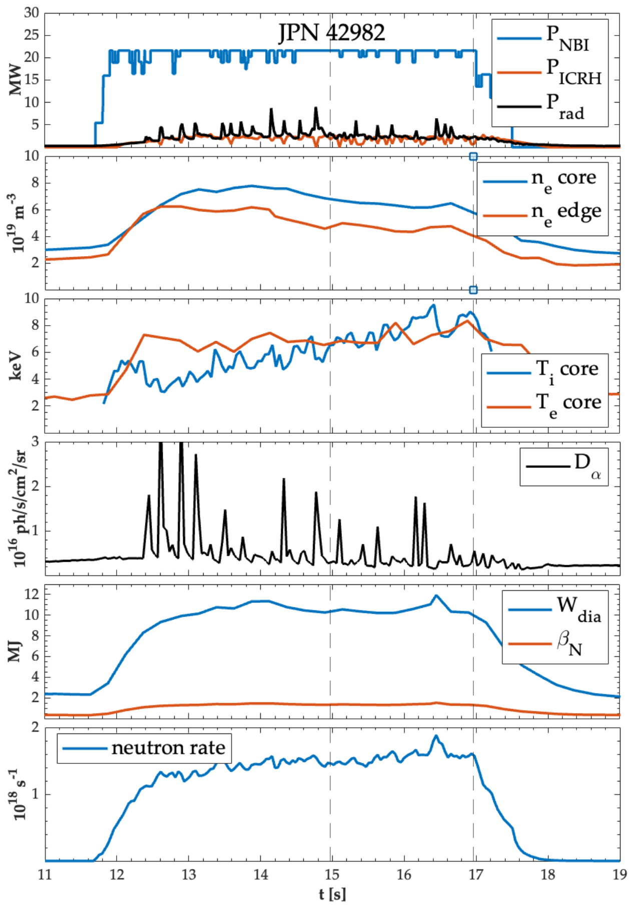

Figure 4.6. JPN 42982: experimental evolution of main plasma parameters for JET shot 42982, a 50-50 D-T plasma from JET campaign DTE1 chosen as target to validate the model tuned on JET shot 92376 and used for the extrapolations presented in this work. From top to bottom are shown: NBI and ICRH auxiliary heating power and radiated power (from bolometer); core and edge line average electron density (from JET multi-channel infrared interferometer, on-axis electron temperature (from LIDAR Thomson scattering) and core ion temperature (from high resolution X-ray crystal spectrometer looking at Ni^{+26} emission at $\psi_N \approx 0.29$); D_α line intensity (from spectroscopy, showing the ELM behavior); plasma thermal energy and β_N and neutron rate.

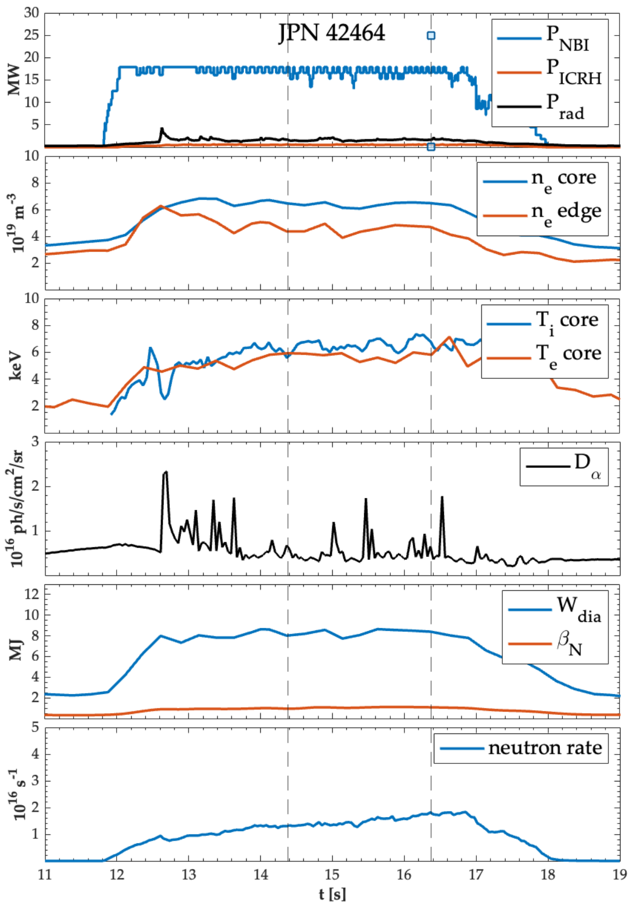

Figure 4.7. JPN 42464: experimental evolution of main plasma parameters for JET shot 42464, a pure D plasma from JET campaign DTE1 chosen as target to validate the model tuned on JET shot 92376 and used for the extrapolations presented in this paper. From top to bottom are shown: NBI and ICRH auxiliary heating power and radiated power (from bolometer); core and edge line average electron density (from JET multi-channel infrared interferometer, on-axis electron temperature (from LIDAR Thomson scattering) and core ion temperature (from high resolution X-ray crystal spectrometer looking at Ni^{+26} emission at $\psi_N \approx 0.23$); D_α line intensity (from spectroscopy, showing the ELM behavior); plasma thermal energy and β_N and neutron rate.

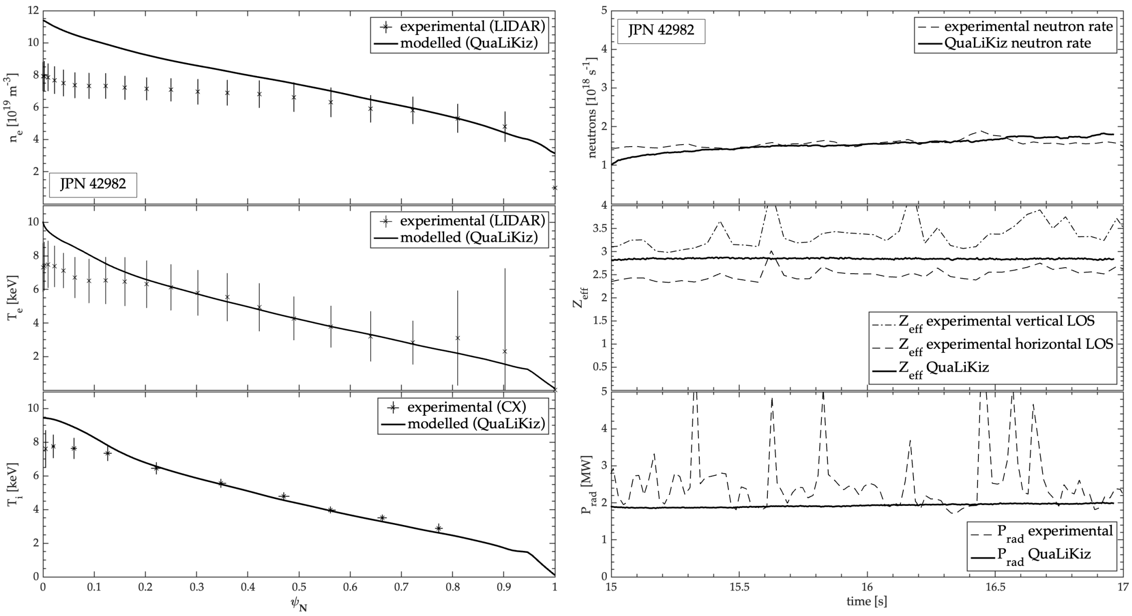

(a) JPN 42982 plasma kinetic profiles **(b)** JPN 42982 plasma time traces

Figure 4.8. JPN 42982: (a) Comparison between experimental and modelled electron density profiles, electron temperature profiles and ion temperature profiles. The electron density and electron temperature experimental points are LIDAR Thomson scattering measurements (LIDAR) and the ion temperature experimental points are beam charge exchange spectroscopy measurements (CX). All measurements are averaged over the modelled time interval. The vertical error bars combine the RMS over the time interval considered and the measurement uncertainty and the horizontal error bars are the RMS of the ψ_N coordinate mapped from a EFIT equilibrium. The modelled profile is the converged solution after full relaxation of the kinetic profiles (QuaLiKiZ, solid lines). (b) Comparison between experimental and modelled neutron rate, Z_{eff} and radiated power. Z_eff is inferred from Brehmsstrahlung measurements along a vertical and a horizontal line of sight across the plasma and radiated power from bolometry.

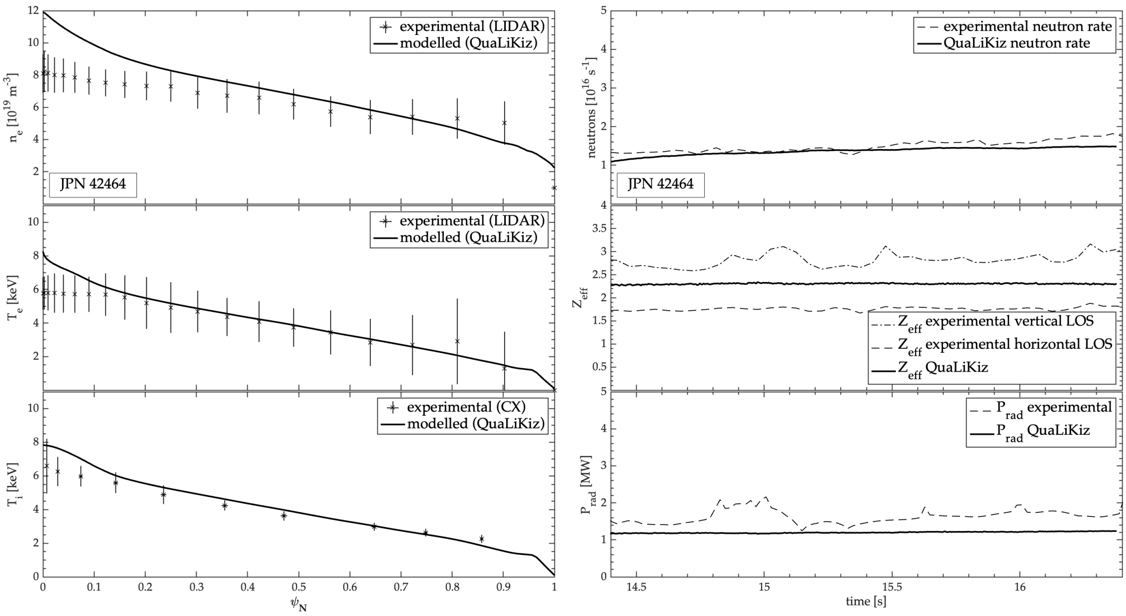

(a) JPN 42464 plasma kinetic profiles

(b) JPN 42464 plasma time traces

Figure 4.9. JPN 42464: (a) Comparison between experimental and modelled electron density profiles, electron temperature profiles and ion temperature profiles. The electron density and electron temperature experimental points are LIDAR Thomson scattering measurements (LIDAR) and the ion temperature experimental points are beam charge exchange spectroscopy measurements (CX). All measurements are averaged over the modelled time interval. The vertical error bars combine the RMS over the time interval considered and the measurement uncertainty and the horizontal error bars are the RMS of the ψ_N coordinate mapped from a EFIT equilibrium. The modelled profile is the converged solution after full relaxation of the kinetic profiles (QuaLiKiz, solid lines). (b) Comparison between experimental and modelled neutron rate, Z_{eff} and radiated power. Z_eff is inferred from Brehmsstrahlung measurements along a vertical and a horizontal line of sight across the plasma and radiated power from bolometry.

The results of the modelling done on the two DTE1 pulses are shown in Fig. 4.8 for the D-T main ion plasma mixture, and in Fig. 4.9 for the D plasma. The agreement between experiment and simulation is generally good, both for the kinetic profiles and in the time traces. However, the lack of measurements in the pedestal region does not allow a proper comparison with the modelling.

The main difference seen in the simulations with C-wall with respect to the simulations shown with the ILW involves the density at the separatrix. It is significantly higher in DTE1 pulses due to the higher values of the Z_{eff}. It has to be noted the tendency of QuaLiKiz to overestimate the peaking of the electron density profiles, which has been also reported and analyzed in [76]. The cause of this discrepancy is not clear. A possible reason could be the fairly strong sensitivity of the main ion density profile peaking predicted by QuaLiKiz to the details of the profiles of quantities such as the T_i/T_e ratio at the top of the edge transport barrier, the safety factor q, the plasma rotation and the impurity density and to the fact that the simulation does not match exactly these plasma parameters.

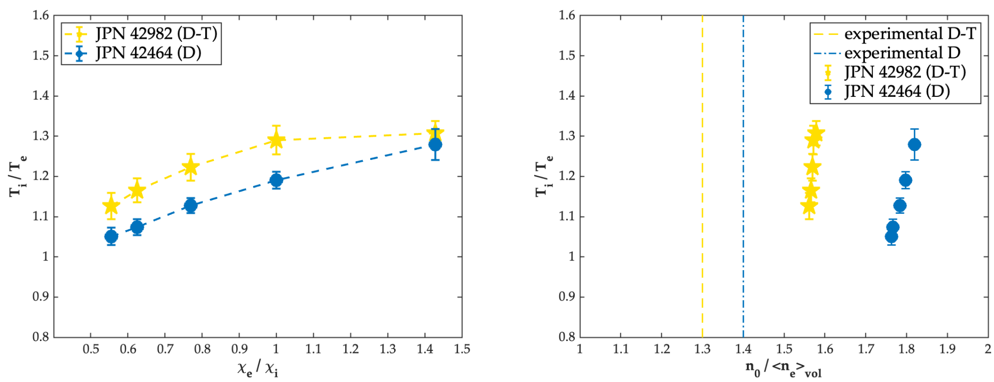

(a) T_i/T_e against the enhancement of χ_e/χ_i **(b)** Density peaking factors

Figure 4.10. Sensitivity study of the density peaking factors in dependence to T_i/T_e.

In Fig. 4.10 the results of the sensitivity study on the density peaking factors are shown in dependence to the T_i/T_e ratio at the top of the edge transport barrier. By scanning the electron thermal conductivity with respect to the ion thermal conductivity imposed in the pedestal, the ratio between ion and electron temperatures can be varied. However, for these pulses the variation in the density peaking factors is modest, and the overestimate of the peaking factor is $\approx 20\%$ in D-T and $\approx 30\%$ in D. Being the D case more affected by density peaking and more sensitive, we do not expect an increasing in the density peaking overestimation extrapolating D cases to D-T cases. A more detailed investigation into the sensitivity of the density peaking to QuaLiKiz input parameters is beyond the scope of this work. The over-prediction of the density peaking significantly affects only a relatively small volume of plasma ($\psi_N \leq 0.2 - 0.3$). Indeed, the simulated and the experimental volume averaged electron densities agree within the measurement uncertainties in both pulses. This agreement seems sufficient for proceeding with the extrapolations to DTE2.

4.4 Extrapolations to DTE2

In order to extrapolate the modelling described in the previous sections to the DT plasmas to be produced in DTE2, the reference simulations of JPN 92376 has been modified, changing the fuel mixture and the NBI injection from pure D to 50-50 D-T main ion plasma mixture. The current and the magnetic field have been increased in three steps to 3.8 MA, 4.2 MA and 4.5 MA, scaling the density in order to keep the Greenwald fraction constant. With the optimistic assumption of 40 MW of additional power (34 MW from NBI and 6 MW from ICRH, see [18]), the magnetic field is 3.5 T at 3.8 MA and it is 3.7 T at 4.2 MA and 4.5 MA. The limit on the magnetic field is imposed by the minimum duration of the flat top necessary to achieve a 5 s window of optimized performance and by the need to limit, at the same time, the thermal and mechanical stresses on the JET toroidal field coils. This means that the extrapolation are not done at constant q_{95}, but q_{95} varies from 3 at 3.8 MA to 2.7 at 4.5 MA.

Extrapolating the pedestal parameters to higher current, the target density at the top of the pedestal is scaled with the current in order to keep the Greenwald fraction constant and the same pedestal width. Particle and heat transport as in the reference case are assumed.

In order to take into account a certain degree of uncertainty linked to the expected pedestal performance, the simulations have been repeated increasing and decreasing the electron and ion thermal conductivity in the ETB by 25%. These cases are determining the lower and upper bound on the predicted performance.

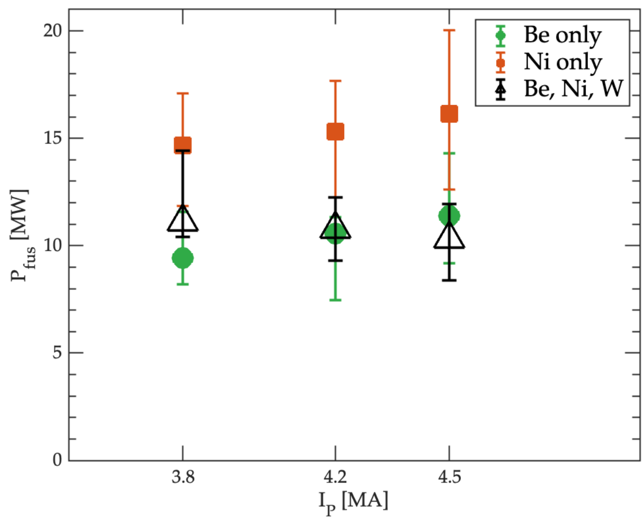

Figure 4.11. Expected fusion power as function of plasma current and for different impurity mixes for a medium $\beta_N \approx 1.8$ baseline plasma based on JPN 92376 assuming 40 MW of additional heating power (34 MW of NBI and 6 MW of ICRH). In this scan $B_T = 3.5$ T at 3.8 MA and $B_T = 3.7$ T at 4.2 and 4.5MA. The error bars correspond to different assumptions on the thermal conductivity in the pedestal.

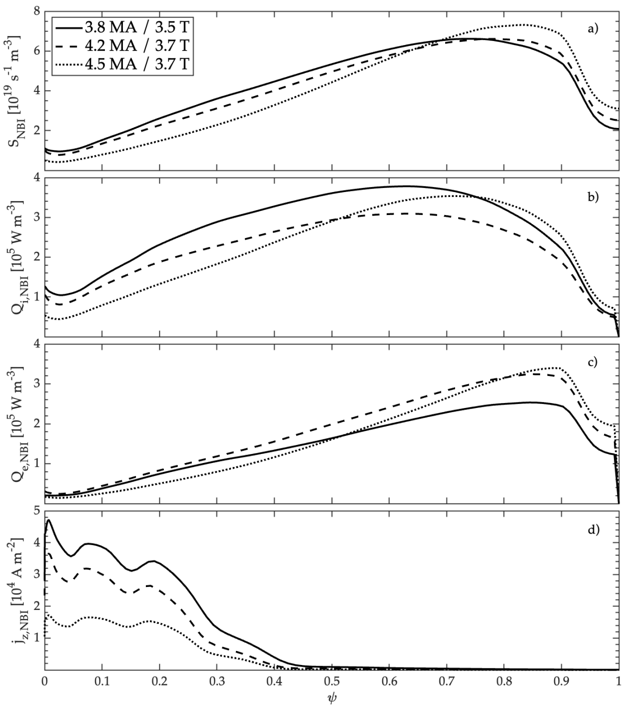

Figure 4.12. NBI deposition profiles for three different plasma currents and fixed Greenwald fraction. From top to bottom: (a) particle source, (b) ion heat deposition, (c) electron heat deposition and (d) driven current. In all cases the total NBI injected power is $P_{NBI} = 34$ MW.

The effect of the impurities is taken into account by assuming the same impurity mix as the one determined experimentally for pulse 92376, with an increased W concentration in order to achieve the same ratio P_{rad}/P_{aux} as in the reference case. Many of the baseline D and D-T pulses exhibit a poloidally asymmetric and localised blob of radiation on the low field side, this effects can not be modelled due to the transport equations are averaged over the flux surfaces. Thus, the modelling can not distinguish the high filed side from the low field side. The effect of the uncertainty in the impurity mix has been assessed by performing two additional series of simulations assuming Ni and Be as dominant impurity respectively and keeping Z_{eff} constant.

The results of this first series of runs are plotted in Fig: 4.11 where the expected fusion power is shown for the different cases. The error bars represent the effect of the uncertainty in the pedestal transport. It can be seen that the fusion power does not increase significantly with plasma current above 3.8 MA and even decreases slightly when W is included in the impurity mix. This is due partly to the fact that the additional power is kept constant rather than increased proportionally to the density, leading to a progressive reduction of the ion temperature in the core, and partly to the fact that, with increased density, the NBI penetration is shallower, resulting in a lower heating source in the plasma core.

The NBI deposition profiles for the three plasma currents considered in this study are shown in Fig. 4.12 where the NBI particle source, ion and electron heat deposition and driven current are ploted.

As for the effect of the impurity mix, it can be seen that the assumption of the contribution to Z_{eff} comes entirely from Be results in a significant plasma dilution, with a maximum fusion power achievable for these moderate β_N baseline plasmas is only 10 MW, as opposed to the 15 MW obtained in the simulations where Ni was assumed to be the only impurity present in the plasma. It should be noticed that in the simulations with only Be the plasma dilution is overestimated and the radiated power is underestimated. In the simulations with Ni only the dilution and the radiated power are both underestimated. The assumption of a more realistic impurity mix of Be, Ni and W based on the empirical estimate of the relative concentration of these species for the reference JPN 92376 does not change significantly the result with respect to the case with Be only. This is because the plasma performance is more sensitive to dilution rather than radiated power.

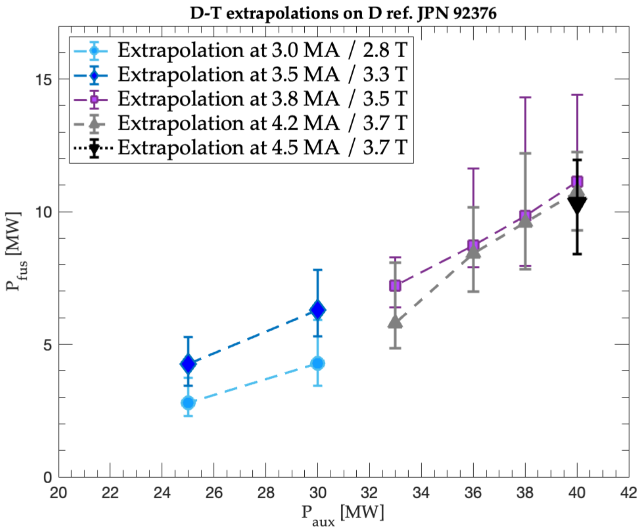

Figure 4.13. Expected fusion power as function of available heating power for different plasma currents for a medium $\beta_N \approx 1.8$ baseline plasma based on JPN 92376 assuming the experimentally determined impurity mix of Be, Ni and W. The error bars correspond to different assumptions on the thermal conductivity in the pedestal..

The effect of the available additional power on the performance is now investigated. In order to do this, starting from the runs at 40 MW with impurity mix including Be, Ni and W, the additional heating power is gradually reduced from 40 MW to 38 MW (32 MW from NBI and 6 MW of ICRH), 36 MW (32 MW form NBI and 4 MW of ICRH) and 33 MW (29 MW of NBI and 4 MW of ICRH) respectively. Each power scan has been performed for 3.8 MA, 4.2 MA and 4.5 MA.

Moreover, to assess the impact of the availability of additional heating power of lower or similar magnitude with respect to the reference case, a second series of runs for plasma current equal to 3.0 MA and 3.5 MA has been performed assuming 25 MW (23 MW of NBI and 2 MW of ICRH) and 30 MW (27 MW of NBI and 3 MW of ICRH). The results are shown in figure 4.13 where the different scans for different plasma currents are plotted. The 10 MW of fusion power can be achieved only with an available additional heating power above 36 MW.

4.5 Chapter summary

The simulations presented in this chapter predict the fusion power in baseline scenario at medium β_N (≈ 1.8) in DTE2. The interest in these plasmas is due the fact that they are more easily extrapolable to higher field and current and more representative of a typical baseline scenario than the higher β_N and peaked performance plasmas considered in the past.

The transport model used in the extrapolation is the QuaLiKiz model, which reproduces well pure D plasmas produced in JET with an ILW, and which is in reasonable agreement with plasmas from DTE1 (JET with C-wall) apart for the over-prediction of the peaking of the density profile.

The results indicate that it should be possible to achieve 10 MW of fusion power over 5 s in a fairly wide range of circumstances, provided that 38 MW heating power is available.

Moreover, they suggest that pushing for high current is not necessarily a way to continuously improve the fusion performance as the increase in density at fixed additional heating power is likely to offset the expected increase in confinement associated with higher current.

The effect of the uncertainties in the pedestal confinement have also being investigated and can be responsible for a variation of about 1 MW of fusion power in excess or defect of the reference case where the pedestal transport was tuned to match the experimental parameters in the reference case at 3.0 MA. The analysis of the sensitivity to pedestal condition has been motivated by the necessity of taking into account on one side a possible improved pedestal confinement in DT with respect to D and on the other hand by the possibility that the fuelling rate in D-T will have to be increased with respect to pure D plasmas to promote the ELMs, which could be less frequent in D-T, and are necessary to flush impurities out of the plasma edge.

A final analysis has been conducted to investigate the sensitivity to the available additional input power. In order to estimate the effect of different levels of heating power we have run simulations at different current levels scanning the additional heating power availability from 25 MW (23 MW of NBI and 2 MW of ICRH) to 40 MW (34 MW of NBI and 6 MW of ICRH). The assumption for the impurity mix was the most realistic one including Be, Ni and W and based on the concentrations experimentally determined for JPN 92376.

This scan has shown that the heating power is probably the most critical parameter in determining the highest fusion power achievable and that an additional heating power above 36 MW will be needed to achieve $P_{fus} = 10$ MW.

For these medium β_N plasmas, 15 MW of fusion power are achieved only in the best case scenario where the dilution due to Be is minimised and the pedestal confinement is optimized, in presence of 40 MW of available additional heating power.

In all the cases analyzed the contribution to the total neutron yield was $\approx 60\%$ from thermal reactions and $\approx 40\%$ from beam-target reactions (beam-beam reactions being negligible).

Chapter 5

Transport analysis of D-T pulses

5.1 Experimental results of D-T baseline scenario

After the end of the deuterium-tritium experimental campaign, the fusion power predictions discussed in the previous chapter and presented in [62] have been compared with the experimental fusion power. In Figure 5.1 the comparison between

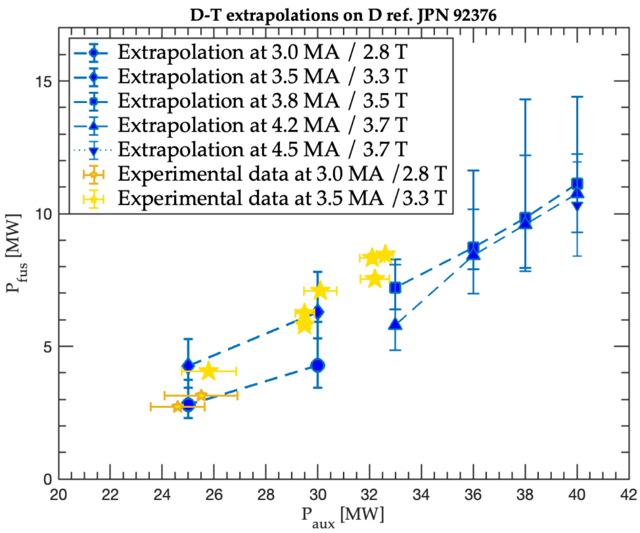

Figure 5.1. Experimental fusion power obtained by *baseline* scenario during DTE2 campaign averaged over 0.5 s during the flat-top phase of the discharges (yellow stars) compared to the predicted fusion power in dependence of the available auxiliary heating power at different plasma currents (blue markers).

the predicted fusion power and the experimental results is shown. It can be seen that the stars, identifying the experimental data, are close to the predictions within the uncertainties related to the pedestal modelling presented in 4.4. Moreover, at high available auxiliary heating power, the experimental fusion power seems laying on the upper bound of the predicted performance.

A similar figure to Fig. 5.1 can be produced with the experimental fusion power obtained by the *hybrid* scenario compared to the results of the predictive modelling presented in [66], showing a good agreement between predictions and experimental results. The fact that, over a wide range of plasma parameters, both in *hybrid* and *baseline* scenario, the predictive simulations are in agreement with the actual D-T data, denotes a good prediction capability of QuaLiKiz and TGLF in D-T main ion plasma mixture. The main differences between D-T experiments and predictive simulations done in preparation to DTE2 are related to the experimental boundary conditions, i.e. the total auxiliary power P_{aux}, its components from NBI and ICRH and, therefore the toroidal velocity V_{tor}, the impurity mix composition and, consequently, Z_{eff} and P_{rad}, and the main ion plasma composition. We chose to perform predictive simulations imposing the experimental boundary conditions to the discharges JPN 96482 in D plasma mixture and the discharge JPN 99948 in D-T plasma mixture. The discharge JPN 99797 will be also modelled for studying the D-T fuel mix control on actual D-T data. The relevant plasma parameters of these pulses are summarised in the Table 5.1.

Table 5.1. Main plasma parameters of the JET plasmas analysed after DTE2 campaign averaged in the reference time intervals.

JPN	96482	99948	99797
Main ion species	D	D-T	D-T
T concentration [%]	-	50	53
Simulated time window [s]	10 - 10.5	9.5 - 10	9.5 - 10.7
B_T [T]	3.35	3.35	3.35
I_p [MA]	3.5	3.5	3.5
q_{95}	3.2	3.3	3.3
β_N [% / MA]	1.8	1.9	1.8
P_{NBI} [MW]	29.0	28.6	25.8
P_{ICRH} [MW]	4.3	3.5	3.7
$n_e(0)$ [10^{19} m^{-3}]	8.9	8.5	9.2
$< n_e >$ [10^{19} m^{-3}]	6.1	7.1	6.7
$T_e(0)$ [keV]	6.0	8.0	7.5
$< T_e >$ [keV]	2.5	2.5	2.4
$T_i(0)$ [keV]	8.0	8.5	7.5
$< T_i >$ [keV]	3.0	3.3	3.0
W_{th} [MJ]	10.0	11.7	10.6
Neutron rate [10^{16} n/s]	2.75	296	214
Z_{eff}	1.7	1.4	1.6

The time intervals of analysis have been chosen in order to compare the JPN 96482 with the JPN 99948 before it stars accumulating impurities.

The evolution of these two discharges can be compared in Fig. 5.2. It can be seen that the initial entry in H-mode is very similar, the two discharges share comparable auxiliary heating power, and the radiative power in the density ramp-up are close to each other. In this phase, the electron and ion temperatures are similar while the plasma stored energy of the D-T pulse results higher with respect to the stored energy of the D pulse despite the fluctuations of the NBI power. After $t \approx 9s$, the core electron density of the D pulse stabilises, while in the D-T pulse it is still

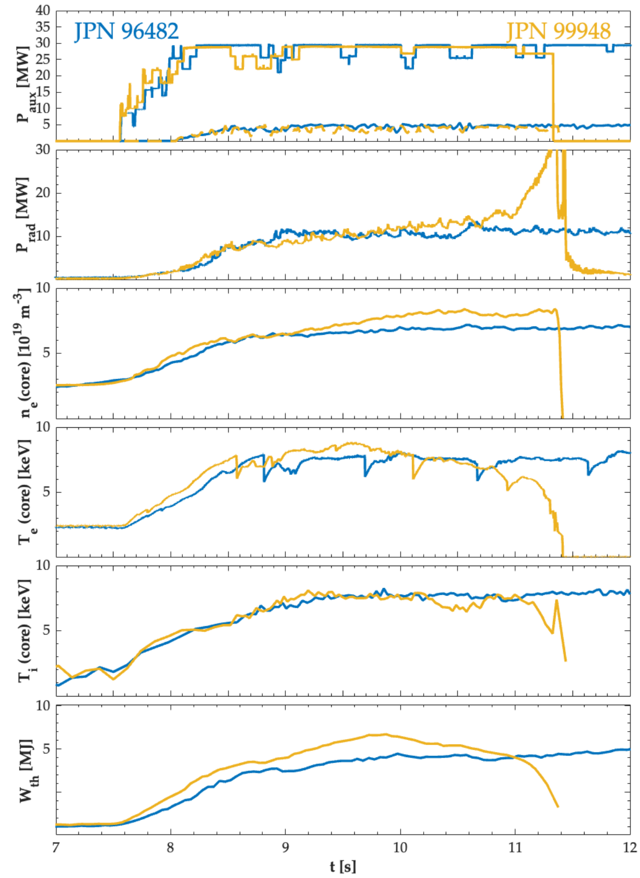

Figure 5.2. Experimental evolution of main plasma parameters for JPN 96482 (D) [blue] and the time traces of the JPN 99948 (D-T) [yellow]. From top to bottom: auxiliary heating power from NBI P_{NBI} and from ICRH P_{ICRH}; radiated power P_{rad} (from bolometer); core line averaged electron density n_e (from JET multi-channel infrared interferometer); on-axis electron temperature T_e (from electron cyclotron emission radiometer); core ion temperature T_i (from high resolution x-ray crystal spectrometer looking at Ni^{+26}); plasma thermal energy W_{th}.

increasing. In this time interval in the D-T pulse, despite the increase in the radiative power the ion and electron temperatures and the plasma stored energy seems to be not suffering from the increase in density. The impurity accumulation starts at $t \approx 10s$ in the a region of the plasma situated on the low field side, the ELM impurity flushing become less effective, and the pulse disrupts due to radiative collapse [77]. This continuous increase of density has been observed in all the *baseline* pulses performed during the DTE2 campaign and is responsible for the impossibility of achieving a *baseline* 5 s long pulse. The density increase is followed by a weakening of the ELM activity and an eventual exponential increase of the radiated power leading to the collapse of the discharge. The reasons for this behavior and possible solutions are still under investigation by JET experimental team. The interpretation of this chain of events is not straightforward. For the moment, the main working hypothesis is that the particle confinement is different between the three plasmas and improves with the isotope mass [78]. A possible explanation could be related to the limitations on available heating power. Operating at high current, which is characterizing the *baseline* scenario, involves operating at high density. Since L-H transition power P_{L-H} increases with the increasing of density it is possible that the *baseline* scenario has operated marginally above the L-H power threshold [77]. This is the root cause of the density increase, which in turn increases the L-H transition threshold implying that the DT and T plasma are more marginally into H-mode than the D ones. Consequently, the ELM activity cannot be sustained and becomes progressively weaker until the ELMs cannot flush the main gas and the W from the plasma anymore, giving way to an increase in impurity concentration and radiated power and, eventually, to the collapse of discharge. The fact that we were operating at relatively high current, field and density and the available heating power was limited and often intermittent exacerbated the problem and prevented us to achieve a 5 s high performance window in DT. The interpretation given above is somehow in contradiction with the expectation that the L-H transition power threshold should be lower in DT and T than in D. In the baseline case it would appear that the isotope dependence of the L-H threshold is dominated by the density dependence. An alternative interpretation could be that, despite the fact that the plasmas are more above threshold in DT and T than in D, the ELM activity is more difficult to sustain for higher isotope mass [79].

An evolution of the density during the flat top phase is present also in the other scenarios performed in DTE2, the *hybrid* and the *optimised fuel mix scenario*. However, they did not suffer that much disruptions in D-T, as they usually do not in D, with respect to the *baseline* scenario due to their lower plasma current (i.e. lower plasma density).

The plasma kinetic profiles can be compared in Fig. 5.3. The plotted profiles have been obtained from interpretative TRANSP analysis fitting the experimental measurements with methodologies described in [80]. This interpretative analysis are intended to check the consistency of different measurements and reproduce the evolution of the plasma performance by evolving the fitted kinetic profiles. Another outcome of TRANSP interpretative analysis is producing plasma kinetic profiles to be used in further analysis (such as, for example, impurity analysis).

The first significant difference between the D pulse and the D-T pulse is related to the pedestal values: the electron density is higher in the D-T pulse with respect to the D pulse, and the pedestal seems to be also wider. This difference in 3.5 MA *baseline* pulses seems to be systematic in all the pulses performed in D-T main ion plasma mixture. No significant differences can be observed in the electron temperature profile while the main differences in the ion temperature and in the toroidal velocity profiles are in the region $\rho_{tor} \leq 0.6$. It has to be mentioned that the on-axis values are obtained from an extrapolation of the fit, since experimental data are not reliable in the region inside $\rho_{tor} \leq 0.2$.

After this brief and phenomenological introduction to the pulses that are modelled in this work, in the following section will be presented the results of the predictive modelling performed with QuaLiKiz and TGLF. The modelling results will be presented comparing the two first principle transport models with similar simulation settings on each pulse. The aim of this work is identifying the limits and the assumptions required to reproduce both the D pulse and the D-T pulse sharing the same assumptions in the modelling. The simulations will be presented increasing the complexity of the modelling in order to evaluate the sensitivity of the simulations results to the different boundary conditions, varied with the goal of improving the agreement of the predictive simulations with the experimental data.

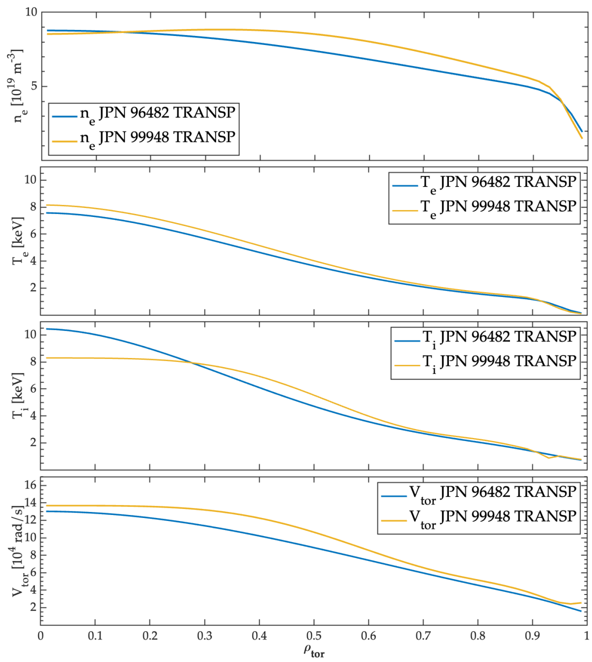

Figure 5.3. Comparison between TRANSP interpretative profiles averaged in the reference time interval plotted in the normalised toroidal radius ρ_{tor} for JPN 96482 and JPN 99948. Electron density profile n_e; electron temperature profile T_e; ion temperature profile T_i ; toroidal velocity profile V_{tor}.

The last section of this chapter will be dedicated to the modelling of the JPN 99797 in D-T main ion plasma mixture. The pulse shows a flat-top phase longer than 1.5 s, which seems to us suitable for balancing the different particle sources. Indeed, in the flat-top phase the *baseline* D-T scenario has a fuelling recipe involving pure T gas puffing and D pacing pellets in presence of balanced D-T beams. The use of different fueling channels for the different hydrogen isotopes gives the possibility to obtain an estimate of the wall particle sources by balancing the particle sources in order to agree with the experimental main ion plasma composition.

5.2 Modelling the reference discharges

5.2.1 Modelling with internal boundary conditions

The modelling presented in this section has been agreed with the JET Task dedicated to the D-T scenario extrapolations. The main deliverable of this Task is to provide a methodology that can be used at ITER to calculate the expected D-T fusion power based on the achieved D pulses. Among the deliverables of the Task, there is the benchmarking of different transport codes, such as JINTRAC, TRANSP and ETS, using QuaLiKiz and TGLF transport models with the same simulation settings and boundary conditions. Here we present the results of JINTRAC-QuaLiKiz and JINTRAC-TGLF (with saturation rule 2, i.e. SAT2) predictive simulations, while an extended comparison between the results obtained with the different transport code can be found in [81]. Therefore, the predictive simulations are different from those presented in the previous chapter.

The simulations are performed with the same settings in D and D-T main ion plasma composition. The boundary conditions of the simulations for the profiles of n_e, T_e and T_i are obtained with TRANSP interpretative analysis and are imposed at $\rho_{tor} = 0.85$. The toroidal velocity is not predicted but imposed in the simulations from the TRANSP interpretative analysis. Impurity transport is not computed, the Z_{eff} profile is imposed in agreement with the estimate of spectroscopy, and the impurity mix composition is modelled as a single effective impurity species. Since the impurity transport is not evolved and the impurities treated as a single effective impurity, the radiation profile must be imposed from experimental measurements. The equilibrium, computed by ESCO, is evolved self-consistently with the evolution of plasma kinetic profiles, and the power and particle deposition from NBI and ICRH are computed with PENCIL-PION modules. In the D-T pulse, alpha heating is computed with the Mako model. The neoclassical transport is computed with NCLASS, with a low component (few percent) of additional Bohm transport for increasing the numerical stability of the simulations and avoid the presence of regions where the transport is completely suppressed.

In Fig. 5.4 are shown the results of the QuaLiKiz and TGLF runs done with internal boundary conditions assuming the Z_{eff} profile found reproducing the D pulse analysed in section 4.2 with JINTRAC-QuaLiKiz-SANCO simulations. Both the simulations are in agreement with the experimental results within the experimental uncertainties. Some differences emerge in the profiles, the shape of the n_e in QuaLiKiz simulation is enhanced by the higher density over-prediction in the core region, QuaLiKiz T_e profile agrees with the TRANSP interpretative run except in the inner core region while the T_i is underestimated. In the TGLF runs, n_e profile agrees with the TRANSP interpretative profile, T_e is significantly over-predicted and T_i shows a good agreement with the TRANSP data. Indeed, the TGLF simulation predicts very well the neutrons produced in the time interval of interest.

Using the same simulation settings and adjusting the experimental boundary conditions we have modelled the D-T pulse. Being unavailable the spectroscopy estimates produced by [73], we determined the impurity mix composition following the methodology presented in [82]. A predictive JINTRAC-QuaLiKiz simulation has been set-up with the boundary condition at the separatrix, and the pedestal is

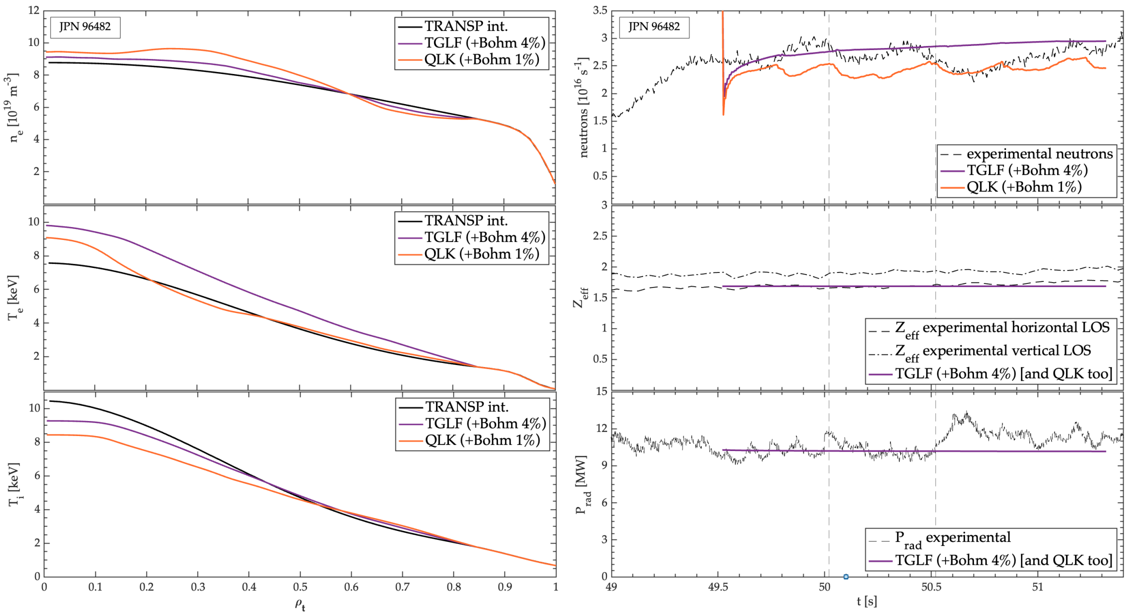

(a) JPN 96482 plasma kinetic profiles

(b) JPN 96482 plasma time traces

Figure 5.4. JPN 96482 plasma profiles (averaged in the reference time interval) and time traces predicted with QuaLiKiz and TGLF, with internal boundary conditions, compared to TRANSP interpretative profiles and experimental time traces.

modelled to reproduce the same values obtained in TRANSP interpretative analysis. The nickel content is determined tuning the concentration required to match the Ni radiative power estimated by spectroscopy [83]. The tungsten content is obtained by reproducing the experimental plasma bulk radiative power. The beryllium is assumed to be the dominant impurity and its content is obtained matching the experimental measurements of the effective charge Z_{eff}. The Z_{eff} profile found in this simulation has been imposed both to QuaLiKiz and TGLF runs, while the impurity mixture composition has been used to determine the effective impurity.

The results of the simulations are shown in Fig. 5.5. Both the models converge on a performance that agrees with the experiment, but outside the reference time interval. In order to match the experimental performance, the additional Bohm transport component in the TGLF simulation has been reduced from the 4% to the 2.5%, obtaining a good agreement shown by the cyan case in Fig. 5.5 (b). A similar approach has been attempted also with the QuaLiKiz simulations, reducing the addition Bohm transport component up to the 0.1%, without any beneficial effect on the predicted performance. This sensitivity of the simulation results to the additional Bohm component is somehow unexpected and has not been observed in simulations where the boundary conditions are prescribed at the separatrix, and the ETB is modelled. The transport coefficients predicted by the Bohm transport model could increase significantly while approaching the plasma edge region, and this increase has a strong impact when imposing internal boundary conditions inside the plasma, while it has no impact when modelling the ETB with an ELM average

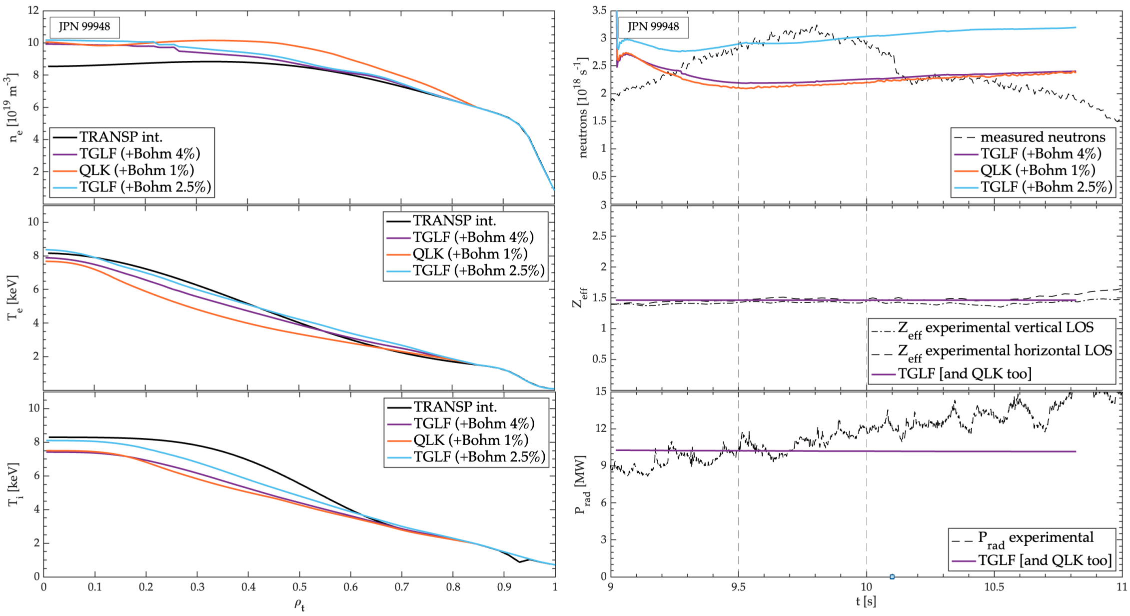

(a) JPN 99948 plasma kinetic profiles

(b) JPN 99948 plasma time traces

Figure 5.5. JPN 99948 plasma profiles (averaged in the reference time interval) and time traces predicted with QuaLiKiz and TGLF, with internal boundary conditions, compared to TRANSP interpretative profiles and experimental time traces.

particle diffusivity and an ELM average heat conductivity.

In Fig. 5.6 the transport coefficients can be compared between the two pulses. Comparing the TGLF results in the D-T case, one could see the difference introduced by the reduction of the additional Bohm transport component. The QuaLiKiz transport is significantly reduced with respect to the TGLF transport both in the density and ion temperature channels. Despite that, the reduction of density transport produces the mentioned density over-prediction which is responsible for the lower electron and ion temperatures. Moreover, with an increased density profile, the NBI beam power deposition results more peripheral. This is contributing to the reduction of the neutron yield both in the thermal and in the beam-thermal component.

Because of the impossibility of reproducing the D-T pulse in the reference time interval with QuaLiKiz transport model, we increased the modelling complexity using the methodology presented in section 4.1, by setting the boundary conditions at the separatrix and modelling the pedestal. However, the modelling procedure illustrated in the present section could be used to obtain a lower limit of the D-T expected fusion power calculated, on the D pulses chosen as reference for the extrapolations.

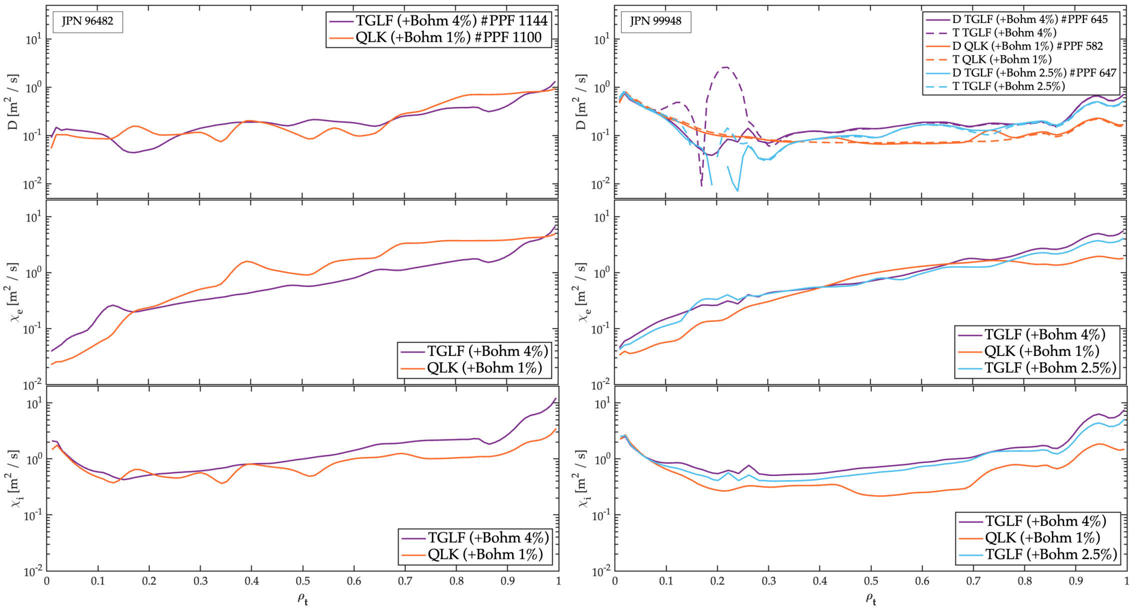

(a) JPN 96482 transport coefficients

(b) JPN 99948 transport coefficients

Figure 5.6. A comparison between the D and D-T transport coefficients (averaged in the reference time interval) computed by QuaLiKiz and TGLF, with internal boundary conditions.

5.2.2 Modelling the pedestal with boundary conditions set at the separatrix

The results of JINTRAC-QuaLiKiz-SANCO predictive simulations are presented in this section. The modelling follows the settings presented in section 4.1, i.e. predicting n_e, T_e, T_i, n_D, n_T, the current density j_z and impurity transport, but the toroidal velocity is imposed from TRANSP interpretative analysis as done in section 5.2.1. The impurity mixture composition has been determined for both the pulses with the method described in [82]. The additional Bohm transport component is equal to 10%. As it has been mentioned before the simulation parameters are optimised on the D pulse and then used in the D-T predictive modelling. The pedestal is modelled by mean of imposing an ELM averaged thermal conductivity $\chi_{eff} = \chi_i = \chi_e$ and an ELM averaged particle diffusivity D. In order to reproduce the D pulse, we assumed $\chi/D = 4$ in the pedestal region, scanned the effective thermal diffusivity to match the experimental electron temperature at the top of the edge transport barrier, tuned the external particle sources with a feedback loop on the measured electron density at the top of the barrier. The effective thermal conductivity found reproducing the D pulse JPN 96482 is $\chi_{eff} = 0.5$ m^2/s. This is imposed to the D-T pulse JPN 99948 with the only difference being the tuning of particle sources required to match the experimental evolution of the main ion plasma composition and the higher density at the top of the pedestal.

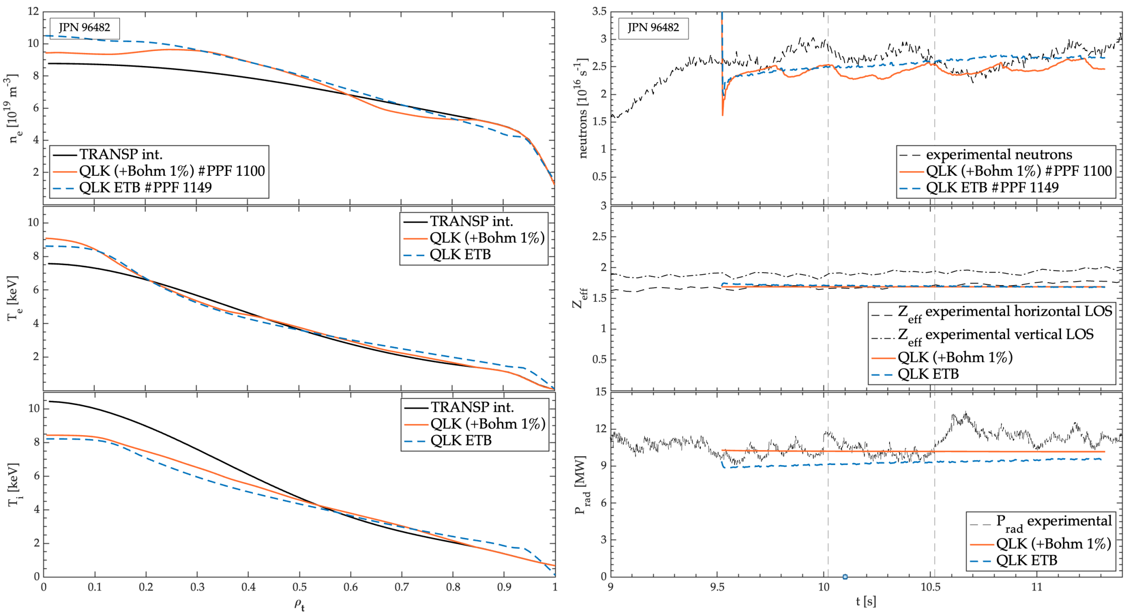

(a) JPN 96482 plasma kinetic profiles **(b)** JPN 96482 plasma time traces

Figure 5.7. JPN 96482 plasma profiles (averaged in the reference time interval) and time traces predicted with QuaLiKiz with and without internal boundary conditions, compared to TRANSP interpretative profiles and experimental time traces.

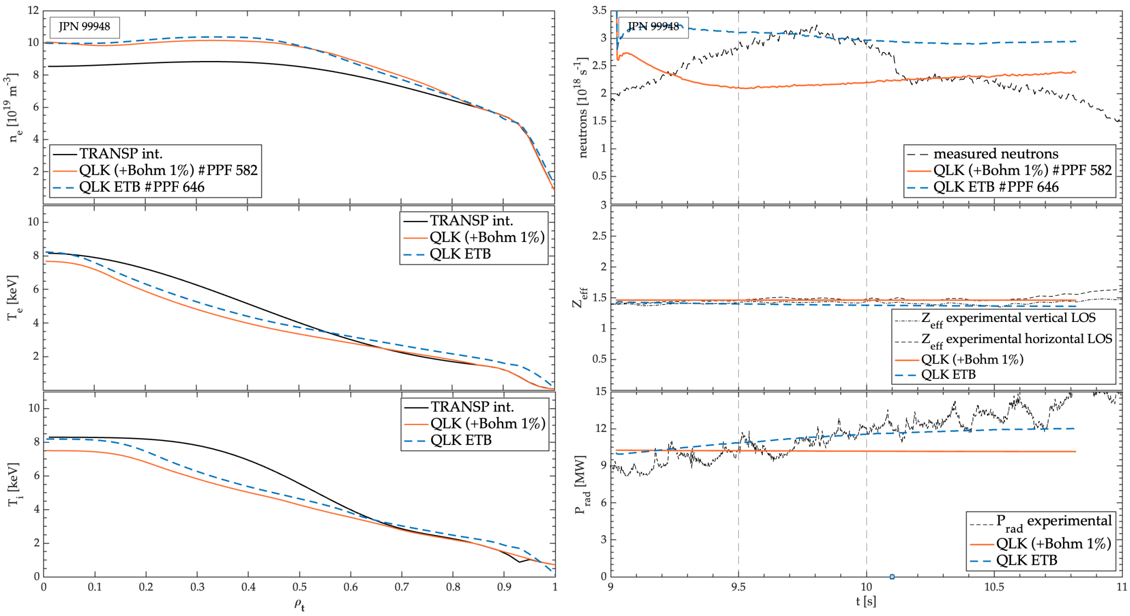

(a) JPN 99948 plasma kinetic profiles

(b) JPN 99948 plasma time traces

Figure 5.8. JPN 99948 plasma profiles (averaged in the reference time interval) and time traces predicted with QuaLiKiz with and without internal boundary conditions, compared to TRANSP interpretative profiles and experimental time traces.

In Fig. 5.7 the results of the predictive simulation done on the D pulse with the boundary conditions at the separatrix can be compared with the results presented in the previous section. In Fig. 5.8 the corresponding predictive simulation in D-T main ion plasma composition is shown. As it can be seen, both the simulations predict well the plasma performance in the reference time interval. Starting from the D-T pulse, without any significant difference in the n_e profile introduced by the pedestal modelling, the on-axis T_e and T_i are recovered. The predicted neutron yield agrees with the measurement and is stable for the whole simulated time interval. The reason of the differences between the predicted performance at the end of the simulations is in the presence of a large sawtooth (not modelled) at $t_{SW} = 10.11s$, which is responsible for the drastic decrease of neutron yield in the experiment. The impurity mix composition, together with the impurity transport computed by SANCO, describes well the evolution of the experiment, matching not only the average P_{rad} but also its increase during the simulated time interval.

In the D pulse, the modelling of the edge transport barrier produces more differences in the electron density profile, with respect to the D-T case (cf. Fig. 5.7(a)). The n_e over-prediction comes along the density peaking over-prediction, and is not present in D-T simulation. As it has been shown in section 4.3, when investigating the QuaLiKiz density peaking, pure D pulses seem to be more sensitive in the simulations to density peaking with respect to D-T pulses. In this case, a possible contributor to the over-prediction of the core density in D could be the NBI particle deposition. In Fig. 5.9 NBI particle deposition profile of pure D beams can be compared to the particle deposition profile in presence of balanced D-T beams. It is well known that NBI particle deposition is the dominant fueling source inside the core where $\rho_{tor} \leq 0.5$, this is a result obtained in the experiments [84] an in modelling [82]. Pure D beams, characterized by a higher energy with respect to D-T beams, are penetrating better towards the plasma core and are contributing to the core fueling with a higher particle source. Another player on the density peaking is the impurity transport that will be investigated in the next section.

In conclusion to the modelling done with boundary conditions at the separatrix, it has been shown that, with a proper modelling of the pedestal, it is possible to reproduce both D and D-T pulses using the same simulation settings and the same pedestal modelling. The only differences between the D and D-T cases are related to the experimental boundary conditions, showing a good prediction capability of the reduced transport models when applied to realistic plasma operating parameters. For completeness, in Fig. 5.10 the computed transport coefficients for the D and D-T pulses can be compared in the cases where boundary conditions are imposed inside the plasma together with the cases where the pedestal is modelled and the boundary conditions are at the separatrix. It can be seen that the transport coefficients in the pedestal region are significantly lower. With similar density profiles and similar gradients, the reduction in the particle diffusivity produces a reduction of the particle fluxes towards the separatrix with the consequent increase in particle confinement time.

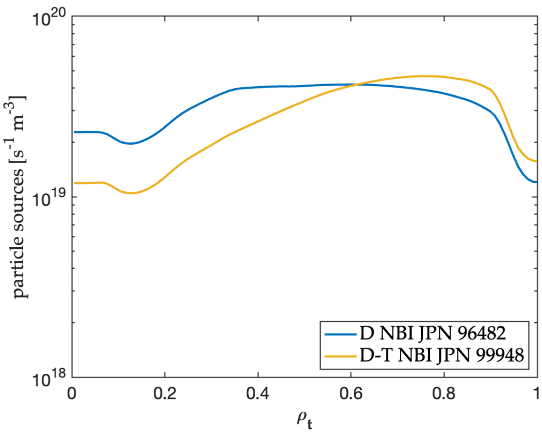

Figure 5.9. Comparison between NBI particle deposition profiles averaged in the reference time interval plotted in the normalised toroidal radius ρ_{tor} for JPN 96482 in presence of pure D beams and JPN 99948 in presence of balanced D-T beams.

The approach presented in this section should be preferred when preparing predictive simulations. Indeed, in the section where internal boundary conditions are imposed the energy and particle balance is solved in presence of arbitrary sources (or sinks) in order to match the boundary conditions. Time evolving internal boundary conditions have been also considered but its usage frequently produces numerical instabilities and leads to run crashes. On the contrary, modelling the pedestal with an effective thermal conductivity and an effective particle diffusivity allows to obtain an estimate of the particle sources required to sustain the pedestal taking into account the transport contribution from the core. This is more realistic and describes well the mutual interactions between core and pedestal region. It can be argued that the pedestal determines the operational conditions for the core, but also the core transport can influence the pedestal operating point. The pedestal and edge plasma physics are still open arguments and a theoretical approach to the problem is still under investigation.

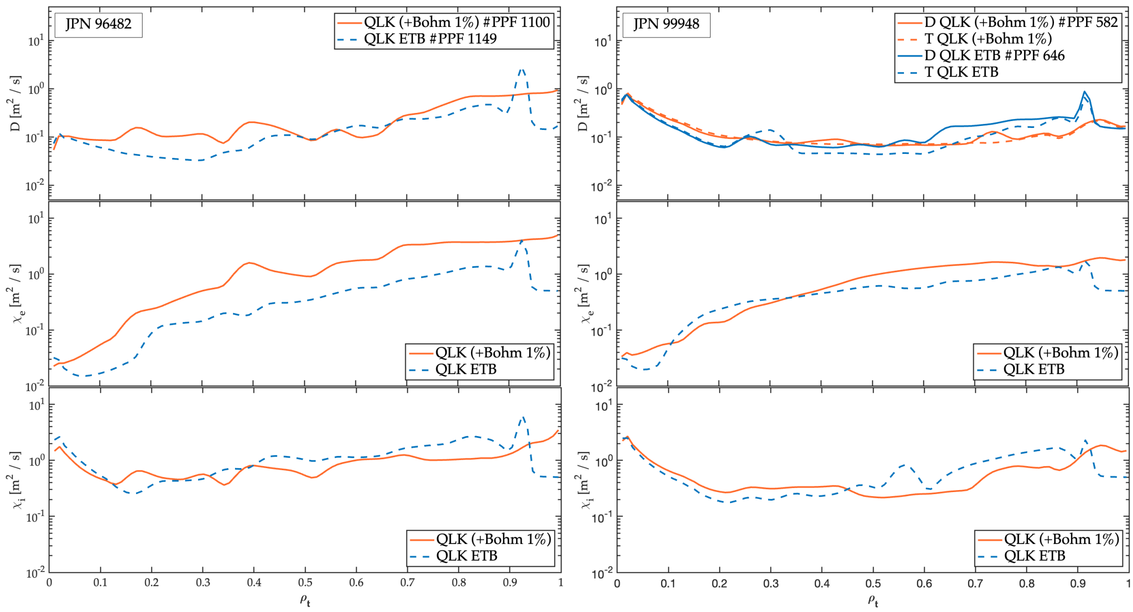

(a) JPN 96482 transport coefficients

(b) JPN 99948 transport coefficients

Figure 5.10. A comparison between the D and D-T transport coefficients (averaged in the reference time interval) computed by QuaLiKiz with and without internal boundary conditions.

5.2.3 Effects of impurities and Z_{eff} profile

As it has been show in the previous section, after modelling the pedestal in the D pulse with the simulation boundary conditions at the separatrix, the density profile starts to be over-predicted in simulations where the impurity transport is predicted too. It has been argued that the possible contributors to the density over-prediction are the NBI particle source and the impurity transport. In this section the sensitivity to the impurity mix composition and to the Z_{eff} profile is studied on the D pulse JPN 96482.

Two different spectroscopy estimates of the impurity mix composition are available for this pulse: the one presented in [62] obtained with the methodology described in [73] estimated from spectroscopy, where $\langle n_{Be}\rangle/\langle n_e\rangle \approx 2.2\%$, $\langle n_{Ni}\rangle/\langle n_e\rangle \approx 0.092\%$ and $\langle n_W\rangle/\langle n_e\rangle \approx 0.0081\%$; the second obtained with the methodology described in [82] based on the $P_{rad,Ni}$ estimate presented in [83], where $\langle n_{Be}\rangle/\langle n_e\rangle \approx 1.7\%$, $\langle n_{Ni}\rangle/\langle n_e\rangle \approx 0.045\%$ and $\langle n_W\rangle/\langle n_e\rangle \approx 0.012\%$. It has to be mentioned that the first estimate from spectroscopy [73] leads to $P_{rad,Ni} \approx 1.9$ MW, while the second estimates $P_{rad,Ni} \approx 1.5$ MW. The assumption on $P_{rad,Ni}$ changes slightly the impurity mix composition, but the effect on the effective impurity choice is around 3% in terms of mass and charge, because the Be is the dominant impurity. In Fig. 5.11 the different available Z_{eff} profiles can be compared: the average Z_{eff} profile obtained in the simulations done with predictive impurity transport with the constrain on $P_{rad,Ni}$ (in blue); the average Z_{eff} profile obtained in the simulations done with predictive impurity transport and the impurity mix composition from spectroscopy presented in Sec. 4.2 (in yellow); the average Z_{eff} profile obtained directly from spectroscopy analysis (in black). Starting from the simulations with internal boundary conditions, the effects of imposing the Z_{eff} profile obtained directly from spectroscopy analysis can be compared with the simulation results presented in Section 5.2.1, where the imposed Z_{eff} profile comes from the simulation results presented in 4.2.

In Fig. 5.12 the TGLF results are shown for the two different Z_{eff} profiles. The only difference in the simulation results can be seen in the electron density profile. Imposing the Z_{eff} profile from spectroscopy analysis slightly improves the agreement with the TRANSP interpretative run. The corresponding QuaLiKiz cases are shown in Fig. 5.13. The sensitivity to the Z_{eff} profile shape results higher in QuaLiKiz with respect to TGLF. Indeed, the temperature are changing together with the density profile. The decrease in the neutron yield can be attributed to a lower penetration of the beams with the consequent decrease in the beam-thermal component of fusion reactions. The overall impact of changing the Z_{eff} profile with internal boundary conditions seems to be modest both in TGLF and in QuaLiKiz.

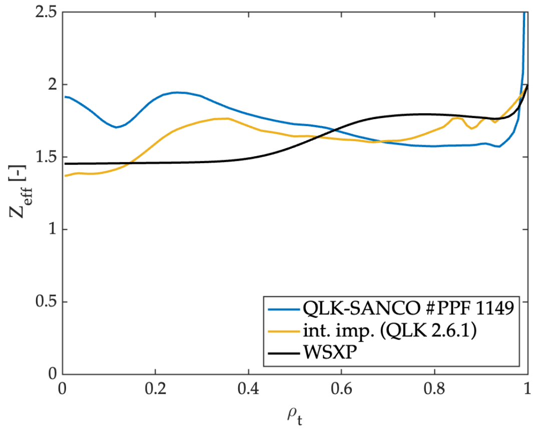

Figure 5.11. Comparison between the different Z_{eff} profiles used in predictive simulations, averaged in the reference time interval plotted against normalised toroidal radius ρ_{tor} for JPN 96482, the WSXP is obtained from [73].

In the last part of the section, we will discuss wether predicting the impurity transport has an impact on simulations where the pedestal is modelled and the boundary conditions are imposed at the separatrix. It has been shown in D pulses (cf. Sec. 4.3 and Sec. 5.2.2) that in these conditions the over-prediction of on-axis density and density peaking can be more severe. In Fig. 5.14 the results of different QuaLiKiz predictions are compared. In the case with internal boundary conditions (orange in Fig. 5.14) the impurity transport is not evolved and the Z_{eff} profiles comes from the predictive simulation presented in Sec. 4.2 with the estimate of spectroscopy analysis [73]. In the case dashed cyan we are modelling the pedestal and evolving the impurity transport with an impurity mixture prescribed to match $P_{rad,Ni}$ in Fig. 5.14, while in the last case (dotted-dashed cyan in Fig. 5.14) the pedestal is modelled but the impurity transport is not evolved by imposing the Z_{eff} profile directly from spectroscopy analysis [73]. It can be seen that the latter case has a strong impact on predictive simulations improving significantly the agreement with the experimental results. The density over-prediction disappears and, through the ion temperature increase, the fusion performance is well predicted. The differences between the two cases where the pedestal is modelled can only be ascribed to the shaping of the Z_{eff} profile (cf. Fig. 5.11). Indeed, the electron density profile is really similar in the two cases from the separatrix to $\rho_{tor} \approx 0.6$ leading to the

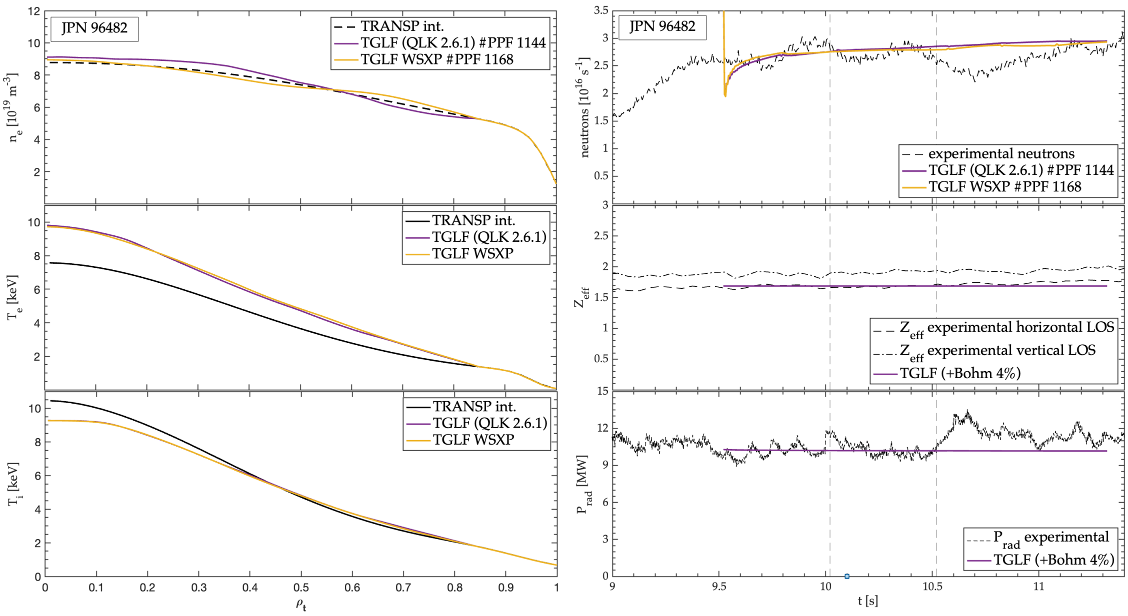

(a) JPN 96482 plasma kinetic profiles **(b)** JPN 96482 plasma time traces

Figure 5.12. JPN 96482: (a) n_e, T_e and T_i plasma profiles predicted with TGLF with internal boundary conditions, compared to TRANSP interpretative profiles; (b) Comparison between experimental and modelled neutron rate, Z_{eff} obtained from Bremsstrahlung measurements along a vertical and horizontal line of sight, and radiated power from bolometry.

similarity of the NBI deposition profiles. The differences in the Z_{eff} profile lead to a decrease of the core dilution which is beneficial for the fusion reactivity and also for the heating deposition.

Since impurities play a crucial role in the evolution of different phenomena in plasmas, the sensitivity to different modelling approaches has been tested with TGLF and QuaLiKiz transport models. Currently, TGLF is not suitable in JINTRAC to predict the impurity transport due to significant numerical instabilities when trying coupling TGLF with SANCO. The effects of impurity on particle and heat transport is taken into account indirectly in TGLF also when the impurity transport is not evolved. The inclusion of high-Z impurities, even if interpretative, is discouraged by the TGLF developing team. On the contrary, QuaLiKiz is suitable in JINTRAC to be coupled with SANCO and predict the impurity transport. A sort of feedback loop exists between impurity and main ion transport. The impurity transport depends on the main ion transport but the transport coefficients computed by QuaLiKiz for the main ion transport depends also on the impurity density. This mechanism cause a significant sensitivity of the model to the impurity mix composition and to the shape of the Z_{eff} profile. When light or medium-Z impurities starts accumulating in the core the turbulent transport computed by QuaLiKiz is reduced. The reduction of the turbulent transport is responsible for the increase in the density in the core and can lead to significant under-predictions of the plasma performance.

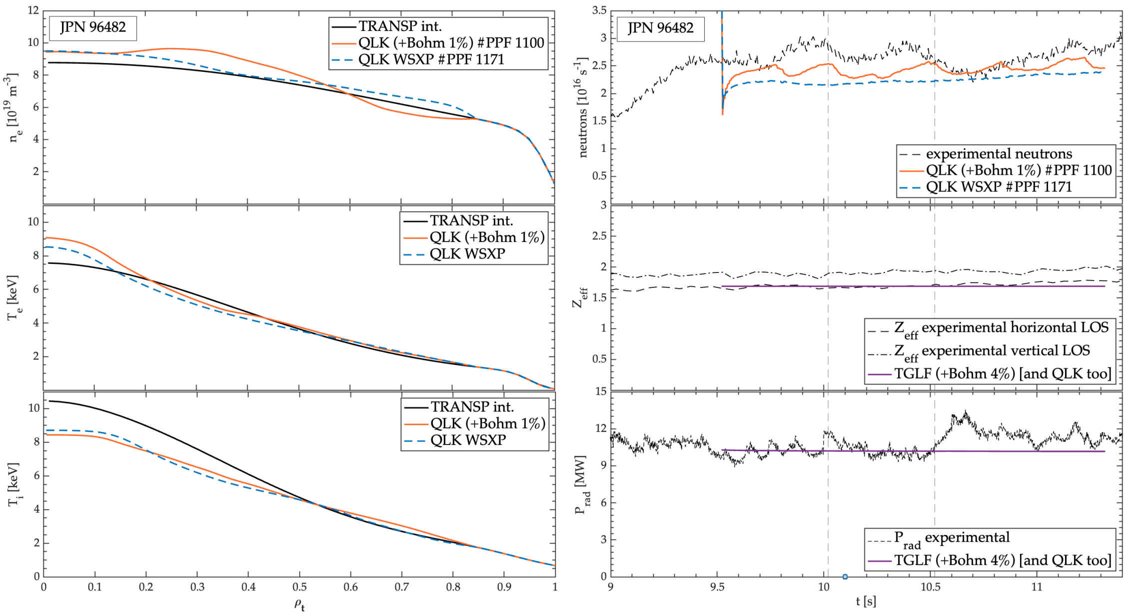

(a) JPN 96482 plasma kinetic profiles

(b) JPN 96482 plasma time traces

Figure 5.13. JPN 96482: (a) n_e, T_e and T_i plasma profiles predicted with QuaLiKiz with internal boundary conditions, compared to TRANSP interpretative profiles; (b) Comparison between experimental and modelled neutron rate, Z_{eff} obtained from Bremsstrahlung measurements along a vertical and horizontal line of sight, and radiated power from bolometry.

The impurity mix composition is determinant too (cf. Sec. 4.4), and an accurate estimate of the Ni present in the discharge is required. In fact, in a Be, Ni, W impurity mixture, when underestimating the Ni content (with Z_{eff} imposed from measurements), the Be concentration results overestimated leading to an overestimate of the dilution with the consequent decrease of the plasma performance. On the contrary, overestimating the Ni concentration reduces the Be dilution leading to an overestimate of the plasma performance. For these reasons an accurate estimate of the Ni concentration from spectroscopy is fundamental in order to obtain reliable prediction of present experiments and future machines.

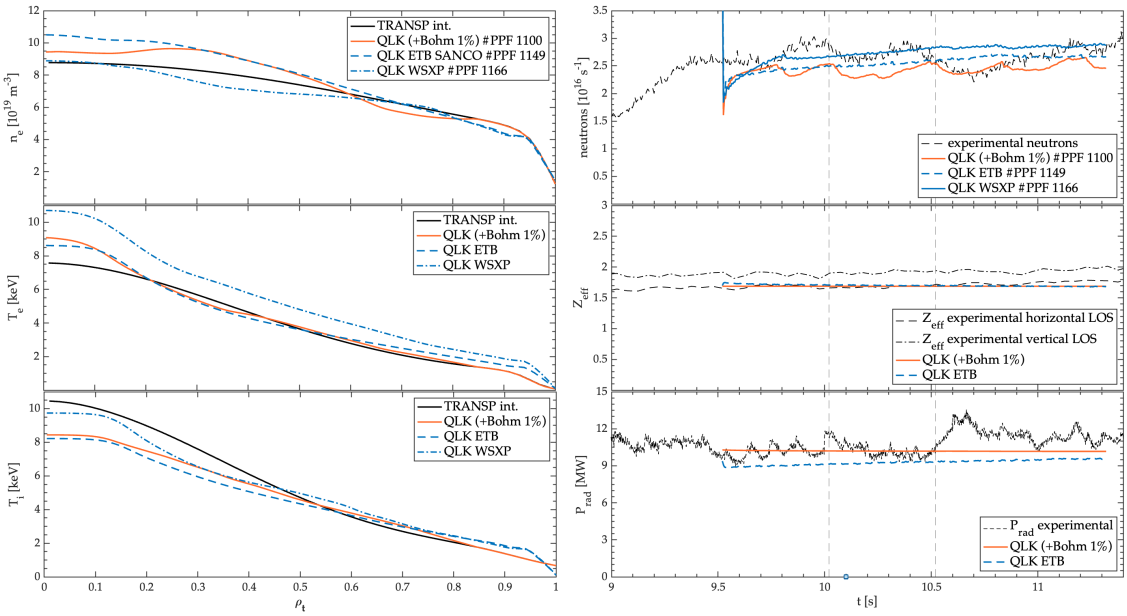

(a) JPN 96482 plasma kinetic profiles

(b) JPN 96482 plasma time traces

Figure 5.14. JPN 96482: (a) n_e, T_e and T_i plasma profiles predicted with QuaLiKiz with internal boundary conditions and with the edge transport barrier modelling with the boundary conditions at the separatrix, compared to TRANSP interpretative profiles; (b) Comparison between experimental and modelled neutron rate, Z_{eff} obtained from Bremsstrahlung measurements along a vertical and horizontal line of sight, and radiated power from bolometry.

5.3 D-T fuel mix control with pure T gas puff and D pacing pellets

The work presented in this section appeared in its first reduced version in [82]. Here it will be extended and adjusted for the purposes of this dissertation.

Fuel mix control is a relevant problem in present experiments featuring mixed isotope fusion plasmas, and it will be crucial in future fusion reactors operating with a D-T plasma mixture. To maximise the D-T thermal reactions the main ion plasma mixture has to be close to 50-50. By means of predictive simulations different fuelling schemes can be evaluated and compared. Integrated modelling can provide a guidance to arrive to a suitable recipe for the desired conditions. The simulations are performed using QuaLiKiz transport model to predict the evolution of the current density profile, the D and T densities, the electron density, the ion and electron temperatures, while the impurity transport (i.e. n_{Be}, n_{Ni} and n_W) is computed by SANCO. The impurity mixture composition is determined imposing the Z_{eff} inferred from Bremsstrahlung measurements, adjusting the Ni content to match the $P_{rad,Ni}$ estimate from [83], and W concentration is obtained matching the total radiated power. The Be, assumed as dominant impurity, is determined to match the plasma dilution. The toroidal velocity profile is imposed in the simulations form charge exchange measurements, because it has been observed a strong rotation under-prediction simulating the D-T *baseline* scenario. The equilibrium is computed self-consistently with the evolution of the plasma kinetic profiles by ESCO equilibrium solver. Heating deposition profiles from NBI and ICRH are computed by PENCIL-PION. FRANTIC is responsible for the computation of the ionization sources (not measured at JET). The boundary conditions of the simulations are imposed at the separatrix which allows to investigate the effects of imbalanced D-T gas puff and of pure D pacing pellets on the main ion plasma composition. The pedestal is modelled *ad hoc* with an effective ELM averaged diffusivity and conductivity to reproduce the experiment.

Before the beginning of the D-T campaign, the sensitivity of plasma composition to different fuelling schemes has been studied for the (3.5 MA / 3.3 T) *baseline* scenario, extrapolating to D-T plasma mixture the JPN 96482. In Fig. 5.15 it can be seen that the predicted performance of QuaLiKiz simulations follows the trend of the TRANSP interpretative analysis done with the experimental profiles of the flat-top phase of the JPN 96482 imposing different main ion plasma compositions. During this preliminary study, it has been shown that a balanced D-T main ion plasma mixture can be obtained by an appropriate balance of the external particle sources. The T concentration profile predicted in QuaLiKiz simulations is flat with respect to the radial coordinate, leading to a core T concentration almost equal to the volume averaged T concentration. Similar results have been obtained in [85] simulating multiple-isotope particle transport.

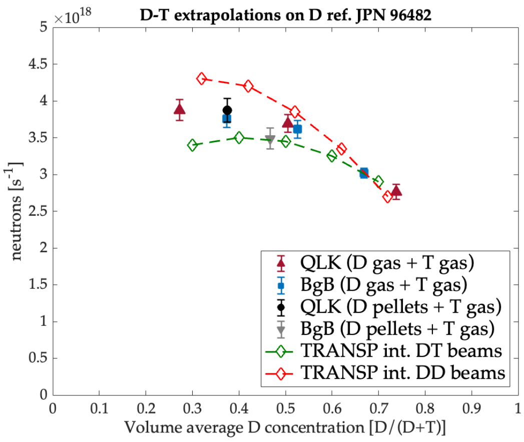

Figure 5.15. Sensitivity of plasma composition to different fuelling schemes for the (3.5 MA / 3.3 T) *baseline* scenario, comparing the performance of fully predictive JINTRAC simulations done with QuaLiKiz and Bohm gyro-Bohm transport model in presence of D-T balanced beams (full markers) to TRANSP interpretative analysis (open markers) with D-T balanced beams or pure D beams.

With the contribution of integrated modelling the *baseline* fuelling scheme has been assessed with a balanced D-T gas puff during the ramp-up phase, and with pure T gas puffing with the injection of D pacing pellets during the flat-top phase of the discharge. It has to be mentioned that pacing pellets are required in the *baseline* scenario for promoting ELMs, for high and medium-Z impurities influx control and for density control. Since JET pellet injector is not compatible with T, the D pellets used in JET D-T *baseline* experiments are the first cause of imbalance in the external particle source and eventually of the main ion plasma composition. The experimental condition where the fuelling of different hydrogen isotopes occurs through different channels is considered as an opportunity to test the reliability of the particle sources estimate in core-pedestal integrated simulations.

The *baseline* D-T pulse chosen for this study is the JPN 99797 with balanced D-T NBI injection, the main plasma parameters of which are shown in Fig. 5.16, while the averaged plasma parameters in the time interval chosen for the analysis are reported in table 5.1. During the flat-top, the gas puffing is pure T and 35 Hz 2 mm pellets lead to a nominal pellet source $S_{pel} = 0.8 * 10^{22} s^{-1}$. The flat-top time interval to be compared with predictive simulations is 1.2 s long, starting from 9.5 s, when the T concentration, measured by the Balmer-alpha spectrum measured near the subdivertor pressure gauge (in the edge), is around 53%. The simulations start 500 ms before the time interval of interest in order to relax the initial conditions taken from measurements. Thus, the relevant quantities, to be compared with measurements, should be computed self-consistently by the transport model. The simulations done on this pulse can be divided in two sets: the first one where particle sources are modelled as gas puff (both the contribution from gas puff and pellets) to determine the total particle sources required to sustain the experimental pedestal density; the second, where D pellets are modelled in presence of T gas puff. Being the recycling set to zero in these simulations, the ionization sources modelled as gas puff are also including the wall ionization sources. At this point of the work it is impossible to distinguish the particle sources from the gas puff and those from the wall.

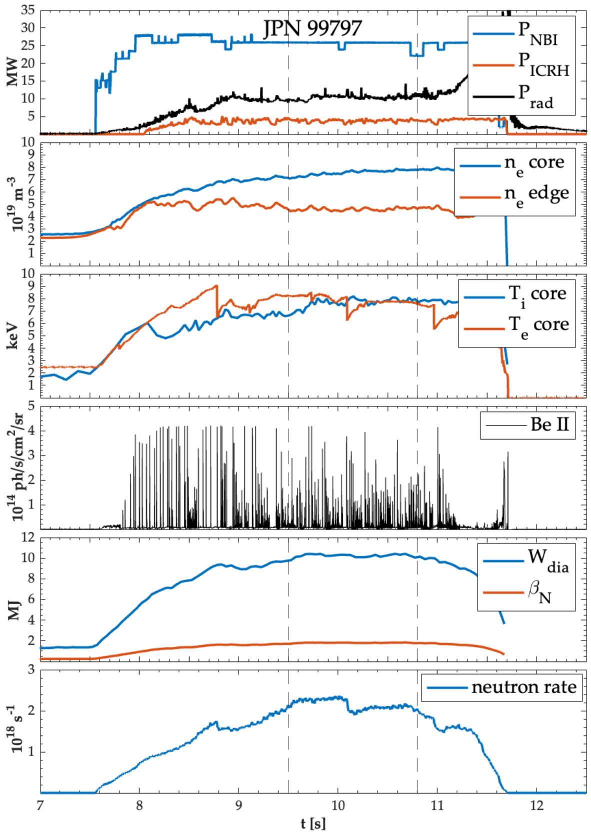

Figure 5.16. Experimental evolution of the main plasma parameters for the D-T JPN 99797 a (3.5 MA / 3.3 T) *baseline* scenario. From top to bottom are shown: NBI and ICRH auxiliary heating power and radiated power (from bolometer); core and edge line average electron density (from JET multi-channel infrared interferometer); on-axis electron temperature (from electron cyclotron emission radiometer) and core ion temperature (from high resolution x-ray crystal spectrometer looking at Ni^{+26} emission; Be II emission (from visible spectroscopy, showing ELM behavior); plasma thermal energy and β_N and neutron rate.

It has been found, in agreement with the modelling results presented in Sec. 4.1, that the simulation results are not sensitive on whether the external particle sources are modelled with or without a proper pellet modelling. In Fig. 5.17 the results of modelling are shown in the case where pellets are modelled. We want to underline that, with the exception of small numerical fluctuations in the time traces,

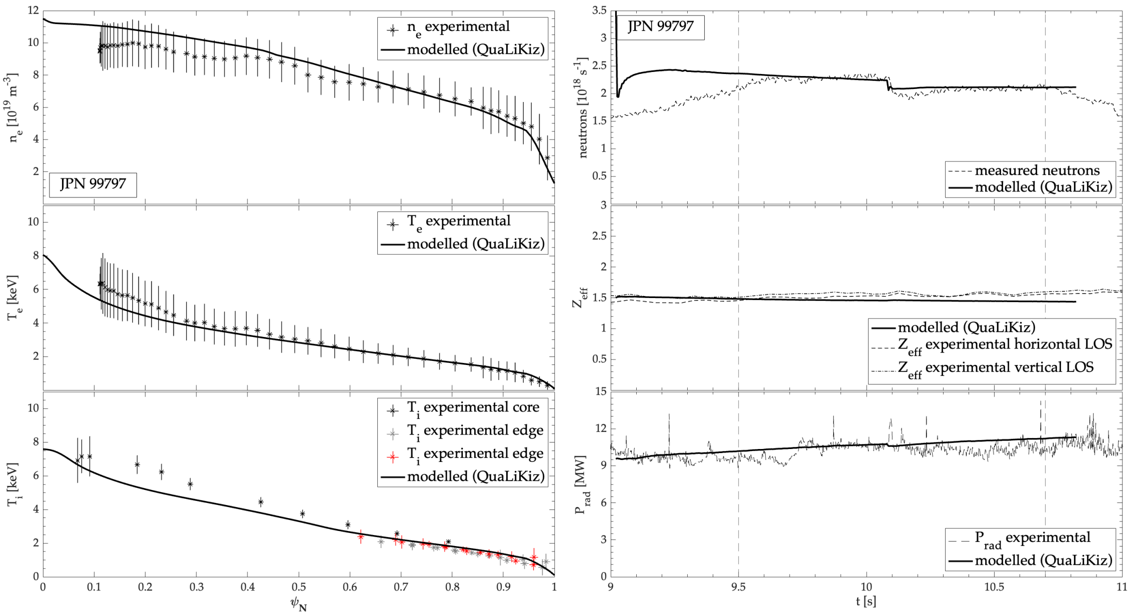

(a) JPN 99797 plasma kinetic profiles **(b)** JPN 99797 plasma time traces

Figure 5.17. JPN 99797: (a) Comparison between experimental and modelled n_e, T_e and T_i; The electron density experimental points are HRTS measurements, the electron temperature experimental points are high resolution Thomson scattering measurements (HRTS, black crosses) and the ion temperature experimental points are beam CX spectroscopy measurements. Measurements and predictions are averaged over the time interval of interest. The vertical error bars combine the RMS over the time interval and the measurements uncertainties, the horizontal error bars are the RMS of the ψ_N coordinate mapped from an EFTP equilibrium. (b) Comparison between experimental and modelled neutron rate, Z_{eff} obtained from Bremsstrahlung measurements along a vertical and horizontal line of sight, and radiated power from bolometry.

the simulation results without a separate modelling of the pellets coincides with the simulation results shown in Fig. 5.17. The agreement between the modelled and the experimental measurements is good in all the quantities selected as figure of merit. The impurity transport is well predicted as well. The increase in the radiated power is captured in the simulation without assuming high-Z impurities influxes. At $t \approx 10.1$ s, a sawtooth crash is modelled with the Kadomtsev model [86]. It can be seen that the modelled performance is in agreement with measurements both before and after the crash, showing that also the equilibrium computed by ESCO self-consistently with the evolution of the plasma kinetic profiles is really close to the experimental equilibrium.

In Fig. 5.18 it can be seen the comparison between the particle sources modelled with or without separate pellet modelling. The different fuelling channels are dominant in different regions of the plasma. The NBI fuelling dominates the core fuelling for $\psi_N \leq 0.6$, the gas puffing is the dominant fuelling channel in the region with $\psi_N \geq 0.6$. The effects of pellets depend on the injection parameters and can be used to control the plasma compositions as shown in [87]. Moreover, a different

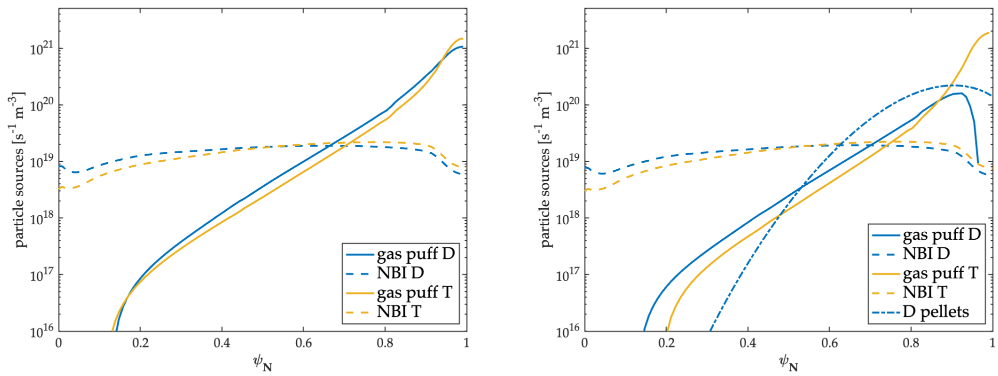

(a) JPN 99797: particle sources with pellets and gas puff modelled as gas puff (gas only cases)

(b) JPN 99797: particle sources with D pellets modelling and gas puff modelling

Figure 5.18. JPN 99797: Comparison between the particle sources in the first set of simulations "gas only" and the second set of simulations with D pellet modelling.

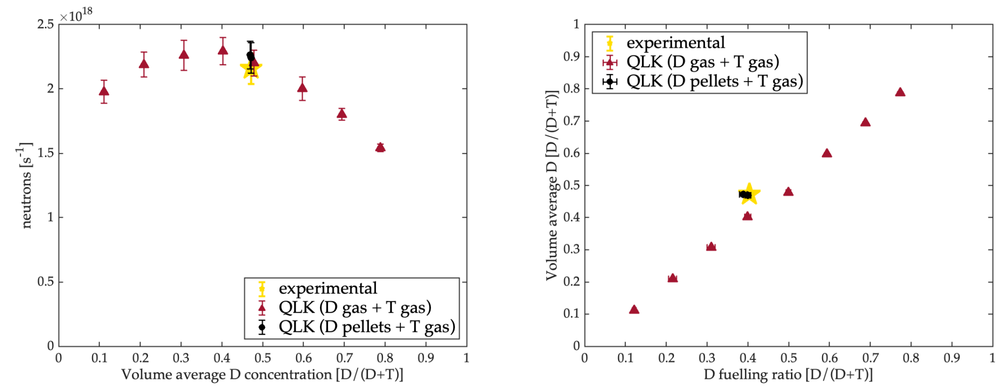

(a) JPN 99797: plasma performance in dependence on main ion plasma composition

(b) JPN 99797: volume avergage D concentration in dependence on D fuelling ratio

Figure 5.19. JPN 99797: (a) comparison between the performance of the first set of simulation "gas only", the simulations with pellet modelling and the experimental data; (b) comparison between the experimental and modelled volume average D concentration and the fuelling D ratio.

fuelling efficiency can be expected for the different hydrogen isotopes. For this experiment, pellets are modelled using the continuous pellet model [88] with a gaussian source of D centred at the normalised toroidal flux coordinate $\rho_{tor} = 0.9$, with a width equal to 0.15 for a total particle source $S_{pel} = 0.61 * 10^{22} s^{-1}$ which matches the experimental data. In addition to this, a different simulation was performed, where the pellet particle source modelled is equal to the nominal particle source $S_{pel,nom} = 0.8 * 10^{22} s^{-1}$.

In Fig. 5.19(a) it can be seen that the neutron yield can be reproduced both in simulations where particle sources are modelled as gas puff and in simulations with a separate pellet modelling. In Fig. 5.19(b), when comparing the experimental and modelled fuelling mixture, it can be seen that pellet modelling results differ from the simulation results where particle sources are modelled as gas puff, and the main ion fuelling composition agrees with the experimental data. In presence of D pellet modelling, it can be seen that with a slightly T rich fuelling ($T_{fuel} \approx 60\%$) a 50-50 main ion plasma mixture is obtained in line with the experiment. The reason for these results can be ascribed to the higher retention time of pellet particles with respect to gas puff particles.

An interesting outcome of the present analysis is that in the simulation with the effective particle source from pellets ($S_{pel} = 0.61 * 10^{22} s^{-1}$) in absence of a residual D source modelled as gas puff, it is impossible to match the T concentration time evolution not even imposing the nominal pellet particle source. Plasma main ion composition and sources are shown in Fig. 5.20. Under the assumption of D and T equivalent wall ionization sources, the estimate presented in [89] could be applied. The D wall ionization source can be computed with the following formula:

$$\phi^D \approx \phi^T = (\phi^D_{NBI} + \phi^T_{NBI})$$

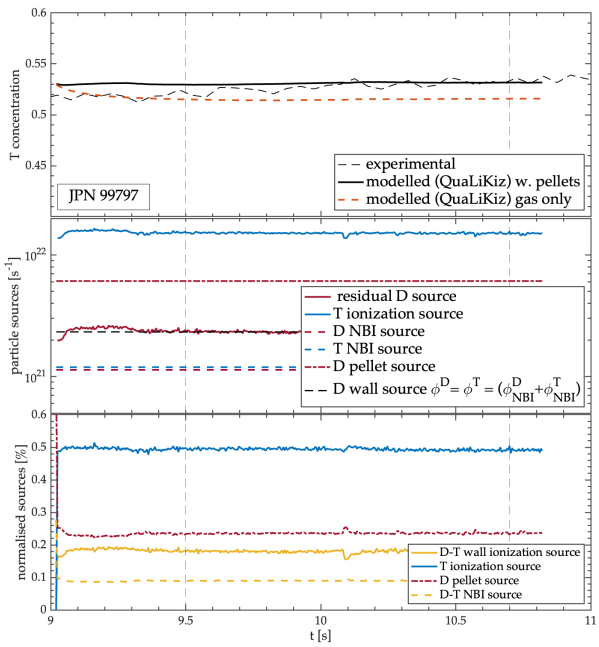

Figure 5.20. JPN 99797: modelled and experimental T concentration evolution measured by the Balmer-alpha spectrum form the subdivertor pressure gauge; estimate of particle sources; normalised particle sources with respect to the total particle sources;

The residual D source required in this work to match the experimental evolution of the T concentration is in agreement with the estimate of the D wall ionization source calculated with [89]. This case corresponds to the lower limit of the pellet fuelling efficiency. It has to be mentioned that, imposing the nominal pellet source, the residual D source required to match the experimental T concentration is reduced to around 1% of the total particle sources. This estimate of wall ionization sources proposed after a dedicated experiment performed during DTE1 seems to be valid also in DTE2, despite the substitution of the C-wall with the Be/W wall. This should not be cause of concern. The fuel retention in Be/W wall is significantly lower than the fuel retention of the C-wall [90]. Moreover, in the dedicated experiment designed for DTE1 the wall was pre-loaded in D in order to see its contribution to the main ion plasma composition through wall ionization sources. If the wall does not retain more fuel, due to the pre-loading, it can be argued that the behavior of the loaded wall is similar to the behavior of a metallic wall with a lower fuel retention. However, the wall ionization sources estimated with this approach are 20% of the total ionization sources.

5.4 Chapter summary

We have presented the comparison between the extrapolations done in preparation to DTE2 campaign and the experimental fusion power obtained by the *baseline* scenario during the campaign. The experimental results are well in line with what was expected by the intense modelling activity done in preparation to the campaign and the trend of the experimental results seems to rely on the upper bound of the uncertainty on the predicted performance.

Due to the differences in the experimental boundary conditions, the predictive modelling results on three different discharge have been discussed thorough a progressive increase of the simulation complexity. The 3.5 MA D discharge JPN 96482 has been compared to the D-T discharge JPN 99948 both in the experiment phenomenology and in the modelled results. In particular, the two pulses have been modelled with the first principle transport models QuaLiKiz and TGLF. A systematic comparison between the results given by the two transport models sharing the same experimental boundary conditions and simulation settings has been presented. The modelling starts from simplified simulations where only electron density, D and T densities, electron and ion temperature are predicted imposing the boundary conditions inside the plasma. It has been shown that the use of simulation parameters tuned on the D pulse leads to an under-estimate of the D-T predicted performance, in the reference time interval, with both transport models. Therefore, simulations with internal boundary conditions can be considered for establishing the lower limit of the expected fusion performance.

To ensure the predictive capability from the experimental results achieved in D plasmas to D-T main ion plasma composition, with the QuaLiKiz transport model the two pulses have been successfully reproduced in simulations where boundary conditions are imposed at the separatrix. In these simulations, the pedestal region is modelled by imposing an effective ELM average conductivity and an effective ELM average diffusivity under the assumption of $\chi/D = 4$. This methodology has been extensively tested building the extrapolation database for the moderate *baseline* scenario before the deuterium-tritium experimental campaign. Modelling with boundary conditions at the separatrix allows to predict the impurity transport and treat self-consistently the mutual interaction between main ion transport and multiple impurity transport.

Impurity mix composition plays a crucial role in the reliability of predictive simulations. Referring to the impurity mix composition of JET, Be is the dominant impurity and determines the plasma dilution in absence of other (injected) low-Z impurities, while, the W is the main plasma radiator. In this picture, the presence of medium-Z impurities, such as Ni, can hide part of the dilution effects and contribute to the radiated power decreasing the W concentration required to match it. An accurate estimate of Ni concentration becomes fundamental to deal with these effects. It has been also shown that impurity transport can determine density over-prediction and density peaking. On the other hand, when using interpretative impurities, the ion transport is not self-consistent because the impurity density profiles don't evolve. In this latter case the estimate of the Z_{eff} profile can affect significantly the results of the predictive simulations both in plasma kinetic profiles and in performance.

The D-T pulse JPN 99797 has been chosen for studying the D-T fuel mix control in presence of D-T balanced beams. During the flat-top phase the gas recipe consist on pure T gas puffing and D pacing pellets. With the predictive modelling it has been demonstrated that the pulse can be reproduced in the time modelling gas puff and pellets separately, or modelling all particle sources (except those from the NBI) as gas puff. The pulse fits with the purpose of this dissertation because of the duration of the stable part of the discharges which allows to evolve the main ion plasma composition. The boundary conditions set at separatrix are suitable for the QuaLiKiz fully predictive simulations with the exception of the toroidal velocity, found significantly under-predicted in D-T simulations. The main ion plasma composition turns out to be almost constant in the radial profile, despite strong imbalance in the gas puff particle sources. The different fuelling channels are dominant in different plasma regions, with the NBI particle sources dominating the region with $\psi_N \leq 0.6$. It has been shown that matching experimental fuelling mixture can be done only modelling pellet particle sources which exhibits a higher retention time with respect gas puff particle sources. In simulations with pellets, a residual D particle source is required to reproduce the evolution of the main ion plasma composition, independently on using the nominal pellet particle source or the effective particle source. When using the effective pellet particle source, the residual D particle source found in simulations is in agreement with the estimate proposed for wall particle sources after DTE1 under the assumption of similar D and T wall particle sources. In this condition, the lower limit of pellets fuelling efficiency has been identified.

Chapter 6

Conclusions

In this thesis we have presented the results of predictive integrated modelling performed using the reduced first principle transport models QuaLiKiz and TGLF for JET baseline scenario. We have developed a robust methodology to collect reliable results while predicting and optimising future plasma scenarios. In preparation to JET D-T operations we have studied the performance of the baseline scenario in dependence to different operating conditions and we have optimised the fuelling scheme.

We have validated QuaLiKiz and TGLF against moderate β baseline plasmas achieved in D pulses both in C-wall and in ITER-like wall. The extrapolation capability has been demonstrated for the first time at higher plasma current and higher toroidal magnetic field scaling the reference plasma density while keeping constant the Greenwald density fraction.

The extrapolation to D-T main ion plasma composition have been performed under a wide range of assumptions. We compared the predicted performance for baseline scenarios at higher plasma current (i.e. 3.8 MA, 4.2 MA and 4.5 MA), with the optimistic assumption of an available auxiliary heating $P_{aux} = 40$ MW. It has been shown that the plasma performance shouldn't increase significantly with increasing plasma current. The JET baseline scenario is not expected to benefit of the increase in plasma current (i.e. increasing plasma density) since JET is limited in the auxiliary heating power.

The effects of the impurity mixture have been assessed performing predictions with Be and Ni as single dominant impurity. We studied a realistic impurity mixture of Be, Ni and W, starting from the impurity mixture of the reference baseline plasma and adjusting the W content to obtain a radiated power such that $P_{rad}/P_{aux} \approx 30\%$. Expected fusion power in presence of an impurity mixture of Be, Ni and W is in line with the one expected assuming Be as single dominant impurity. This is a consequence of the sensitivity of plasma performance to dilution. Finally, we have explored the sensitivity of the baseline scenario to the available heating power and assessed the fuelling scheme required to sustain a 50-50 D-T baseline plasma in presence of balanced D-T NBI injection.

Collecting the experimental results in DTE2 we have demonstrated that the baseline performance (averaged over 0.5 s, which corresponds to two confinement times) is well in line with the fusion power computed by means of predictive modelling. This result is encouraging because it shows that reduced first principle transport models are well describing the turbulent transport in the plasma core also in presence of multiple hydrogen isotopes. Moreover, being the experiments well in line with the predictions both in *hybrid* and in *baseline* scenarios, it is suggesting that the predictive modelling ongoing for ITER scenario development is reliable. On the other hand, JET data collected during DTE2 will contribute to the improvement of present transport models in the view of a further increase of the model prediction capabilities.

Baseline D-T scenario did not achieved the duration of 5 s in high performance aimed for DTE2, and it early terminated due to radiative collapses. The reasons for these terminations are still under analysis, but the uncontrolled increase of density with the difficulties in sustaining regular ELMs seems to be responsible for high-Z impurities accumulation in the low field side, leading to an increase in the radiated power until radiative collapse. This evolution was not expected by the predictive modelling performed in preparation to the experimental campaign.

In the simulations where the experimental boundary conditions of DTE2 were imposed, we have shown the importance of a proper modelling of the pedestal. The increase in plasma radiated power is predicted when imposing the experimental pedestal in the integrated modelling also in absence of impurity influxes. This is an important insight from our modelling: in absence of reliable first principle transport models describing the plasma edge, we have assumed the pedestal in D-T main ion plasma composition to be similar (or scaled at constant Greenwald fraction in higher plasma current cases) to the pedestal in D plasmas. From the data analysis performed on D-T baseline pulses we have seen significant differences both in the pedestal height and in the pedestal width with respect to D pulses. The D-T pedestal shows higher density and larger width with respect to the pedestal in D pulses, and this difference may play a crucial role in the mutual interaction between core transport and pedestal transport. Therefore, plasma transport simulations with core-pedestal coupling should be pursued in future work together with the development of more reliable models describing the pedestal evolution. In any case, the methodology presented here can be used to develop and optimise plasma scenarios for future experiments, as it has been used in assisting JET team activities when assessing the fuelling scheme to sustain a 50-50 D-T main ion plasma mixture.

Finally, we have analysed a D-T pulse in order to obtain a more accurate estimate of the particle sources in presence of pure T gas puff, D pacing pellets and balanced D-T NBI injection. We have applied the methodology described in this thesis to reproduce with predictive simulations the evolution of the pulse. We have reproduced the global characteristics of the pulse both in a simulation where pellet sources and gas puff sources are modeled as gas puff, and in a simulation where pellet sources are modeled separately. We have confirmed that in terms of performance gas puff and pellets can be modeled as very similar particle sources.

Modelling T gas puff and D pellets separately allows to reproduce the experimental fuelling ratio of the fuelling scheme. In these simulations, we have observed a higher pellet particle retention time with respect to the particle injected through gas puffing. The different fuelling channels are dominant in different plasma regions. NBI injection dominates the plasma core ($\psi_N < 0.5$), while pellets and gas puffing are the dominant fuelling channels in the region where $\psi_N \geq 0.5$. Despite a significant imbalance of D and T particle sources in the edge region ($\psi_N \geq 0.9$), the main ion plasma composition results constant through the plasma radial coordinate. The mixing velocities predicted by QuaLiKiz are faster than in the Bohm gyro-Bohm transport model, leading to the constant main ion plasma composition.

While modelling the experimental pellet particle source, we found that a residual D particle source is required in the simulations to reproduce the evolution of the main ion plasma composition. This could be considered in contrast with the experiments where the D fuelling is performed only by pellets injection, but in our simulations the gas puff sources include the particle sources both from gas puffing and from the wall. Therefore the residual D source can be attributed to the wall recycling. Assuming a similar wall recycling both for D and T, we have computed the D wall particle sources in accordance to a methodology proposed after DTE1, showing that our residual D particle source is very close to the wall particle source DTE1. The results of this modelling activity could be affected by the assumptions done on the effective particle diffusivity D in the pedestal region. Despite that, we do not expect differences in the fuelling isotope ratio and, consequently, in the magnitude of the wall particle sources with respect to the total particle sources. Further analysis will be performed with core-edge-SOL coupled simulations in order to refine and confirm the results of these analyses.

Bibliography

[1] L.J. Reinders "The Fairy Tale of Nuclear Fusion" *Springer* 2021

[2] D. Fabbi 2022 *Domino* **1** 7

[3] F. Maronta 2022 *Limes* **3** 273

[4] A. Colibasanu 2022 *Domino* **2** 73

[5] G. Pucella and S.E. Segre "Fisica dei Plasmi" *Zanichelli* 2010

[6] P. Caldirola, R. Pozzoli and E. Sindoni "Il fuoco della fusione termonucleare controllata" *Arnoldo Mondadori* 1984

[7] J. Mailloux *et al* 2022 *Nucl. Fusion* **62** 042026

[8] J. Wesson, 1999, "The science of JET", JET-R(99)13

[9] F. Romanelli and R. Kamendjeon behalf of JET-EFDA Contributors 2009 *Nucl. Fusion* **49** 104006

[10] TFR Group 1985 *Nucl. Fusion* **25** 1025

[11] L.A. Artsimovich, V.D. Shafranov 1972 "Tokamak with non-round section of the plasma loop" *JET P. Lett.* 15:51-54

[12] F. Wagner *et al* 1982 *Phys. Rev. Lett.* **62** 1408

[13] ASDEX Team 1989 *Nucl. Fusion* **29** 1959

[14] A. Kallenbach *et al* 2017 *Nucl. Fusion* **57** 102015

[15] M. Keilhacker *et al* 1987 *Plasma Phys. Control. Fusion* **14** 1401

[16] P.T. Lang *et al* 2013 *Nucl. Fusion* **53** 043004

[17] A. Loarte 2001 *Plasma Phys. Control. Fusion* **43** R183

[18] L. Garzotti *et al* 2019 *Nucl. Fusion* **59** 076037

[19] R.J. Hawryluk *et al* 1998 *Phys. of Plasmas* **5** 1577

[20] M.G. Bell *et al* 1995 *Nucl. Fusion* **35** 1429

[21] M. Keilhacker *et al* 1999 *Nucl. Fusion* **39** 209

[22] L.D. Horton *et al* 1999 *Nucl. Fusion* **39** 993

[23] J. Garcia *et al* 2017 *Plasma Phys. Control. Fusion* **59** 014023

[24] F.G. Rimini *et al* "Towards thermonuclear plasmas: praparation for D-T operation with an ITER-like wall at JET" at 46^{th} *EPS Conference on Plasma Physics*, 2019

[25] J. Garcia *et al* 2021 *Proc. 28th IAEA Fusion Energy Conference* paper EX/1

[26] F. Koechl "Modelling of Transport and Pellet Fuelling in ITER-relevant Plasmas", PhD Thesis, TU Wien, 2009

[27] J.P.H.E. Ongena, M. Evrard and D. McCune 1998 *Fusion Technology* **33** 2T

[28] M. Marin "Integrated modelling of multiple-ion tokamak discharges: validation and extrapolation", PhD Thesis, Eindhoven University of Technology, 2021

[29] W.M. Tang, J.W. Connor and R.J. Hastie 1980 *Nucl. Fusion* **20** 1439

[30] B.N. Rogers, J.F. Drake, and A. Zeiler *Phys. Rev. Lett.* **81** 4396

[31] D.R. Hatch *et al* 2017 *Nucl. Fusion* **57** 036020

[32] M. Kotschenreuther *et al* 2019 *Nucl. Fusion* **59** 096001

[33] D. Dickinson *et al* 2012 *Phys. Rev. Lett.* **108** 135002

[34] G.M. Staebler *et al* 2018 *Phys. Plasmas* **25** 056113

[35] R.D. Hazeltine *et al* 2012 *Phys. Fluids* **18** 1778

[36] A. Taroni *et al* 1994 *Plasma Phys. Control. Fusion* **36** 1629

[37] M. Erba *et al* 1997 *Plasma Phys. Control. Fusion* **39** 271

[38] G.M. Staebler 2007 *Phys. Plasmas* **14** 055909

[39] G.M. Staebler *et al* 2016 *Phys. Plasmas* **23** 062518

[40] G.M. Staebler *et al* 2021 *Plasma Phys. Control. Fusion* **63** 015013

[41] C. Bourdelle *et al* 2016 *Plasma Phys. Control. Fusion* **58** 014036

[42] J. Citrin *et al* 2017 *Plasma Phys. Control. Fusion* **59** 124005

[43] C. Bourdelle *et al* 2007 *Phys. Plasma* **14** 112501

[44] A. Casati *et al* 2009 *Nucl. Fusion* **49** 085012

[45] G. Wang *et al* 2011 *Phys. Plasma* **18** 082504

[46] M. Romanelli *et al* 2014 *Plasma and Fusion Research* **9** 3403023

[47] G. Cenacchi and A. Taroni "JETTO: a free-boundary plasma transport code", ENEA Report 1988

[48] C.D. Challis *et al* 1989 *Nucl. Fusion* **29** 563

[49] M. O'mullane "ADAS Atomic Data and Analysis Structure" *CXSFIT: User manual*, 2007

[50] V.S. Chan *et al* "Current drive and profile control in low aspect ratio tokamaks" at 22^{nd} *EPS Conference on Plasma Physics*, 1995

[51] L.G. Eriksson, T. Hellsten, U. Willén 1993 *Nucl. Fusion* **33** 1037

[52] L. Villard *et al* 1995 *Nucl. Fusion* **35** 1173

[53] D. Gallart *et al* 2018 *Nucl. Fusion* **58** 106037

[54] H.S. Bosh and G.M. Hale 1992 *Nucl. Fusion* **35** 1173

[55] S. Tamor 1981 *Journal Comp. Phys.* **40** 104119

[56] J. Simpson 2019 "Impact of the neutral source on the pedestal using JETTO-EIRENE and a comparison of the EIRENE and FRANTIC neutral models", JINTRAC internal Report.

[57] L. Taroni 1994 *Proc. 21st EPS Conference on Controlled Fusion and Plasma Physics* ECA vol. **18B**, part I, p. 102

[58] G. Cenacchi and M. Rulli 1988 *Upgrading of an equilibrium transport code for a multispecies free-boundary plasma*, ENEA Report RTI/TIB(88)5

[59] L.L. Lao 1985 *Nucl. Fusion* **25** 1611

[60] R. Albanese *et al* at *ISEM, Versailles*, 2003

[61] V.K. Zotta *et al* "Moderate beta baseline scenario in preparation to D-T operations at JET" at 47^{th} *EPS Conference on Plasma Physics*, (P3.1052), 2021

[62] V.K. Zotta *et al* 2022 *Nucl. Fusion* **62** 076024

[63] E. Joffrin *et al* 2019 *Nucl. Fusion* **59** 112021

[64] F. Troyon *et al* 1984 *Plasma Phys. Control. Fusion* **26** 209

[65] K. Miyamoto 2005 *Plasma Physics and Controlled Nuclear Fusion*, Springer-Verlag

[66] J. Garcia *et al* 2019 *Nucl. Fusion* **59** 086047

[67] F.J. Casson *et al* 2020 *Nucl. Fusion* **60** 066029

[68] J. Garcia *et al* 2017 *Nucl. Fusion* **57** 014007

[69] A. Mariani *et al* 2021 Nucl. Fusion **61** 066032

[70] W.A. Houlberg, K.C. Shaing, S.P. Hirshman and M.C. Zarnstorff, 1997 *Phys. Plasmas* **4** 3230

[71] R. Pasqualotto *et al* 2004 *Rev. Sci. Intrum.* **75** 3891

[72] N.C. Hawkes *et al* 2018 *Rev. Sci. Intrum.* **89** 10D113

[73] M. Sertoli *et al* 2019 *J. Plasma Phys.* **85** 905850504

[74] G. Kamelander and D.J. Sigmar 1992 *Phys. Scr.* **45** 147

[75] Hyun-Tae Kim *et al* 2020 *Nucl.Fusion* **60** 066003

[76] O. Linder *et al* 2019 *Nucl. Fusion* **59** 016003

[77] L. Garzotti at *IoP* 48^{th} *Annual Plasma Physics Conference*, 11 - 14 April 2022, Liverpool, UK

[78] I. Predebon *et al* "Isotope mass dependence of pedestal transport in JET H-mode plasmas" submitted to *Nucl. Fusion*

[79] L. Garzotti *et al* "Development of baseline scenario for high fusion performance at JET" to be submitted to *Nucl. Fusion Special Issue*

[80] L.C. Ingesson, "The Mathematics of some Tomography Algorithms at JET", JET Reports JET-R(99)08, 1999

[81] Hyun-Tae Kim *et al* in preparation for *Nucl. Fusion special issue*

[82] V. K. Zotta *et al* "Predictive modelling of D-T fuel mix control with gas puff and pellets for JET 3.5 MA baseline scenario" at 48^{th} *EPS Conference on Plasma Physics*, (P2a.115), 2022

[83] A. Czarnecka *et al* 2011 *Plasma Phys. Control Fusion* **53** 035009

[84] M. Valovic *et al* 2008 *Nucl. Fusion* **48** 075006

[85] M. Marin *et al* 2020 *Nucl. Fusion* **60** 046007

[86] B.B. Kadomtsev 1975 *SOV J. PLASMA PHYS.* vol. 1 no. 5, 389

[87] M. Valovic *et al* 2021 *Control of H/D isotope mix by peripheral pellets in H-mode plasma in JET* at 28^{th} *IAEA Fusion Energy Conference* (FEC 2020)

[88] V. Parail *et al* 2009 *Nucl. Fusion* **49** 075030

[89] T.T.C. Jones *et al* 1998 Proc. 25^{th} *EPS Conference on Controlled Fusion and Plasma Physics*

[90] S. Brezinsek *et al* 2013 *Nucl. Fusion* **53** 083023